N d'ordre : 3962

THÈSE

PRÉSENTÉE À

L'UNIVERSITÉ BORDEAUX 1

ÉCOLE DOCTORALE DE MATHÉMATIQUES ET INFORMATIQUE

Par **Joanne DUBOIS**

POUR OBTENIR LE GRADE DE

DOCTEUR

SPÉCIALITÉ : Mathématiques appliquées

MODÉLISATION, APPROXIMATION NUMÉRIQUE ET COUPLAGE DU TRANSFERT RADIATIF AVEC L'HYDRODYNAMIQUE

Soutenue le : 15/12/2009

Après avis de :

M.	Christophe CHALONS,	Maître de conférences,	Université Paris 6
M.	Boniface NKONGA,	Professeur,	Université de Nice

Devant le jury formé de :

M.	Christophe BERTHON,	Professeur,	Université de Nantes
M.	Christophe CHALONS,	Maître de conférences,	Université Paris 6
M.	Pierre CHARRIER,	Professeur Emérite,	Université Bordeaux 1
M.	Bruno DUBROCA,	Docteur (HDR),	Université Bordeaux 1
M.	Luc MIEUSSENS,	Professeur,	Université Bordeaux 1
M.	Boniface NKONGA,	Professeur,	Université de Nice

Invitée :

Mme	Thanh-hà NGUYEN-BUI,	Docteur (HDR),	CEA/CESTA

-2009-

Table des matières

Table des figures

Introduction

Contexte général

Le rayonnement intervient dans de nombreuses configurations physiques présentes aussi bien dans la vie de tous les jours que dans des applications de plus grande envergure. Outre l'observation et l'expérimentation, la simulation numérique d'un tel phénomène est un outil important dans le but d'en améliorer la compréhension. La connaissance de la propagation du rayonnement et de son influence sur un milieu donné est nécessaire dans de nombreux domaines. Le transfert radiatif intervient en effet dans des processus industriels tels que les fours de cuisson du verre, dans les écoulements haute température et même en météorologie. La variété des applications contribue à l'intérêt porté à ce phénomène. La présente étude n'en abordera qu'un petit nombre.

La caractérisation du comportement des photons dans les rayons X est notamment nécessaire dans le domaine de l'imagerie médicale. La reconstruction d'images du corps humain est en effet possible grâce à une bonne connaissance et surtout à une modélisation adéquate du transport du rayonnement à travers les tissus biologiques. Il s'agit de prendre en compte le fait que le rayonnement traverse différents types de tissus, comme dans le cas du cerveau humain qui se trouve entouré de substances aux propriétés diverses. Certains tissus possèdent la propriété de disperser le rayonnement, alors que d'autres se contentent d'en absorber une partie.

Un second exemple est celui de la combustion lors de laquelle le rayonnement, selon le combustible utilisé et la présence ou non de suies, contribue de manière importante à l'entretien de la flamme. Ce phénomène a été étudié par J.-F. Ripoll dans [38]. La combustion et les processus radiatifs associés (émission, absorption, dispersion) interviennent dans de nombreuses applications telles que la propulsion d'engins spatiaux, les risques industriels et la prévention des feux. Pour ces applications, le transport des photons se doit d'être couplé aux phénomènes hydrodynamiques qui interviennent tels que la convection, ou les réactions chimiques engendrées par l'élévation de température au sein de la flamme.

L'hydrodynamique radiative a aussi été étudiée par M. González dans [20] pour application au domaine de l'astrophysique, et notamment aux chocs radiatifs et jets moléculaires d'étoiles jeunes. Les observations faites des objets astrophysiques et les données collectées sont rendues compréhensibles par une bonne simulation de l'interaction des photons avec le gaz.

Enfin, dans ce mémoire, nous nous intéresserons à la rentrée atmosphérique de

véhicules spatiaux. Les rentrées atmosphériques font intervenir des écoulements à des régimes dits hypersoniques, c'est à dire avec des nombres de Mach supérieurs à 5. Lors de la rentrée du véhicule dans l'atmosphère, une onde de choc se forme par compression à l'avant du véhicule. Le gaz, considéré comme un fluide compressible, voit sa pression et sa température atteindre des valeurs très importantes derrière cette onde de choc, notamment à proximité du point d'arrêt.

FIGURE 1 – Rentrée atmosphérique.

La température devient suffisamment élevée pour exciter l'énergie de vibration interne des molécules en présence. Dans le cas de l'air, ces effets deviennent importants au-delà de $800K$. Avec cette augmentation de température ainsi induite, des réactions de dissociation et même d'ionisation des espèces présentes peuvent avoir lieu. Une région hors-équilibre est alors observée derrière l'onde de choc. Le retour du fluide à l'équilibre se fait suite à des échanges d'énergie par collisions intermoléculaires.

Ces échanges d'énergie permettent la relaxation des espèces excitées vers un état d'énergie plus stable, ceci s'accompagnant de l'émission d'un photon transportant une énergie $E = h\nu$, où h est la constante de Planck, et ν la fréquence du rayonnement. Ce photon peut ensuite être absorbé, ou dispersé par le milieu dans lequel il se déplace. Ces différents comportements sont influencés par l'opacité, également appelée épaisseur optique, du milieu considéré. On peut distinguer les opacités d'émission, d'absorption et de dispersion, celles-ci dépendant de l'activité radiative du fluide, et notamment des espèces qui le composent.

Pour un fluide donné, les distributions de population des états excités des espèces radiatives doivent être connues pour pouvoir caractériser les phénomènes radiatifs tels que l'émission et l'absorption de photons, et ainsi déterminer l'opacité du milieu. Pour cela, on s'intéresse à l'énergie interne des molécules. Elle est le résultat

des contributions de quatre modes d'énergie : translation, rotation, vibration et électronique. Dans le cas d'un atome, seuls les énergies de translation et électronique existent. La mécanique quantique permet de quantifier ces différents modes d'énergie afin de déterminer l'état et l'énergie interne d'une espèce chimique.

D'après la mécanique quantique, il existe donc un ensemble dénombrable de niveaux d'énergie sur lesquels sont distribués les atomes et molécules à un instant donné. On sait que pour un système à l'équilibre thermodynamique, la distribution la plus probable est régie par une distribution gaussienne appelée Maxwellienne. Dans l'étude réalisée ici, on ne cherchera pas à déterminer nous-même les opacités d'émission et d'absorption. On se restreindra à des opacités données qui ne dépendent pas de la composition ni de l'état du système.

Il apparaît indispensable d'évaluer la contribution du rayonnement dans la mesure où le dimensionnement d'un véhicule de rentrée sera déterminé de façon à limiter les flux thermiques à la paroi. Nous nous intéresserons exclusivement à l'avant du véhicule et au rayonnement thermique engendré dans cette zone.

Précisons que l'importance du rayonnement thermique par les gaz chauds de la couche de choc (délimitée par le corps de rentrée et la discontinuité) dépend de plusieurs paramètres, relatifs à la géométrie de la couche de choc, et à son état chimique et thermodynamique. Par exemple, plus la couche de choc est épaisse, plus le volume de gaz susceptible d'émettre un rayonnement est important. Ainsi, comme l'épaisseur de la couche de choc est proportionnelle au rayon de courbure du véhicule, le flux radiatif au point d'arrêt devient aussi proportionnel au rayon de courbure. Il en résulte que, pour des conditions de rentrée données, les flux thermiques d'origine radiative seront moins importants si l'on réduit le rayon de courbure du véhicule. Par contre, les flux thermiques à la paroi liés à la convection sont inversement proportionnels à la racine carrée du rayon de courbure [1]. Il appartiendra donc aux ingénieurs de trouver le bon compromis qui reduira l'impact thermique total.

Selon le type de rentrée (vitesse, composition chimique de l'atmosphère), le rayonnement peut s'avérer être un phénomène prépondérant par rapport à la convection. Le rayonnement est le résultat de toutes les émissions et absorptions ayant lieu dans le gaz présent dans la couche de choc. L'énergie radiative est transférée dans toutes les directions à travers le fluide. Cette énergie, en fonction de la nature et de l'opacité du milieu, est ainsi soit absorbée, soit atteint la surface du véhicule, soit s'éloigne de la proximité du véhicule et favorise le refroidissement de la couche de choc.

Ces effets dûs à la prise en compte du rayonnement sont mis en évidence à l'aide de la figure 2. Il s'agit de calculs effectués dans le cas de la sonde Mars Sample Orbiter. Nous nous intéressons dans cette introduction à l'aspect qualitatif des résultats présentés. La géométrie de la sonde considérée est axi-symétrique, seule la moitié inférieure de la zone de calcul est donc représentée. La sonde occupe la partie restée blanche dans le coin en haut à droite de la figure. La figure de gauche est le résultat d'un couplage des phénomènes hydrodynamiques avec le rayonnement, alors que la figure de droite résulte d'un calcul découplé (sans rayonnement). Au vu des contours de températures obtenues, il est clair que la contribution du rayonnement n'est pas négligeable, du moins en terme de températures et d'épaisseur de la couche de choc.

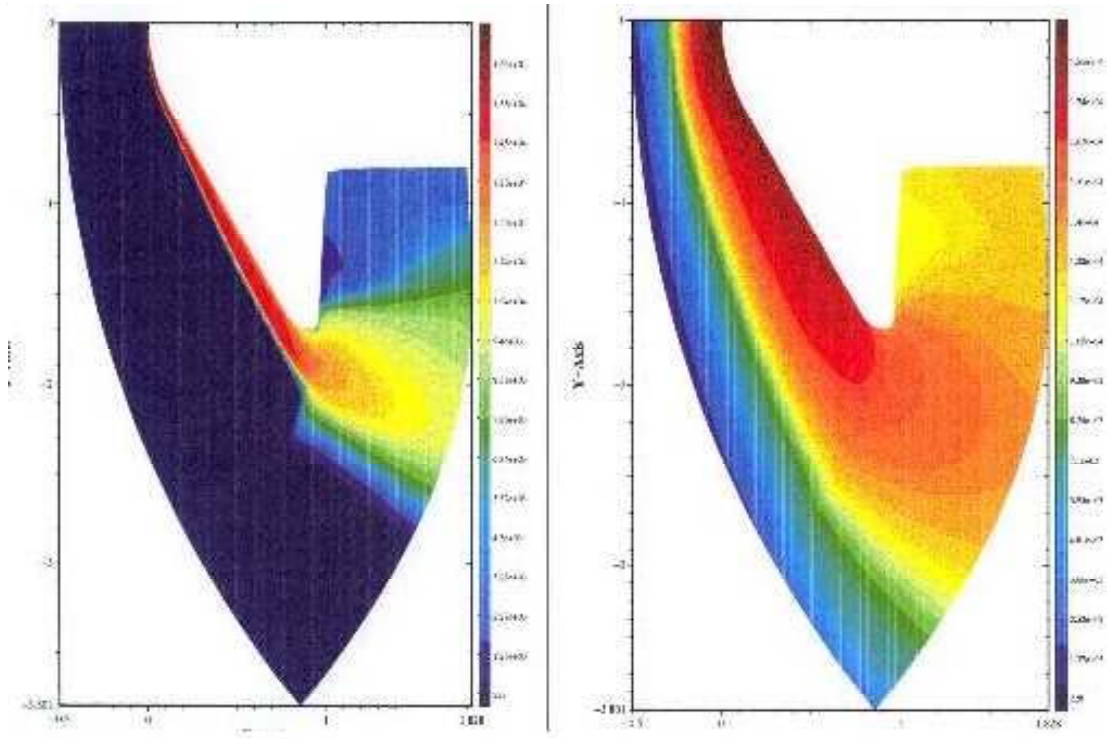

FIGURE 2 – Cartes de températures. Avec couplage (à gauche) et sans couplage (à droite) avec le rayonnement.

Ainsi, si on choisit de simuler de telles applications impliquant des échanges d'énergie entre le rayonnement et la matière, il est clairement nécessaire de coupler l'écoulement et le rayonnement. Cependant, remarquons que d'importantes différences d'échelles de temps caractéristiques existent entre la convection (de l'ordre du $m.s^{-1}$ ou du $cm.s^{-1}$), les réactions chimiques un peu plus rapides, et le rayonnement qui se déplace à la vitesse de la lumière.

La résolution du problème radiatif sera ainsi soumise à de nombreuses itérations, par rapport aux phénomènes hydrodynamiques. La méthode de résolution du transfert radiatif est donc déterminante dans le coût de calcul d'un problème couplé rayonnement/hydrodynamique.

La forme microscopique de l'équation du transfert radiatif décrit le champ radiatif et son interaction avec la matière. Cette équation régit l'évolution de l'intensité radiative I. Une telle description microscopique est classiquement utilisée dans le cas de milieux transparents. Des méthodes de résolution dites particulaires directes, ou statistiques (comme la méthode Monte-Carlo) y sont associées. Cette dernière méthode considère des paquets de photons dont la direction et la fréquence sont aléatoires. La distance parcourue par les photons avant absorption ou diffusion dépend de l'opacité du milieu. Outre le difficile couplage de ces méthodes avec les codes d'hydrodynamique, elles sont aussi très coûteuses, notamment en régime de diffusion.

Dans le cas des milieux opaques, des méthodes de type macroscopique sont souvent utilisées. En milieu opaque, nous sommes proches de l'équilibre radiatif, et des

modèles dits de diffusion sont utilisés pour décrire le comportement radiatif. Sous l'hypothèse de quasi-isotropie directionnelle de répartition d'émission des photons reposent les modèles dits de diffusion tels que l'approximation de Rosseland, ou le modèle aux moments P_1. L'utilisation de ces modèles est restreinte aux milieux opaques. Ainsi pour des applications où coexistent des régions optiquement minces et épaisses, il faut coupler méthodes microscopiques et modèles de diffusion. Un tel couplage est complexe et présente des inconvénients tels qu'une perte de précision dans les zones de transition, et il persiste notamment un mauvais traitement du transfert radiatif dans les milieux semi-transparents puisque les deux méthodes citées ci-dessus ne sont performantes que dans les cas limites, c'est à dire en milieu opaque pour l'une, et en milieu transparent pour l'autre. Dans ces conditions, il n'est pas raisonnable d'envisager le couplage d'une telle méthode d'approximation du transfert radiatif à l'hydrodynamique.

On préfère donc approcher l'équation du transfert radiatif à l'aide d'une unique méthode de type macroscopique. Le modèle P_1 est inadapté car il ne respecte pas la propriété de limitation du flux en régime de transport. C'est pourquoi on choisit d'utiliser le modèle aux moments M_1 développé par Dubroca et Feugeas [17], et qui permet un panel plus large d'applications. Ce modèle est le résultat de moyennes sur l'espace des fréquences et des directions, et contrairement au modèle P_1, M_1 considère une fonction de distribution avec une direction de propagation privilégiée alignée avec le flux radiatif. Les trois premiers moments de l'intensité radiative sont l'énergie radiative, le flux radiatif, et le tenseur de pression radiative. Ils ne dépendent plus que du temps et de paramètres d'espace.

Le modèle M_1, de par son hypothèse de fermeture, est d'autant plus intéressant qu'il offre la possibilité de traiter les régimes de transport aussi bien que les régimes de diffusion. En effet, son prédécesseur, le modèle P_1 décrit un comportement non physique des photons en régime de transport (le rayonnement obtenu tend à se déplacer plus vite que la vitesse de la lumière), alors que le modèle M_1 permet de préserver cette limitation du flux radiatif dans les milieux transparents. Et dans les milieux opaques, le système M_1 dégénère en une équation de diffusion. Notons aussi que ce modèle préserve la positivité de l'énergie.

A partir de ce modèle, l'enjeu du travail présenté dans ce document est d'y associer un schéma numérique qui résout précisément un problème donné de transfert radiatif. Le schéma HLL, introduit par Harten-Lax-Van Leer [27], est classiquement utilisé et simple à mettre en oeuvre. Mais ce schéma donne des résultats présentant une viscosité numérique importante, notamment dans les problèmes 2D. On a donc cherché à développer un schéma capable de capturer avec plus de précision les discontinuités de contact et tenant compte de la propagation du rayonnement dans une direction transverse.

Pour ce faire, il est courant de développer des schémas de type HLLC qui ont la propriété de capturer les discontinuités de contact. Cependant, dans le cas du schéma HLLC, la construction de linéarisations appropriées reste délicate. Dans [11] et [12], certains types de linéarisations sont employés, mais la robustesse du schéma n'y est pas établie. Assurer la robustesse des méthodes développées constitue un point important de la présente étude. On veillera tout particulièrement au respect

des propriétés physiques importantes telles que la positivité de l'énergie radiative, et la limitation du flux.

Afin de construire plus facilement des linéarisations, et de mieux contrôler les propriétés de robustesse, il a tout d'abord été envisagé de développer un schéma dit de 'relaxation'. Ce type de schéma présente deux avantages intéressants pour notre étude : il permet de capturer les discontinuités de contact, tout en assurant la robustesse du schéma. Malgré ce gain en précision, le schéma de relaxation ainsi construit s'avère être relativement coûteux, ceci étant dû au calcul des coefficients qui nous permettent d'assurer la robustesse du schéma. Ces coefficients sont difficiles à déterminer, et font notamment intervenir un nombre important d'équations quadratiques.

La construction d'un schéma de relaxation dans le cadre du transfert radiatif nous a tout de même permis de mettre en évidence des linéarisations importantes pour le développement d'un schéma précis pour le modèle M_1. Ce dernier est un schéma de type HLLC. C'est une méthode similaire à la relaxation, qui possède les mêmes propriétés de robustesse, tout en étant plus simple à mettre en oeuvre, et elle est aussi moins coûteuse (une seule équation quadratique y est impliquée). Grâce à ce schéma HLLC, nous observons un gain important en précision lors des tests numériques que nous avons réalisés pour la validation de la méthode.

Plan de la thèse

Le chapitre 1 introduira la physique du rayonnement, et à travers les besoins spécifiques à nos applications, on déterminera le cahier des charges auquel doit répondre notre modèle. Un état de l'art sur les modèles et méthodes connus et utilisés pour traiter du transfert radiatif nous guidera dans notre choix. On présentera ensuite plus en détail le modèle M_1 développé par Dubroca and Feugeas [17]. Une reformulation du modèle sera proposée et conduira au développement de schémas numériques précis.

Dans le chapitre 2, l'étude sera d'abord exposée à partir d'une formulation 1D du système. On présentera le principe de l'approximation des solutions faibles du système M_1 par des méthodes aux volumes finis. Le solveur de Riemann de Harten-Lax-Van Leer [27] possède jusqu'à présent l'exclusivité en ce qui concerne le transfert radiatif. Il présente cependant des désavantages connus. Nous le présenterons et l'utiliserons comme point de départ pour le développement d'un schéma apte à capturer l'onde de contact que le schèma HLL néglige. On commencera par la construction d'un schéma de relaxation, avant d'aborder le schéma HLLC. Pour chacun de ces schémas on veillera à en assurer la robustesse. Une comparaison de leurs performances clôturera ce chapitre.

Ensuite, outre une montée en ordre de la solution à l'aide d'un schéma de type MUSCL, on s'intéressera au comportement du schéma dans les régimes asymptotiques, c'est à dire en régime de diffusion dans les milieux opaques et en régime de transport dans les milieux transparents, à travers un schéma 'asymptotic preserving' que l'on détaillera dans le chapitre 3.

Puis, au chapitre 4, on explicitera les extensions réalisées à partir du schéma HLLC précédemment construit, pour considérer des problèmes en deux dimensions d'espace et à géométrie curviligne.

Enfin, dans le chapitre 5, des cas tests purement radiatifs mettront en évidence les progrès réalisés en termes de précision numérique par comparaison avec le schéma HLL, ainsi que les limitations du schéma notamment en ce qui concerne les deux faisceaux de directions convergentes.

Une applications plus réelle et couplée à l'hydrodynamique sera mise en oeuvre dans le dernier chapitre, l'entrée Venusienne de la sonde Pioneer, qui nous permettra d'entrevoir le gain en coût de calcul qu'il est possible de réaliser.

Pour finir, nous présenterons une conclusion de ce travail, ainsi que les perspectives envisagées.

Chapitre 1

The Radiative Transfer Equation

1.1 Introduction

The work presented in this document is dedicated to the specification of radiative transfer in physical applications. This phenomenon is involved in many applications such as industrial processes (e.g. glass cooling), radiotherapy, combustion, astrophysics and atmospheric entries of space vehicles.

Among these applications, let us develop the example of the atmospheric entry. For this application, we are often confronted to hypersonic regimes where the Mach number is higher than 5. And depending on the entry parameters, such as the density and chemical composition of the planet's atmosphere, the speed of the entering vehicle, radiation transfer effects are more or less noticeable. For instance, in the case of aerobreaking (when the vehicle is slowed down thanks to viscous effects), two third of the energy is dissipated through radiative effects.

Indeed, because of the atmosphere density, the flow speed is considerably reduced, and a great part of kinetic energy is transformed into internal energy. The temperature inside the shock layer then becomes high enough ($> 3000K$) to raise the internal energy of the species in presence in the gas. In the case of very high temperatures, dissociation and even ionisation reactions may occur.

When the temperature in the shock layer is sufficiently high, the thermal radiation emitted by the gas becomes important. This radiative energy travels through the flowfield in all directions and is either absorbed by the gases or leaves the shock layer, or reaches the body surface. Heat fluxes from the gas must be taken into account for the sizing of the thermal protection of hypersonic vehicles. For instance, in the case of an optically thin gas, the radiative flux to the body is known to be proportional to the radius of curvature of the body, this radius would then appear as one of the parameters to modify to make the vehicle viable. With this purpose in mind, interests about the effects of radiation on the hydrodynamics are raised within the aerodynamic society.

Another possible application is medical imaging in order to make possible a proper reconstruction of the human body. Human tissues are very diverse and an appropriate behaviour of the radiative model with the tissue characteristics is mandatory.

Combustion problems are also constraining from that point of view as far as the flame may be of different nature depending on the presence of soot or not. And radiation effects on the flame are then different whether it is confined in an optically thick medium, or whether it is free to be transported to the outer environment. Let us mention that such a flame is chemically reacting, and that convection also plays an important part in the overall behaviour of the flame. Such hydrodynamic phenomena then have to be coupled to radiation.

It is therefore set from the begining that we have some requirements to meet. Indeed, we need a radiation model that is quite simple to couple with hydrodynamic phenomena. In addition, we need a model that allows a treatment of various propagation regimes, that is to say, radiative transfer in an optically thick medium, where the mean free path of the photon is small, as well as in a transparent medium, where the mean free path is big.

With this aim, after an overview on radiation and the usual resolution methods in particular configurations, we argument the radiative model we choose to use and the solution approximation method we therefore adopt. In this chapter, we detail the macroscopic model that is derived from the radiative transfer equation. This model has several interesting features that motivated its use, and which we detail here. Particularly, we will see how coherent it is with the physical phenomena we are interested in, and which are the constraints to impose on the macroscopic quantities.

An hyperbolic system is derived from the model and its properties are outlined. The radiative variables are expressed and some useful relations are given. This chapter introduces the tools on which relies the numerical study we make from Chapter 2 until the thesis conclusions.

1.2 Generalities on radiation

Radiation is a form of energy that can even propagate in vacuum. It is transported by weightless photons travelling at the speed of light in vacuum.

Meanwhile, when propagating in a non-vacuous medium, three main phenomena are observed when radiation interacts with matter : emission, absorption and scattering. The species in the shock-layer have their internal energy excited due to the high temperature of the gas. A high energy level is then reached. Molecular collisions in the gas lead to a relaxation of the gas species. Their energy is relaxed back to their initial and stable configuration, that is to say to a lower energy level. This is actually the result of a photon emission. This photon transports an amount of radiative energy $E = h\nu$, where h is Planck's constant, and ν the photon frequency.

On the contrary, absorption occurs when matter absorbs energy and raises its internal energy levels. An absorption opacity is also associated and is inversely proportional to the mean free path between two photon absorptions of a given frequency. When the mean free path tends to infinity (the opacity tends to zero), the photons are not absorbed, whereas when the mean free path tends to zero (the opacity is big), the photons are absorbed right after being emitted and the gas tends towards radiative equilibrium.

A third possible behaviour is the scattering occurring if the propagation direction is modified without interaction with matter. In the case of scattering the radiative energy is conserved, the matter only deviates the photon and does not absorb nor emit photons. Scattering is observable for example on a foggy day as it makes the cars' lights thicker.

Note that in entry flowfields, as radiation is mainly due to electronic transitions, the frequencies of interest are the infrared, visible and ultra-violet bands. An emission opacity is characteristic of the gas properties, and it is inversely proportional to the mean free path between two photon emissions of a given frequency.

Radiation has an intensity I depending on four parameters which are : time t, space $x \in \mathbb{R}^3$, frequency ν and direction $\mathbf{\Omega} \in \mathbb{R}^3$. The specific radiative intensity is associated to the photons distribution function $\tilde{f}$ and they are related as :

$$I(t, x, \Omega, \nu) = ch\nu\tilde{f}(t, x, \mathbf{\Omega}, \nu), \tag{1.1}$$

where h is Planck's constant and c is the speed of light.

If the radiative intensity does not depend on x, I is said to be homogeneous. And, if the radiative intensity does not depend on the photons propagation direction vector $\mathbf{\Omega}$ then it is said to be isotropic. A common example where this particular approximation is usable is a far-distant source of light such as stars. This particular case leads to an easier analysis of radiative transfer.

Let us now enumerate the different states of the flow that can be encountered in atmospheric entries. With the rise of temperature chemical reactions can occur and the flow is then in chemical non-equilibrium. When dissociation and ionisation reactions are also involved, the flow turns into an ionised plasma.

In addition, when all radiative processes occur at a local equilibrium temperature of the gas, an additional radiative equilibrium is attained. The matter is said to be in equilibrium with the radiative phenomenon and the photons are described according to Planck's function. In this particular case, an homogeneous and isotropic radiative field has its specific radiative intensity equal to the black body function $B = B_\nu(T)$ with :

$$B_\nu(T) = \frac{2h\nu^3}{c^2}\left[exp(\frac{h\nu}{kT}) - 1\right]^{-1}, \tag{1.2}$$

where k is Boltzmann's constant, ν is the frequency, and T is the matter temperature. This function is known as Planck's law where the radiative energy is continuously distributed versus the wavelength $\lambda = 2\pi/\nu$. Planck's function is assimilated as an equilibrium function, its use is relevant when all absorbed photons are immediately re-emitted, and so on, which corresponds to the photons behaviour in an optically thick medium (where the mean free path tends to zero).

Let us introduce some representative macroscopic variables. They are obtained as the integration of the microscopic variables over the wavelength and frequency ranges. We introduce the following average operator :

$$\langle . \rangle = \frac{1}{c}\int_0^\infty \int_{S^2} . \, d\mathbf{\Omega} d\nu. \tag{1.3}$$

The macroscopic variables we will use in all the following developments then are :

$$\begin{aligned} &\bullet \text{ the radiative energy} \quad E_R = \langle I \rangle \,, \\ &\bullet \text{ the radiative flux vector} \quad \mathbf{F}_R = \langle c\mathbf{\Omega} I \rangle \,, \\ &\bullet \text{ the radiative pressure tensor} \quad \mathbf{P}_R = \langle \mathbf{\Omega} \otimes \mathbf{\Omega} I \rangle \,. \end{aligned} \tag{1.4}$$

These radiative variables are the first three moments of the radiative intensity I. They are submitted to essential properties. Indeed, as the radiative intensity I is a positive variable, the radiative energy E_R is also a positive variable. Additionally, the radiative flux is physically limited by the speed of light so that : $-cE_R \leq F_R \leq cE_R$.

An important data for the resolution of radiative transfer is the medium opacity. It is determined through the knowledge of excited states energy levels and their population. In most cases, equilibrium can not be considered, the different internal modes of the species in presence in the shock layer are excited. To determine the excited states number densities various assumptions and models may be used. For instance, the number densities of vibrational states within an electronically excited state can be determined with a Boltzmann distribution employing the vibrational temperature. The same equilibrium assumption holds for the calculation of rotational states, although the Boltzmann distribution employs the translational temperature since the rotational temperature is known to equilibrate very fast with the translational one.

Once the flowfield variables, such as temperature, species densities, and excited states population distributions are known, the radiative processes remain to be determined. With this aim, four methods with various accuracy levels are available in order to determine the needed opacities of the medium through which radiation is travelling. The absorption and emission opacities are usually presented in the form of an absorption or emission spectrum, where the values are plotted versus the corresponding wavelength. A spectrum example is given in Figure 1.1.

Number of databases exist for a given temperature range. In the case of geophysical applications, the associated temperatures are more often lower than $400K$. Combustion processes involve temperatures between $1000K$ and $2000K$. And electric arcs, lasers and atmospheric entries deal with temperatures from $3000K$ to $25000K$.

The low temperature cases make use of the databases HITRAN and HITEMP that contain molecular band spectra (from the near infrared to the wavelength of the order of the millimeter). Figure 1.1 is actually a spectrum obtained from these databases.

As for the high temperatures, the PARADE [40] and NEQAIR [48] databases are actually codes that calculate the emission and absorption spectrum through a line by line procedure, every transition line over the whole spectrum is specified. This method is very expansive and is usually used as a validation tool and reference solution.

Indeed, because of the important number of spectral lines, a detailed calculation is not to be considered. Other alternatives are available. The spectrum may indeed be divided into spectral intervals within which averages are performed. The first category of these averaging models deals with band models where mean opacities are determined over narrow spectral bands. This method remains expansive to use.

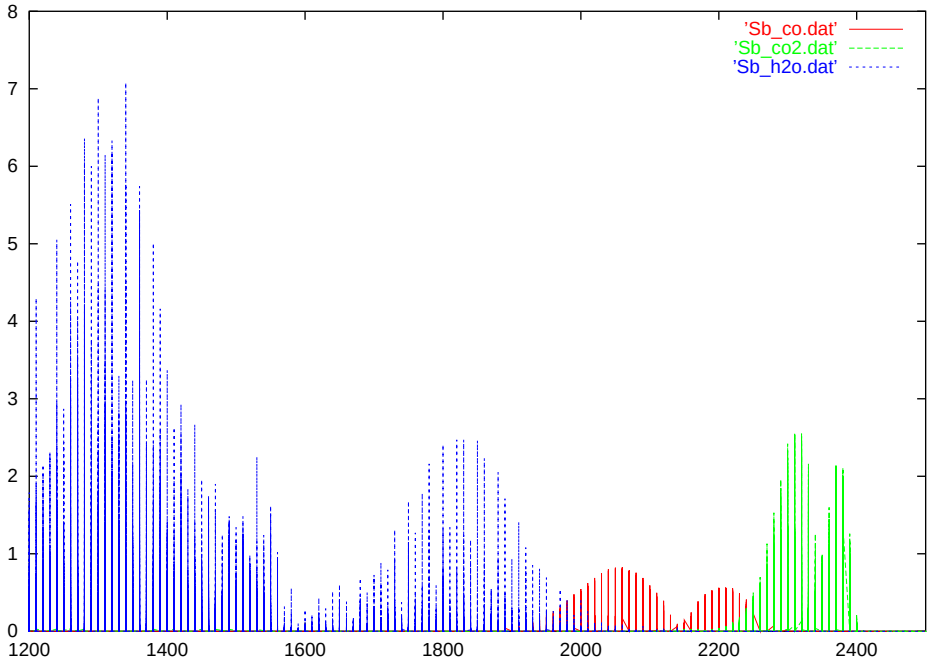

FIGURE 1.1 – Absorption coefficient (m^{-1}) versus the wavelength (cm^{-1}) for the CO, CO_2 and H_2O molecules

A third option is the multi-group method developped by Turpault [43] [44], where the spectrum is divided into wider spectral bands than band models. The obtained mean values may bring errors in the solution however it is usually not possible to use more accurate methods because of the lack of data. Finally, with a fourth method, it is possible to integrate over the full sprectrum. These models are called "grey" models. They are appropriate for applications where we simply focus on the energy balance of the problem.

Mean macroscopic opacities are often used in macroscopic models such as moments models. We use the definition of the moments of the radiative intensity to express the mean opacities as they are needed in such models. In our case, these mean macroscopic opacities are defined as follows :

$$\sigma^e = \frac{\langle \sigma B(T) \rangle}{aT^4}, \tag{1.5}$$

$$\sigma^a = \frac{\langle \sigma I \rangle}{E_R}, \tag{1.6}$$

$$\sigma_x^f = \frac{c\langle \sigma \Omega_x I \rangle}{F_R}, \tag{1.7}$$

$$\sigma_y^f = \frac{c\langle \sigma \Omega_y I \rangle}{F_R}, \tag{1.8}$$

where a is a constant defined later. Here σ^e is the emission opacity, it is also called Planck's average. The variable σ^a is the absorption opacity, and σ_x^f and σ_y^f are the radiative flux absorption opacities. The calculation of the opacities is not realised in

the present work. At the most, we will mainly consider thermal equilibrium or local thermodynamic equilibrium so that the opacity is only a function of the density and temperature. Pressure and temperature may also be used to evaluate the opacity, which is equivalent thanks to the appropriate equation of state.

Now that we have defined the opacities, we are left with the resolution of the radiative transfer problem. Our starting point is the time-dependant Radiative Transfer Equation (RTE) describing the behaviour of the photons distribution function I. It writes :

$$\begin{aligned}\frac{1}{c}\partial_t I_\nu(\mathbf{\Omega}) + \mathbf{\Omega}.\nabla I_\nu(\mathbf{\Omega}) = S_\nu - (\sigma_\nu^a + \sigma_\nu^d) I_\nu(\mathbf{\Omega}) \\ + \frac{\sigma_\nu^d}{4\pi}\int_{S^2} p_\nu(\mathbf{\Omega}'.\mathbf{\Omega}) I_\nu(\mathbf{\Omega}') d\mathbf{\Omega}' d\nu,\end{aligned} \tag{1.9}$$

where σ_ν^a and σ_ν^d are respectively the absorption and scattering opacities, p_ν is the scattering probability and S_ν is the emission source term. As mentioned earlier, in the case of a local thermal equilibrium, this source term can be expressed thanks to Planck's blackbody function as :

$$S_\nu = \sigma_\nu^e B_\nu(T), \tag{1.10}$$

where σ_ν^e is the emission opacity and $B_\nu(T)$ is defined by (1.2).

This RTE actually reveals to be too sophisticated to be utilised in its form (1.9) in our context, where a coupling to hydrodynamic phenomena is needed. The solution we have at our disposal is then to use approximate models of the RTE. We then have to choose an appropriate radiative model. In the applications we mentionned and that we are aiming to simulate, very diverse propagation regimes can be encountered. The radiative model should be chosen carefully so that it is appropriate for our applications.

In order to justify the choice of the model we make, let us specify the two limit regimes we have to deal with for our dedicated applications. When the opacity tends to zero, the photons are not absorbed by the matter, and then travel in free streaming. The associated propagation regime in the limit of a zero opacity is a transport regime. On the other hand, when the mean free path of the photons is short, the opacity tends to infinity. It is known that in this opaque medium limit, the matter temperature can be approximated by the solution of an asymptotic model called equilibrium diffusion equation (see Mihalas [34] and Pomraning [36]). We therefore need to choose an approximate model that solves those two limit regimes : transport and diffusion. More often, the proposed models are able to deal properly with the free streaming regime, whereas it is more tricky to solve appropriately the diffusion regime.

Let us now make an overview of the methods available so far. In fact, if we first consider the microscopic methods, we can cite the statistical method known as the Monte-Carlo method. Like the direct methods, it looks at groups of photons. From a number of directions and frequencies defined beforehand, the direction and frequency of the group of photons we are looking at is then randomly set. This group of photons then interacts with the matter and travels through it. This method works quite well

in transparent medium, where the opacity is close to zero. However, a solution is longer to obtain in opaque mediums. This is related to the optical thickness of the medium, indeed, the mean free path of the photons being very short, the transfer of the photons from point to another involves even more processes as the mean free path is short. This makes these microscopic methods not easily applicable in opaque mediums, even if they are quite efficient in the transport regime.

The next alternative we mention here are macroscopic models obtained from the integration of the RTE over frequencies and directions. They are often used in order to perform cheap resolutions from a computational point of view.

1.3 Macroscopic models

Using macroscopic equations in fluid mechanics through the moments method has been suggested by Grad [24] in 1949. He proposed to introduce unknowns such as the stress tensor and the heat flux. They are called moment models as they involve the moments of the radiative intensity I such as the radiative energy E_R, the radiative flux $\mathbf{F}_R$ and the radiative pressure $\mathbf{P}_R$. These moments models actually focus on the energy balance. Then, the model to use only depends on time and space parameters, and not anymore on direction and frequency parameters. An appropriate closure is needed for the moments system derived from Boltzmann's equation to be hyperbolic.

Let us assume the RTE with no scattering source term, and a frozen flow in Local Thermal Equilibrium. In fact, radiative energy is not conserved so we choose to couple the radiative and matter energies to obtain a conserved total energy. We describe radiative transfer and its interaction with matter through the following equations :

$$\frac{1}{c}\partial_t I + \mathbf{\Omega}.\nabla I = \sigma\left(B_\nu(T) - I\right), \tag{1.11}$$

$$\partial_t\left(\rho C_v T\right) = -\int_0^\infty \int_{S^2} \sigma\left(B_\nu(T) - I\right) d\mathbf{\Omega} d\nu, \tag{1.12}$$

where T is the matter temperature, ρ is the density, and C_v is the specific heat at constant volume. The term $\sigma\left(B_\nu(T) - I\right)$ sets a balance between the photons emission and absorption, σ being the absorption opacity.

Given the definition of the radiative energy and the radiative flux as the first two moments of the radiative intensity, the non-dimensional radiative flux is defined as : $f = \|\mathbf{F}_R\| / cE_R$ where $\|\cdot\|$ is the euclidian norm. Let us remind that, to verify the limited flux property, this non-dimensional flux must be such that :

$$f \leq 1. \tag{1.13}$$

Note that Planck's function, given by (1.2), has its energy expressed in terms of the temperature as :

$$\frac{1}{c}\int_0^\infty \int_{S^2} B_\nu(T) d\mathbf{\Omega} d\nu = aT^4, \tag{1.14}$$

where the coefficient a is given by $a = \frac{8\pi^5 k^4}{15h^3c^3}$. The coefficient a is usually written as $\frac{4\sigma_R}{c}$ where σ_R is Stefan-Boltzmann's constant. Planck's function being isotropic, its radiative flux is equal to zero. Radiative equilibrium is indeed characterised by a zero radiative flux and a radiative energy equal to aT^4. While the radiative energy is defined by :

$$E_R = aT_R^4, \tag{1.15}$$

where T_R is the radiative temperature, it is clear that in radiative equilibrium conditions $T_R = T$.

Proposition 1. *The total energy of a radiating gas is conserved, that is to say :*

$$\partial_t(E_R + \rho C_v T) + div(\mathbf{F}_R) = 0. \tag{1.16}$$

Proof. Let us start with Equation (1.11) and integrate over directions and frequencies :

$$\langle \frac{1}{c}\partial_t I + \mathbf{\Omega}.\nabla I \rangle = \langle \sigma \left(B_\nu(T) - I\right) \rangle. \tag{1.17}$$

And with $\mathbf{\Omega}.\nabla I = div(\mathbf{\Omega} I) - I div(\mathbf{\Omega})$ where $div(\mathbf{\Omega}) = 0$, it comes :

$$\partial_t E_R + div(\mathbf{F}_R) = \langle c\sigma \left(B_\nu(T) - I\right) \rangle. \tag{1.18}$$

Meanwhile, from Equation (1.12), we have :

$$\partial_t(\rho C_v T) = -\langle c\sigma \left(B_\nu(T) - I\right) \rangle. \tag{1.19}$$

Now, adding up the two Equations (1.18) and (1.19), we obtain (1.16). The proof is thus achieved. □

Now, let us write the moments system obtained in the grey case from the integration of the Radiative Transfer Equation (1.9) where the first three moments of the radiative intensity (1.4) intervene. We have :

$$\begin{cases} \partial_t E_R + div(\mathbf{F}_R) = c\sigma(aT^4 - E_R), \\ \partial_t \mathbf{F}_R + c^2 div(\mathbf{P}_R) = -c\sigma \mathbf{F}_R, \\ \partial_t(\rho C_v T) = -c\sigma(aT^4 - E_R). \end{cases} \tag{1.20}$$

From this system, there exist many possibilities in the choice of the closure hypothesis. This choice is indeed important as it determines the various properties of the model, its capabilities and failures. We present three of the main models that are usually used.

1.3.1 Diffusion models

In the case of applications where diffusion is the main propagation regime, so called "diffusion models" are more often used. Diffusion models are an alternative where the Radiative Transfer Equation is assimilated to a parabolic equation. This method is applied in optically thick cases, radiative equilibrium conditions are then assumed and Rosseland's limit in such diffusion regimes is considered. In this model, we only consider the evolution equation of the radiative energy. To solve it, we express the radiative flux as a function of the radiative energy. For that, we make the assumption of a continuous regime in the evolution equation of the radiative flux in (1.20). It comes :

$$c\, div(\mathbf{P}_R) = -\sigma \mathbf{F}_R. \tag{1.21}$$

Next, we define the closure relation based on the fact that in the diffusive regime, the pressure is isotropic and :

$$\mathbf{P}_R = \frac{E_R}{3}\mathbf{I}, \tag{1.22}$$

where $\mathbf{I}$ is the identity matrix.

Coming back to our diffusion model, and replacing the expression of $\mathbf{P}_R$ in (1.21), we obtain a relation between the radiative flux and the radiative energy :

$$\mathbf{F}_R = -\frac{c}{3\sigma}\nabla E_R. \tag{1.23}$$

Replacing (1.23) in the radiative energy evolution equation, we obtain the following diffusion equation :

$$\partial_t E_R - div\left(-\frac{c}{3\sigma}\nabla E_R\right) = c\sigma(aT^4 - E_R). \tag{1.24}$$

A good point for this method is that it is obviously cheap from a numerical point of view, and it is then widely used when coupling radiative transfer to any other phenomenon (hydrodynamic, chemistry ...). However, one must keep in mind that it is based on the hypothesis of an isotropic radiative pressure tensor in the diffusive limit. This method is then not adapted to transport regimes.

Moreover, from Equation (1.23), the radiative flux being proportional to the radiative energy, it is not limited by construction, which is contradictory with the radiative flux definition (it can not propagate faster than the speed of light). Some method have been developed to solve this issue where a multiplication factor is used, called "flux limiter". Although these methods are not yet good enough in the transport regime.

1.3.2 The P_1 model

In order to get rid of the disadvantages of the diffusion models, the P_1 model has been developed. The main difference with diffusion models is that we conserve

the radiative flux evolution equation, while we are still using an isotropic radiative pressure tensor.

Indeed, the P_1 system uses the function $I(T) = B_\nu(T)(\alpha + \vec{\beta}.\mathbf{\Omega})$ where the condition $I \geq 0$ is not always verified, and the flux limitation property is not ensured. Let us express the various moments of the radiative intensity. We have :

$$E_R = \langle I \rangle = \frac{1}{c}\int_0^\infty B_\nu(T)d\nu \times \int_{-1}^{1}(\alpha + \beta\,\mu)d\mu = 2\alpha a T^4, \tag{1.25}$$

$$F_R = \langle c\mu I \rangle = caT^4 \times \left[\alpha\mu^2/2 + \beta\mu^3/3\right]_{-1}^{1} = caT^4\frac{2\beta}{3}, \tag{1.26}$$

where $\mu = cos(\Omega)$ is in $(-1, 1)$. It is then possible to write :

$$I(T) = \frac{B_\nu(T)}{2caT^4}(cE_R + 3\mu F_R). \tag{1.27}$$

And then we write the radiative pressure as :

$$P_R = \left\langle \mu^2 I \right\rangle = \frac{1}{2c}\int_{-1}^{1}(cE_R + 3\mu F_R)\mu^2 d\mu = \frac{1}{2c}\left[cE_R\mu^3/3\right]_{-1}^{1}. \tag{1.28}$$

The radiative pressure can therefore be expressed as :

$$P_R = \frac{E_R}{3}, \tag{1.29}$$

that is to say, as a function of the radiative energy.

Taking into account the two evolution equations allows a better treatment of the flux limitation property. However, the closure relying on a diffusion approximation, it must be carefuly used in transport regimes. It is advised to use the P_1 model mainly in continuous regimes, when the medium is opaque and close to radiative equilibrium.

1.3.3 The M_1 model

A further improved moment model is the M_1 model developped by Dubroca and Feugeas [17] where the closure hypothesis is more general. This M_1 model is obtained from a local entropy dissipating condition. This model conveniently appears to fulfill our requirements as soon as it is able to deal properly with both transport and diffusion regimes. Indeed it remains consistent in these two regimes, and particularly, it verifies the radiative energy positivity condition and the radiative flux limitation property. Important radiative non-equilibrium can be dealt with thanks to this M_1 model. And this M_1 model is therefore chosen for the test cases of varying opacities we have to compute.

As presented in the general case of the moment models, the M_1 model is obtained when multiplying Equation (1.11) by the vector $\mathbf{m} = (1 \quad c\mathbf{\Omega})^T$ and integrate over the directions and frequencies. It writes :

$$\begin{cases} \partial_t E_R + div(\mathbf{F}_R) = c\sigma(aT^4 - E_R), \\ \partial_t \mathbf{F}_R + c^2 div(\mathbf{P}_R) = -c\sigma\mathbf{F}_R, \end{cases} \tag{1.30}$$

where E_R, $\mathbf{F}_R$ and $\mathbf{P}_R$ are the first three moments of the radiative intensity defined by (1.4). We remind that the radiation state vector $(E_R, \mathbf{F}_R)$ in $\mathbb{R}^3$ is expected to be in the following radiation admissible space :

$$\mathcal{A} = \{(E_R, \mathbf{F}_R) \in \mathbb{R}^3; E_R \geq 0, f \leq 1\}. \tag{1.31}$$

The M_1 model is based on System (1.30), however some closure hypothesis needs to be made for the unknown radiative pressure to be expressed as a function of the radiative energy and flux. As for the M_1 model, it is obtained thanks to the minimum entropy principle : the chosen radiative intensity is the one that makes the smallest radiative entropy, with the associated radiative energy and radiative flux :

$$H(\mathcal{I}) = \min_{I \geq 0} \{H(I) = \langle h^\star(I) \rangle, \langle I \rangle = E_R \,\text{and}\, c\langle \mathbf{\Omega} I \rangle = \mathbf{F}_R\}, \tag{1.32}$$

where $h^\star$ is the microscopic entropy.

Amongst the possible states, the Planck's function $B(T)$ is the most likely as it minimises the entropy H.

Note that we are working under the constraint imposing that the radiative intensity of the model remains positive.

Proposition 2. *The distribution*

$$I = B(\vec{\alpha}) = \frac{2h\nu^3}{c^2} \left[exp\left(\frac{h\nu}{kT} \vec{\alpha} \cdot \mathbf{m}(\mathbf{\Omega}) \right) - 1 \right]^{-1} \tag{1.33}$$

is the minimum of the radiative entropy under the constraint of an appropriate reconstruction of the considered moments model :

$$H^\star(B) = \min_{I \geq 0} \left\{ H^\star(I) = \langle \mathbf{m} I \rangle = (E_R, \mathbf{F}_R)^T \right\}, \tag{1.34}$$

where $\vec{\alpha} \in \mathbb{R}^M$ is the vector of Lagrangian multiplicators and $(E_R, \mathbf{F}_R)^T$ is the moments vector.

Proof. The following minimisation problem with equality constraint :

$$\min_{I \geq 0} \left\{ H^\star(I) = \langle \mathbf{m} I \rangle = (E_R, \mathbf{F}_R)^T \right\}, \tag{1.35}$$

is equivalent to the determination of the following Lagrangian point :

$$\mathcal{L}(I, \vec{\alpha}) = H^\star(I) - \vec{\alpha} \cdot ((E_R, \mathbf{F}_R)^T - \langle \mathbf{m} I \rangle), \tag{1.36}$$

where $\vec{\alpha} \in \mathbb{R}^M$ is the vector of Lagrangian multiplicators. These multiplicators are fully defined from the constraint. The constraint $\langle \mathbf{m} I \rangle = (E_R, \mathbf{F}_R)^T$ is realised by definition, the solution B of this minimisation problem has to satisfy, for all $I \geq 0$:

$$\begin{aligned} \partial_B \mathcal{L}(B, \vec{\alpha})(I) &= \langle (\partial_B h^\star(B) + \vec{\alpha} \cdot \mathbf{m}) I \rangle = 0, \\ &= \langle (\partial_n h^\star(n) \frac{c^2}{2h\nu^3} + \vec{\alpha} \cdot \mathbf{m}) I \rangle = 0, \\ &= \langle (-\frac{k}{hc\nu} ln(1 + \frac{1}{n}) + \vec{\alpha} \cdot \mathbf{m}) I \rangle = 0, \end{aligned} \tag{1.37}$$

where n is the population number density. The solution of this equation is also solution of :

$$-\frac{k}{hc\nu}ln(1+\frac{1}{n})+\vec{\alpha}\cdot\mathbf{m})I=0, \tag{1.38}$$

that is to say, replacing $\vec{\alpha}$ with a normalised multiplicator $\vec{\alpha}$:

$$B=\frac{2h\nu^3}{c^2}\left[exp(\frac{h\nu}{kT}\vec{\alpha}\cdot\mathbf{m})-1\right]^{-1}, \tag{1.39}$$

where $\vec{\alpha}\in\mathbb{R}^M$ is determined with the constraint $\langle\mathbf{m}I\rangle=(E_R,\mathbf{F}_R)^T$, then :

$$(E_R,\mathbf{F}_R)^T=\langle\mathbf{m}B(\vec{\alpha})\rangle=\frac{1}{c}\int_0^\infty\int_{S^2}\frac{2h\nu^3}{c^2}\mathbf{m}\left[exp(\frac{h\nu}{kT}\vec{\alpha}\cdot\mathbf{m})-1\right]^{-1}d\nu d\Omega. \tag{1.40}$$

□

Then, while the P_1 system uses the function $I(T)=B(T)(\alpha+\vec{\beta}.\mathbf{\Omega})$, let us write the following function, equivalent to (1.33), that is used in the M_1 model :

$$I(T)=\frac{2h\nu^3}{c^2}\left[exp\left(\frac{h\nu}{kT}(\alpha-\vec{\beta}.\mathbf{\Omega})\right)-1\right]^{-1}, \tag{1.41}$$

where α and $\vec{\beta}$ are Lagrangian multiplicators to be determined. We now therefore have at our disposal a system which is hyperbolic symmetrizable and minimises the entropy (see [16]).

At this point of the main variables presentation, let us introduce the Eddington factor χ (see [33]) :

$$\chi=\frac{3+4f^2}{5+2\xi}, \tag{1.42}$$

where $\xi=\sqrt{4-3f^2}$. And the Eddington tensor is defined such that :

$$\mathbf{P}_R=\mathbf{D}_RE_R, \tag{1.43}$$

where :

$$\mathbf{D}_R=\frac{1-\chi}{2}Id+\frac{3\chi-1}{2}\frac{\mathbf{f}}{f}\otimes\frac{\mathbf{f}}{f}. \tag{1.44}$$

Introducing the Eddington tensor, the M_1 model can be written :

$$\begin{cases}\partial_tE_R+div(\mathbf{F}_R)=c\sigma(aT^4-E_R),\\ \partial_t\mathbf{F}_R+c^2div(\mathbf{D}_RE_R)=-c\sigma\mathbf{F}_R,\\ \partial_t(\rho C_vT)=-c\sigma(aT^4-E_R),\end{cases} \tag{1.45}$$

where σ is a constant opacity over the whole spectrum, so it does not depend on the frequency ν. The third equation is representative of the interaction of radiation with the matter.

An important property of the M_1 model is that it recovers the equilibrium diffusion regime. Indeed, assuming that the opacity is large, we can rescale the M_1 system so that the Knudsen number ϵ appears in front of the time derivative term (long time approximation) and in the relaxation term (near equilibrium hypothesis) :

$$\epsilon\partial_t E_R + div(\mathbf{F}_R) = \frac{c\sigma}{\epsilon}(aT^4 - E_R), \tag{1.46}$$

$$\epsilon\partial_t F_R + c^2 div(\mathbf{P}_R) = -\frac{c\sigma}{\epsilon}\mathbf{F}_R, \tag{1.47}$$

$$\epsilon\partial_t(\rho C_v T) = -\frac{c\sigma}{\epsilon}(aT^4 - E_R). \tag{1.48}$$

An asymptotic expansion around $\epsilon = 0$ gives the usual near equilibrium behavior. If we set $T = T_0 + \epsilon T_1 + \epsilon^2 T_2 + ...$, we get at the leading order, from Equations (1.46) and (1.47), that :

$$E_0 = aT_0^4, \tag{1.49}$$

$$\mathbf{F}_0 = 0. \tag{1.50}$$

At the next order, using Equation (1.47), the flux can be written as :

$$\mathbf{F}_1 = -\frac{c}{\sigma}div(\mathbf{P}_0) = -\frac{c}{3\sigma}a\nabla T_0^4. \tag{1.51}$$

Finally, summing Equation (1.46) and (1.48) at the following order leads to :

$$\partial_t(\rho C_v T_0 + aT_0^4) - div(\frac{4cT_0^3}{3\sigma}\nabla T_0) = 0, \tag{1.52}$$

which is the equilibrium diffusion equation.

We have now presented the M_1 model in its general form, as well as the associated radiative variables. The work realised in this thesis consists in solving this system as much precisely as possible. This hyperbolic system with a relaxation source term is solved through a finite volume scheme.

1.4 Structure of the macroscopic M_1 system

From the construction of the M_1 system, we know that it is hyperbolic symmetrizable. For the general two dimensional form, let us introduce the notations :

$$W = \begin{pmatrix} E \\ F_x \\ F_y \end{pmatrix}, \mathcal{F} = \begin{pmatrix} F_x \\ c^2 P_{xx} \\ c^2 P_{xy} \end{pmatrix}, \mathcal{G} = \begin{pmatrix} F_y \\ c^2 P_{xy} \\ c^2 P_{yy} \end{pmatrix}, \tag{1.53}$$

and the matrices :

$$M_A = \partial_W \mathcal{F},\ M_B = \partial_W \mathcal{G}. \tag{1.54}$$

We then express the Jacobian matrices of the $\mathcal{F}$ and $\mathcal{G}$ fluxes. As the system $\partial_t W + \partial_W \mathcal{F} + \partial_W \mathcal{G} = 0$ is invariant through rotation, we can restrain the study to the x-direction. The matrice M_A contains the following coefficients :

$$M_A = \begin{pmatrix} 0 & 1 & 0 \\ \frac{(2f^2-3f_y^2)(\chi-f\chi')+f_y^2}{2f^2} & -\frac{f_x f_y^2}{2f^4}\theta + \frac{f_x\chi'}{f} & \frac{f_x^2 f_y^2}{2f^4}\theta - \frac{f_y^2\chi'}{2f} \\ \frac{f_x f_y}{2f^2}(3\chi - 3f\chi' - 1) & \frac{f_x^2 f_y}{2f^4}\theta + \frac{f_y}{2f^2}(3\chi-1) & \frac{f_x f_y^2}{4f^4}\theta + \frac{f_x}{2f^2}(3\chi-1) \end{pmatrix} \quad (1.55)$$

where $\theta = 2 + 3f\chi' - 6\chi$. And the matrix M_B is of the same form with f_x replacing f_y. The eigenvalues of matrix M_A are :

$$\begin{aligned} \lambda^{\pm} &= c\left(\frac{f_x}{\xi} \pm \frac{\sqrt{2}\sqrt{(\xi-1)(\xi+2)(2(\xi-1)(\xi+2)+3f_y^2)}}{\sqrt{3}\xi(\xi+2)}\right), \\ \lambda^0 &= c\frac{(2-\xi)f_x}{f^2}. \end{aligned} \quad (1.56)$$

We do not specify here the eigenvectors for the formulas are too large in the formulation known so far.

In Figure 1.2, the dimensionless eigenvalues (i.e. λ/c) of the Jacobian matrix are given as functions of f_x, respectively for $f_y = 0$ and $f_y = \sqrt{3}/2$. Let us remark that

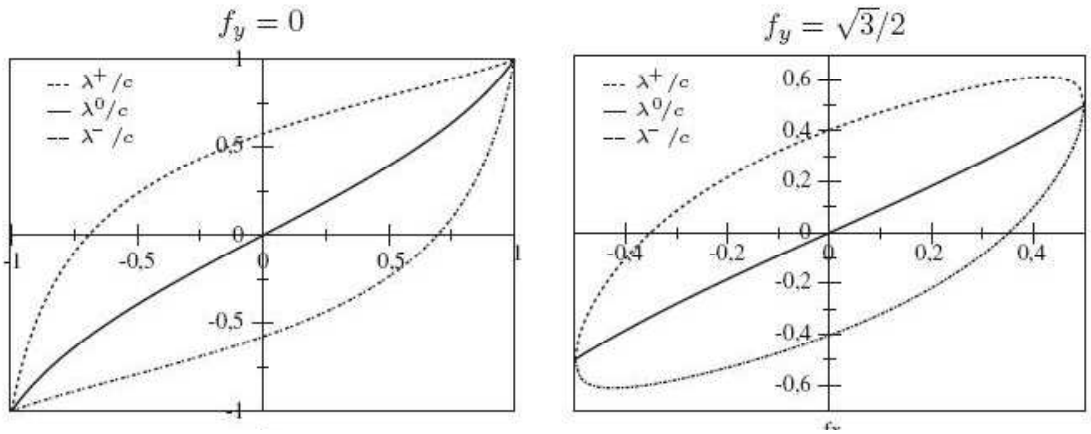

FIGURE 1.2 – Eigenvalues for the hyperbolic M_1 system

these eigenvalues are equal to $\lambda^{\pm} = \pm c/\sqrt{3}$ and $\lambda^0 = 0$ at the equilibrium (when $f_x = f_y = 0$). It illustrates well that the isotropic emission of photons is predominant at the equilibrium. On the contrary, in the case of a strong non-equilibrium (when $|f_x|$ tends to 1), the eigenvalues tend to the speed of light c. In this situation, the photons then all travel at the same speed and towards the same direction (or that the underlying radiative intensity tends towards a Dirac which is called the free streaming regime).

Note that the characteristic fields associated with the eigenvalues $\lambda^{\pm}$ are genuinely nonlinear as $\nabla_W \lambda^{\pm}.r^{\pm} \neq 0$ where $r^{\pm}$ are the corresponding eigenvectors. And

the characteristic field associated with λ^0 is linearly degenerate because $\nabla_W \lambda^0 . r^0 = 0$. These three waves generated by the system are either rarefaction or shock waves in the case of nonlinear fields, either contact discontinuities for linearly degenerate fields. The interest of linearly degenerate fields is that the Riemann invariants are constant through the contact discontinuity.

Definition 1. *A Riemann invariant associated with the j^{th} field is a function $\varphi(W)$ such that :*

$$\nabla \varphi(W).r_j = 0, \tag{1.57}$$

where r_j is the j^{th} eigenvector of the Jacobian matrix.

The formulary that we detail below will be useful in the following. The Lagrangian multiplicators α and $\vec{\beta}$ are used in most formulations and so we here specify them.

Let us start from the relation (1.41) where Lagrangian multiplicators are involved in the radiative intensity expression. We integrate the radiative intensity with (1.3) in order to obtain its three radiative moments. The radiative energy, the radiative flux and radiative pressure tensor are therefore determined as functions of α and $\vec{\beta}$:

$$\begin{aligned} E_R &= \frac{aT^4}{\alpha^4} \frac{3+\beta^2}{3(1-\beta^2)^3}, \\ \mathbf{F}_R &= \frac{caT^4}{\alpha^4} \frac{4\vec{\beta}}{3(1-\beta^2)^3}, \\ \mathbf{P}_R &= \left(\frac{1-\beta^2}{3+\beta^2} Id + \frac{3+\beta^2}{4} \mathbf{f} \otimes \mathbf{f} \right) E_R, \end{aligned} \tag{1.58}$$

where $\mathbf{f} = \frac{\mathbf{F}_R}{cE_R}$. Identifying the radiative pressure expression with the one using the Eddington tensor, we obtain $\vec{\beta}$ as a function of $\mathbf{f}$:

$$\vec{\beta} = \frac{3\chi - 1}{2} \frac{\mathbf{f}}{f^2} = \frac{(2-\xi)\mathbf{f}}{f^2}. \tag{1.59}$$

Therefore it comes the following relation between the contact wave speed and $\vec{\beta}$:

$$\lambda^0 = c\beta. \tag{1.60}$$

From (1.58) and the definition of $\mathbf{f}$, we can also write the limited flux as :

$$\mathbf{f} = \frac{4\vec{\beta}}{4+\beta^2}. \tag{1.61}$$

The first step of the study reported here is realised with the M_1 system (1.30) reduced to its conservative form. The source terms will be taken into account from Section 3.2 through the asymptotic preserving procedure. Let us then write System (1.30) without the source terms :

$$\begin{cases} \partial_t E_R + div(\mathbf{F}_R) = 0, \\ \partial_t \mathbf{F}_R + c^2 div(\mathbf{P}_R) = 0. \end{cases} \tag{1.62}$$

Inspired by Després [11], we choose to introduce the variable Π defined as :

$$\Pi = \frac{1-\beta^2}{3+\beta^2} E_R, \tag{1.63}$$

so that it comes the following expression for the radiative pressure $\mathbf{P}_R$:

$$\mathbf{P}_R = \frac{\vec{\beta} \otimes \mathbf{F}_R}{c} + \Pi. \tag{1.64}$$

And we can write the second equation in a form similar to the momentum conservation equation, so it comes :

$$\begin{cases} \partial_t E_R + div(\mathbf{F}_R) = 0, \\ \partial_t \mathbf{F}_R + c^2 div(\dfrac{\vec{\beta} \otimes \mathbf{F}_R}{c} + \Pi) = 0. \end{cases} \tag{1.65}$$

As we will first work with the M_1 system without considering the source terms, the 1D system will be written as :

$$\begin{cases} \partial_t E + \partial_x F_x = 0, \\ \partial_t F_x + c^2 \partial_x P_{xx} = 0, \\ \partial_t F_y + c^2 \partial_x P_{xy} = 0, \end{cases} \tag{1.66}$$

where $P_{xx} = \frac{\beta_x F_x}{c} + \Pi$, and $P_{xy} = \frac{\beta_x F_y}{c}$.

Let us note that in a first step, in order to simplify the study and scheme development, we plan to look at the subsystem :

$$\begin{cases} \partial_t E + \partial_x F_x = 0, \\ \partial_t F_x + c^2 \partial_x P_{xx} = 0, \end{cases}$$

where only the two nonlinear fields are involved (the stationary contact is not part of the structure anymore). Once the scheme is constructed with such a simplified version, we will consider the full 1D system (1.66). And then, the 2D scheme will be quite straightforward as it acutally sums up the 1D calculations in each direction.

Chapitre 2

Numerical approximation of the monodimensional M_1 model

2.1 Introduction

In the precedent chapter, we have presented an overview of radiative transfer and its applications, and have introduced the M_1 model. This model has several advantages of interest for our purposes, unlike the statistical (Monte-Carlo) or direct method, and even the diffusion models. Indeed, the microscopic approaches, such as the statistical and direct methods, aim to look at groups of photons which direction and frequency are randomly set. The mean free path of the photons until they are absorbed or scattered is related to the medium opacity. Considering that it is longer for a photon to go from one point to an other in an optically thick region, it then turns out that computations with these microscopic methods are longer in opaque mediums than in transparent mediums. These microscopic methods are then not profitable for our applications that not only involve optically thin mediums. And as for the coupling with hydrodynamic codes, it is even more expansive from a computational point of view as the radiation transport routine is called several times (this phenomenon being faster than the hydrodynamic phenomena).

The alternative to perform cheaper calculation is macroscopic methods. There exist some diffusion models but they are indeed pertinent only in the diffusion regime, which is not convenient in our case. Other possible macroscopic models are moments models obtained after integration of the Radiative Transfer Equation over directions and frequencies. The first one is the P_1 model. However, this model is not behaving well enough in the transport regime. A solution could have been to couple these models that deal properly with diffusion regimes to a microscopic method. This coupling remains too much complex to realise, and in addition the transition regime between diffusion and transport would not be properly ensured, and the computational cost would remain too much important. The M_1 model is interesting from this point of view : it is accurate enough over a wide range of radiation transfer regimes which is crucial for our applications.

The M_1 model introduced by Dubroca and Feugeas [17] preserves several crucial properties of the radiative transfer equation such as the energy positiveness, the flux

limitation and the conservation of the total energy. When approximating solutions for this hyperbolic system with source terms, it is important to ensure the preservation of these properties. In this section, we focus on the derivation of numerical schemes meeting this requirement.

Considering a proper Godunov method remains so far out of reach for the M_1 model as the Riemann problem is not known yet. The use of approximate methods is then mandatory. Schemes are developed, each involving a number of constraints.

Dubroca and Feugeas [17] first proposed the use of a standard HLL scheme (see Harten, Lax and Van Leer [27]). The main benefit of this numerical approximation is an easy preservation of the admissible states for a viscous discretisation. But because this method does not take the contact wave into account, and averages the solution over a single intermediate state, it sometimes remains too much diffusive (see [10] and [6] where the authors modify the HLL Riemann solver to introduce the source terms) and needs arose for a more accurate approximation of the numerical solution. We then undertook to build new solvers able to capture the contact wave, such as a relaxation scheme, and an HLLC type scheme. Even if the resulting relaxation scheme does not turn out to be accurate enough, it helped in the suggestion of the appropriate linearisations for the construction of an HLLC type scheme. This HLLC scheme gives results with a good accuracy. In addition, it allows to cover the asymptotic diffusion regime in the limit of large opacities and then satisfies the asymptotic preserving property of the M_1 model.

A full two dimensional study will be done in the following chapters. For now, and for the sake of simplicity in the numerical tool development, a one space dimension study is realised. That is to say, in this chapter, we will consider the following 1D subsystem of (1.66) without source terms :

$$\begin{cases} \partial_t E + \partial_x F_x = 0, \\ \partial_t F_x + c^2 \partial_x P_{xx} = 0. \end{cases} \tag{2.1}$$

And after an introduction about the finite volume method, the relaxation and HLLC schemes are successively developed and presented.

2.2 Finite volume method

To present the finite volume procedure, let us use as an example the following scalar conservation law in differential form :

$$\partial_t u + \partial_x f(u) = 0, \tag{2.2}$$

where $f(u)$ is the flux function. The integral formulation of the conservation law may be written :

$$\int_{x_1}^{x_2} u(x,t_2)dx = \int_{x_1}^{x_2} u(x,t_1)dx + \int_{t_1}^{t_2} f(u(x_1,t))dt - \int_{t_1}^{t_2} f(u(x_2,t))dt. \tag{2.3}$$

This integral formulation will allow us to design numerical methods for our specific needs. Indeed, the integral formulation has the advantage to allow an extension of the class of admissible solutions to include discontinuous solutions.

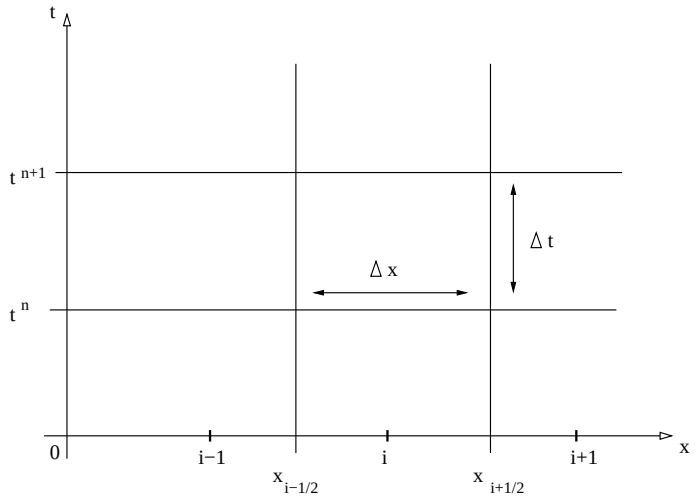

FIGURE 2.1 – Discretisation domain

Let us first set the working space sketched as in Figure 2.1 where we aim to work in the cell (control volume) $C_i = (x_{i-\frac{1}{2}}, x_{i+\frac{1}{2}}) \times (t^n, t^{n+1})$ where Δx and Δt are set constant. The discrete times are defined by : $t^n = n\Delta t$, $n \in \mathbb{N}$. Working in such a discretised domain, the solution $u(x,t)$, $x \in \mathbb{R}$, $t \geq 0$, is discretised over this domain in order to be evaluated.

At the date $t = 0$, the approximation of the initial data is expressed as :

$$u_i^0 = \frac{1}{\Delta x} \int_{x_{i-\frac{1}{2}}}^{x_{i+\frac{1}{2}}} u(x,0)dx.$$

Then, at the date t^n, we assume as known the piecewise constant approximation of $u(x,t)$ denoted $u^h(x,t^n)$, and defined by :

$$u^h(x,t^n) = u_i^n \quad \text{if} \quad x \in (x_{i-\frac{1}{2}}, x_{i+\frac{1}{2}}). \tag{2.4}$$

Now, this approximate solution is evolved in time to the date $t^n + \Delta t$ to define $u^h(x, t^n + \Delta t)$. To evaluate the sequence u_i^{n+1} we consider a Godunov approach.

It is a conservative method, where the intercell numerical fluxes (approximations of the physical fluxes) are computed using solutions of local Riemann problems. The successive Riemann problems do not interact as long as Δt is small enough. This is ensured with an appropriate determination of the time step given by the following CFL like condition :

$$\Delta t \leq \frac{1}{2} \frac{\Delta x}{\lambda_{max}^n}, \tag{2.5}$$

where $\lambda_{max}^n = \max_i |f'(u_i^n)|$. And we are then able to solve these successive Riemann problems for a small enough time step Δt, in order to evolve the solution to the time t^{n+1}.

Indeed, let us assume a pair of constant states (u_i^n, u_{i+1}^n) separated by a discontinuity at the boundary $x_{i+\frac{1}{2}}$. The local Riemann problem is then defined as :

$$\begin{cases} \partial_t u + \partial_x f(u) = 0, \\ \\ u_0(x) = \begin{cases} u_i^n \quad if \quad x < x_{i+\frac{1}{2}}, \\ u_{i+1}^n \quad if \quad x > x_{i+\frac{1}{2}}. \end{cases} \end{cases} \tag{2.6}$$

of which we need to find the solution at Δt. The exact solution is known and we note it

$$u_{\mathcal{R}}\left(\frac{x - x_{i+\frac{1}{2}}}{\Delta t}; u_i^n, u_{i+1}^n\right).$$

Under the CFL like condition (2.5), we define the juxtaposition of the non interacting Riemann solution as follows :

$$u^h(x, t^n + \Delta t) = u_{\mathcal{R}}\left(\frac{x - x_{i+\frac{1}{2}}}{\Delta t}; u_i^n, u_{i+1}^n\right) \quad \text{if} \quad x \in (x_i, x_{i+1}).$$

The solution u_i^{n+1} is obtained as the L^2-projection of the solutions of non-interacting Riemann problems. This is written :

$$u_i^{n+1} = \frac{1}{\Delta x} \int_{x_{i-\frac{1}{2}}}^{x_{i+\frac{1}{2}}} u^h(x, t^n + \Delta t) dx. \tag{2.7}$$

We now use the integral form (2.3) of the conservation law to write :

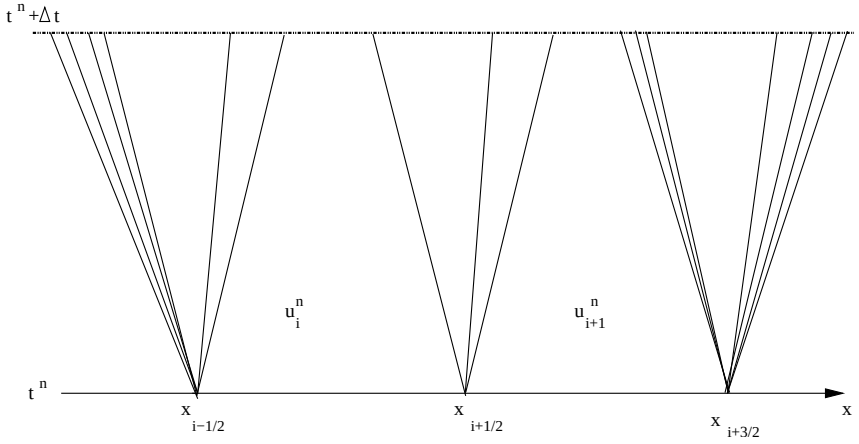

FIGURE 2.2 – Riemann problems

$$\begin{aligned} \int_{x_{i-\frac{1}{2}}}^{x_{i+\frac{1}{2}}} u^h(x, t^n + \Delta t) dx = & \int_{x_{i-\frac{1}{2}}}^{x_{i+\frac{1}{2}}} u^h(x, t^n) dx \\ & + \int_{t^n}^{t^n + \Delta t} f(u^h(x_{i-\frac{1}{2}}, t)) dt - \int_{t^n}^{t^n + \Delta t} f(u^h(x_{i+\frac{1}{2}}, t)) dt, \end{aligned} \tag{2.8}$$

and, using the cell averages definitions given by (2.7), it comes :

$$u_i^{n+1} = u_i^n + \frac{\Delta t}{\Delta x}\left(f_{i-\frac{1}{2}} - f_{i+\frac{1}{2}}\right), \tag{2.9}$$

where the numerical flux is $f_{i+\frac{1}{2}} = f(u^h(x_{i+\frac{1}{2}}, t^n + \Delta t))$.

Godunov's scheme is the standard basis of finite volume methods, leading to robust and stable schemes. In our case, as we do not know the exact solution of the Riemann problem , we plan to use approximate methods to approximate the weak solutions of the M_1 hyperbolic system. The Harten-Lax-Van Leer [27] scheme is a classical approximate method that we present in the next section.

2.3 The HLL scheme

The so-called HLL scheme has been developed by Harten, Lax and Van Leer [27] with the purpose of computing the Godunov-type flux in order to obtain an approximate solution for the Riemann problem. With this approach, introducing an appropriate linearisation, the solution of the Riemann problem is approximated. Starting from a two waves configuration separating three constant states, and assuming the wave speeds are known, the application of the integral form of the conservation laws allows to approximate the flux. The resulting HLL Riemann solvers constitute very efficient and robust approximate methods.

This HLL scheme was so far the only scheme at our disposal for solving System (2.1). It is actually quite straightforward to apply to radiative transfer. We will here sketch its principle in order to set the starting point of the study that follows.

General relations. The approximate solution of the Riemann problem is defined as :

$$U(x, \Delta t) = \begin{cases} U_L & \text{if } x < b_L \Delta t, \\ U^\star & \text{if } x \in (b_L \Delta t, b_R \Delta t), \\ U_R & \text{if } x > b_R \Delta t, \end{cases} \tag{2.10}$$

where the wavespeeds b_L and b_R verify $b_L < b_R$. For the sake of simplicity, and for the rest of the study, we choose to work with $b_L < 0$ and $b_R > 0$.

The HLL Riemann solver involves a intermediate region that consists of a single constant state. The $U^\star$ constant state has its expression obtained from the integral form of the conservation law in the control volume $(x_1, x_2) \times (0, \Delta t)$ (see Figure 2.3), where $x_1 < x_2$. It comes :

$$\int_{x_1}^{x_2} U(x, \Delta t)dx = \int_{x_1}^{x_2} U(x, 0)dx + \int_0^{\Delta t} F(U(x_1, t))dt - \int_0^{\Delta t} F(U(x_2, t))dt. \tag{2.11}$$

Over the interval $(0, \Delta t)$, the function such that $t \longrightarrow F(U(x_i, t))$ is constant and we have :

$$F(U(x_1, t)) = F(U_L) \quad \text{and} \quad F(U(x_2, t)) = F(U_R).$$

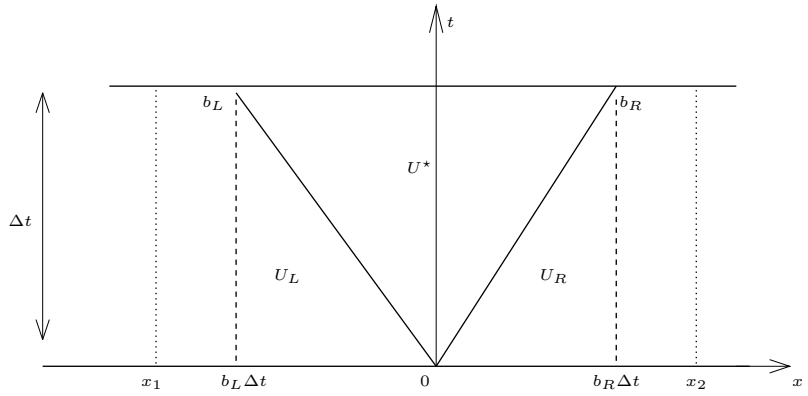

FIGURE 2.3 – HLL scheme - Riemann problem

In order to simplify the notations, we note $F_L = F(U_L)$ and $F_R = F(U_R)$, and it comes :

$$\int_{x_1}^{x_2} U(x, \Delta t)dx = x_2 U_R - x_1 U_L + \Delta t(F_L - F_R). \tag{2.12}$$

Let us split the integral on the left-hand side of (2.11) and then evaluate the first and third terms. With $x_1 < b_L$ and $x_2 > b_R$ so that the exact dependance cone is included into the control volume, we obtain :

$$\int_{x_1}^{x_2} U(x, \Delta t)dx = \int_{b_L\Delta t}^{b_R\Delta t} U(x, \Delta t)dx + (b_L\Delta t - x_1)U_L + (x_2 - b_R\Delta t)U_R. \tag{2.13}$$

The relations (2.12) and (2.13) now give :

$$\int_{b_L\Delta t}^{b_R\Delta t} U(x, \Delta t)dx = \Delta t(b_R U_R - b_L U_L + F_L - F_R). \tag{2.14}$$

We remind that $U(x, \Delta t)$ is constant equal to $U^\star$ over $(b_L\Delta t, b_R\Delta t)$. we can then write :

$$\int_{b_L\Delta t}^{b_R\Delta t} U(x, \Delta t)dx = \Delta t(b_R - b_L)U^\star. \tag{2.15}$$

And thanks to (2.14), we obtain :

$$U^\star = \frac{b_R U_R - b_L U_L}{b_R - b_L} - \frac{1}{b_R - b_L}(F_R - F_L). \tag{2.16}$$

Now let us apply the above procedure to the control volume $(x_1, 0) \times (0, \Delta t)$ (see Figure 2.3), we thus have :

$$\int_{b_L\Delta t}^{0} U(x, \Delta t)dx = -\Delta t b_L U_L + \Delta t(F_L - F_{0L}), \tag{2.17}$$

where F_{0L} is the flux $F(U)$ at $x = 0$. Equation (2.17) leads to :

$$F_{0L} = F_L - b_L U_L - \frac{1}{\Delta t} \int_{b_L \Delta t}^{0} U(x, \Delta t) dx, \tag{2.18}$$

and in the same way, when working in the control volume $(0, x_2) \times (0, \Delta t)$, we have :

$$F_{0R} = F_R - b_R U_R + \frac{1}{\Delta t} \int_{0}^{b_R \Delta t} U(x, \Delta t) dx. \tag{2.19}$$

Let us now substitute the integrand in (2.18) and (2.19) by its expression (2.15) involving $U^\star$. We thus obtain a flux continuity property, which is :

$$F_{0L} = F_{0R} = \tilde{F}.$$

And we replace the fluxes F_{0L} and F_{0R} at $x = 0$ by the corresponding intercell flux $\tilde{F}$, we obtain the two relations :

$$\begin{aligned} \tilde{F} &= F_L + b_L(U^\star - U_L), \\ \tilde{F} &= F_R + b_R(U^\star - U_R), \end{aligned} \tag{2.20}$$

which are similar to the Rankine-Hugoniot relations. The HLL Riemann solver is often assimilated to the direct application of the Rankine-Hugoniot equations. From System (2.20) involving two equations and two unknowns, it is straightforward to derive the expression for the intermediate state $U^\star$ and the intermediate flux $\tilde{F}$.

Now, from a known solution at the date t^n, we obtain the solution at the date t^{n+1} as the juxtaposition of the non interacting Riemann problems, and integrated over the cell $(x_{i-\frac{1}{2}}, x_{i+\frac{1}{2}})$:

$$U_i^{n+1} = \frac{1}{\Delta x} \int_{x_{i-\frac{1}{2}}}^{x_{i+\frac{1}{2}}} U(x, t^n + \Delta t) dx. \tag{2.21}$$

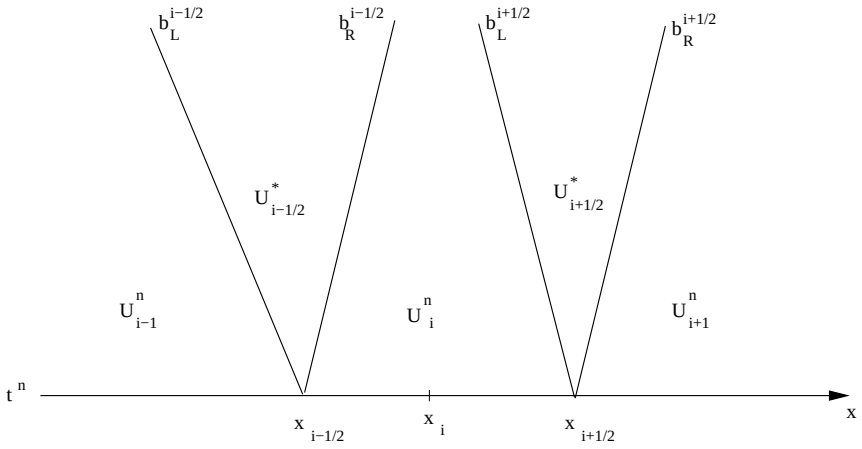

FIGURE 2.4 – HLL scheme

When working in a discretised domain such as displayed in Figure 2.1, the final scheme may be written as :

$$U_i^{n+1} = U_i^n - \frac{\Delta t}{\Delta x}(\tilde{F}_{i+\frac{1}{2}} - \tilde{F}_{i-\frac{1}{2}}), \tag{2.22}$$

where, according to (2.20) :

$$\tilde{F}_{i+\frac{1}{2}} = \frac{b_R^{i+\frac{1}{2}} F(U_i) - b_L^{i+\frac{1}{2}} F(U_{i+1})}{b_R^{i+\frac{1}{2}} - b_L^{i+\frac{1}{2}}} + \frac{b_R^{i+\frac{1}{2}} b_L^{i+\frac{1}{2}}}{b_R^{i+\frac{1}{2}} - b_L^{i+\frac{1}{2}}} \left(F(U_{i+1}) - F(U_i)\right), \tag{2.23}$$

and :

$$U^\star_{i+\frac{1}{2}} = \frac{b_R^{i+\frac{1}{2}} U_{i+1} - b_L^{i+\frac{1}{2}} U_i}{b_R^{i+\frac{1}{2}} - b_L^{i+\frac{1}{2}}} - \frac{1}{b_R^{i+\frac{1}{2}} - b_L^{i+\frac{1}{2}}}(F_{i+1} - F_i). \tag{2.24}$$

Application to radiative transfer. Making use of the preceding relations for the HLL Riemann solver, let us write the Rankine-Hugoniot like relations (2.20) through the numerical waves of speed b_L and b_R. These relations are :

$$\begin{cases} \tilde{\mathcal{F}} - \mathcal{F}(U_L) = b_L(U^\star - U_L), \\ \tilde{\mathcal{F}} - \mathcal{F}(U_R) = b_R(U^\star - U_R). \end{cases} \tag{2.25}$$

From them, we can easily derive expressions for $U^\star$ and $\tilde{\mathcal{F}}$.

$$\begin{aligned} U^\star &= \frac{b_R U_R - b_L U_L}{b_R - b_L} - \frac{1}{b_R - b_L}(\mathcal{F}(U_R) - \mathcal{F}(U_L)), \\ \tilde{\mathcal{F}} &= \frac{b_R \mathcal{F}(U_L) - b_L \mathcal{F}(U_R)}{b_R - b_L} + \frac{b_R b_L}{b_R - b_L}(U_R - U_L). \end{aligned} \tag{2.26}$$

Note that as in any approximate Riemann solver we have $\tilde{\mathcal{F}} \neq \mathcal{F}(U^\star)$. As they will be used later, we explicitly write here the HLL [27] approximate solutions in the star region and the corresponding flux functions :

$$\begin{aligned} E^\star_{HLL} &= \frac{b_R E_R - b_L E_L}{b_R - b_L} - \frac{1}{b_R - b_L}(F_{x,R} - F_{x,L}), \\ F^\star_{x,HLL} &= \frac{b_R F_{x,R} - b_L F_{x,L}}{b_R - b_L} - \frac{c^2}{b_R - b_L}(P_{xx,R} - P_{xx,L}), \\ \tilde{F}_{x,HLL} &= \frac{b_R F_{x,L} - b_L F_{x,R}}{b_R - b_L} + \frac{b_R b_L}{b_R - b_L}(E_R - E_L), \\ \tilde{P}_{xx,HLL} &= \frac{b_R P_{xx,L} - b_L P_{xx,R}}{b_R - b_L} + \frac{b_R b_L}{c^2(b_R - b_L)}(F_{x,R} - F_{x,L}). \end{aligned} \tag{2.27}$$

We now write the full HLL scheme, we can write E_i^{n+1} and $F_{x,i}^{n+1}$ such as :

$$\begin{cases} E_i^{n+1} = E_i^n - \dfrac{\Delta t}{\Delta x}(\tilde{F}_{x,HLL}^{i+\frac{1}{2}} - \tilde{F}_{x,HLL}^{i-\frac{1}{2}}), \\ F_{x,i}^{n+1} = F_{x,i}^n - \dfrac{\Delta t}{\Delta x}(\tilde{P}_{xx,HLL}^{i+\frac{1}{2}} - \tilde{P}_{xx,HLL}^{i-\frac{1}{2}}), \end{cases} \tag{2.28}$$

where :

$$\begin{cases} \tilde{F}^{i+\frac{1}{2}}_{x,HLL} = \dfrac{b_R^{i+\frac{1}{2}} F^n_{x,i} - b_L^{i+\frac{1}{2}} F^n_{x,i+1}}{b_R^{i+\frac{1}{2}} - b_L^{i+\frac{1}{2}}} + \dfrac{b_R^{i+\frac{1}{2}} b_L^{i+\frac{1}{2}}}{b_R^{i+\frac{1}{2}} - b_L^{i+\frac{1}{2}}}(E^n_{i+1} - E^n_i), \\ \tilde{P}^{i+\frac{1}{2}}_{xx,HLL} = \dfrac{b_R^{i+\frac{1}{2}} P^n_{xx,i} - b_L^{i+\frac{1}{2}} P^n_{xx,i+1}}{b_R^{i+\frac{1}{2}} - b_L^{i+\frac{1}{2}}} + \dfrac{b_R^{i+\frac{1}{2}} b_L^{i+\frac{1}{2}}}{c^2(b_R^{i+\frac{1}{2}} - b_L^{i+\frac{1}{2}})}(F^n_{x,i+1} - F^n_{x,i}), \end{cases} \tag{2.29}$$

and with the CFL like condition :

$$\frac{\Delta t}{\Delta x} \max_{i\in\mathbb{Z}}(b_{i+\frac{1}{2}}) \leq \frac{1}{2}. \tag{2.30}$$

We will see later that it is more convenient to work with the constant wave speeds $b_L = -c$ and $b_R = +c$. The scheme then writes as (2.28) where the intermediate fluxes are simply written as :

$$\begin{cases} \tilde{F}^{i+\frac{1}{2}}_{x,HLL} = \dfrac{F^n_{x,i} + F^n_{x,i+1}}{2} - \dfrac{c}{2}(E^n_{i+1} - E^n_i), \\ \tilde{P}^{i+\frac{1}{2}}_{xx,HLL} = \dfrac{P^n_{xx,i} + P^n_{xx,i+1}}{2} - \dfrac{1}{2c}(F^n_{x,i+1} - F^n_{x,i}), \end{cases} \tag{2.31}$$

and with the CFL like condition :

$$\frac{c\Delta t}{\Delta x} \leq \frac{1}{2}. \tag{2.32}$$

This HLL scheme is stable but provides us with a quite viscous solution in the case of radiative transfer. The numerical viscosity comes from the presence of a single intermediate state. This property and the results obtained in numerical experiments (see Chapter 5) raise the need to have at our disposal a more accurate scheme.

These HLL schemes are indeed correct for many hyperbolic systems, however, for systems involving contact waves in between the non-linear fields, this two-wave assumption is not correct anymore. Indeed, when considering only two waves, an average is performed and then implies imprecisions. The resolution of physical features such as contact surfaces is therefore inaccurate. This will be clearly demonstrated by the shadow cone test case in Section 5.3. In order to improve the numerical accuracy, in the following sections, we developed two schemes able to capture the existing stationary contact wave. The first one is a relaxation-type scheme, and the second one is an HLLC-type scheme. These methods allow us to integrate the solution over two intermediate states and then to profit from a more accurate approximation of the Riemann solution.

2.4 The relaxation scheme

Relaxation solvers have been developed and studied in the Euler case in [9], where in particular Suliciu's relaxation system is presented (see also [2], [13], [15], [30], [31], [29] for more relaxation solvers for conservation laws).

Our purpose here is to approximate the solutions of the conservative form of the 1D M_1 model, where x-directed variables and matter interaction are not considered. Let us remind this system :

$$\begin{cases} \partial_t E + \partial_x F_x = 0, \\ \partial_t F_x + c^2 \partial_x P_{xx} = 0, \end{cases} \tag{2.33}$$

where :

$$P_{xx} = \left(\frac{1-\beta_x^2}{3+\beta_x^2} + \frac{3+\beta_x^2}{4} f^2 \right) E. \tag{2.34}$$

The numerical method is expected to preserve the physical properties of the model, and particular attention is paid to the stability of the scheme. Through an adequate reformulation, the weak solutions of system (2.33) are approximated by the weak solutions of a suitable system with singular perturbations.

2.4.1 Reformulation of the system

We decide to perform a reformulation, introducing new variables, allowing us to work with a relaxation system similar to some well-known systems (see [9], [11] and [12]).

Let us remind some relations associated to the selected M_1 model. From the model construction, the radiative energy E, radiative flux F_x and radiative pressure tensor P_{xx} are function of some Lagrangian multiplicators such as β_x. We have :

$$\begin{aligned} F_x &= \frac{4cE}{3+\beta_x^2}\beta_x, \\ P_{xx} &= \left(\frac{1-\beta_x^2}{3+\beta_x^2} Id + \frac{3+\beta_x^2}{4} f^2 \right) E, \end{aligned} \tag{2.35}$$

where the coefficient β_x intervenes in (1.41), and $f = \frac{4\beta_x}{3+\beta_x^2}$.

Resting on the parallel with hydrodynamics inspired by Després [12], we propose the following notations :

$$\begin{cases} E = \rho e, \\ F_x = \rho v, \end{cases} \tag{2.36}$$

where e is a radiative energy per unit mass, v is the photon velocity, and ρ is an arbitrary density to be defined. Let us introduce the variable Π set as :

$$\Pi = \frac{E(1-\beta_x^2)}{3+\beta_x^2}. \tag{2.37}$$

It comes :

$$P_{xx} = \frac{\beta_x F_x}{c} + \Pi. \tag{2.38}$$

It is then straightforward to write the relations :

$$\begin{cases} \rho v = c\beta_x(\rho e + \Pi), \\ P_{xx} = \dfrac{\rho v \beta_x}{c} + \Pi. \end{cases} \tag{2.39}$$

With these notations, system (2.33) can be written as :

$$\begin{cases} \partial_t \rho v + \partial_x(\rho v c\beta_x + c^2\Pi) = 0, \\ \partial_t \rho e + \partial_x c\beta_x(\rho e + \Pi) = 0. \end{cases} \tag{2.40}$$

Some similarities with the Euler equations are here remarkable such as the variable Π that appears to play the same role as the hydrodynamic pressure, and $c\beta_x$ reveals to be the contact Riemann invariant like the velocity u in the Euler equations. It then becomes evident that, with the notations (2.36) and the variable Π we have introduced, we can make a parallel between the Euler system of equations and (2.40). Note also that the velocity $c\beta_x$ and the pressure like Π are formally invariants across the arbitrarily added wave (later on, when we will consider the full 1D system (1.66), this Riemann solver with two intermediate states will help bringing more accuracy to the scheme). Setting $c\beta_x = v$, $\Pi = p$ and $c = 1$, we get back to the Euler equations.

Let us remind the 1D Euler conservative system :

$$\begin{cases} \partial_t \rho + \partial_x \rho v = 0, \\ \partial_t \rho v + \partial_x(\rho v^2 + p) = 0, \\ \partial_t \rho E + \partial_x(\rho E + p)v = 0. \end{cases} \tag{2.41}$$

We make use of this analogy with the Euler system of equations, and with the Suliciu model presented in [9], we propose an adequate relaxation model for (2.40). As it is done with the Euler system, we aim to relax the non-linearities introduced with the pressure Π, but also with the $c\beta_x$ velocity. The idea is actually to relax these system non-linearities thanks to new unknowns governed by pertinent equations.

Let us first introduce the variable q that will relax to Π. It is then possible to write the q relaxation equation :

$$\partial_t q + u\partial_x q + \frac{a^2}{\rho}\partial_x u = \frac{1}{\delta}(\Pi - q), \tag{2.42}$$

which can also be written in the conservative form :

$$\partial_t \rho q + \partial_x(\rho q u + a^2 u) = \frac{\rho}{\delta}(\Pi - q), \tag{2.43}$$

where $a \geq 0$ is a parameter to be determined, $\rho \geq 0$ is a density to be defined, and δ is a relaxation parameter.

Next, the $c\beta_x$ term is actually relaxed to a velocity u governed by the following equation :

$$\partial_t \rho u + \partial_x(\rho u^2 + q) = \frac{\rho}{\delta}(c\beta_x - u). \tag{2.44}$$

It comes the following model where ρ is not yet defined :

$$\begin{cases} \partial_t \rho u + \partial_x(\rho u^2 + q) = \dfrac{\rho}{\delta}(c\beta_x - u), \\ \partial_t \rho v + \partial_x(\rho v u + c^2 q) = 0, \\ \partial_t \rho e + \partial_x(\rho e + q)u = 0, \\ \partial_t \rho q + \partial_x(\rho q u + a^2 u) = \dfrac{\rho}{\delta}(\Pi - q). \end{cases} \tag{2.45}$$

First, with the introduction of the variable V defined as $V = v - c^2 u$, we obtain the following system :

$$\begin{cases} \partial_t \rho u + \partial_x(\rho u^2 + q) = \dfrac{\rho}{\delta}(c\beta_x - u), \\ \partial_t \rho V + \partial_x \rho V u = -\dfrac{c^2 \rho}{\delta}(c\beta_x - u), \\ \partial_t \rho e + \partial_x(\rho e + q)u = 0, \\ \partial_t q + u\partial_x q + \dfrac{a^2}{\rho}\partial_x u = \dfrac{\rho}{\delta}(\Pi - q). \end{cases} \tag{2.46}$$

Note that this obtained system is similar to the 2D Suliciu system for the Euler equations as soon as ρ satisfies a relevant continuity equation :

$$\partial_t \rho + \partial_x \rho u = 0.$$

The full considered relaxation model is thus given by :

$$\begin{cases} \partial_t \rho + \partial_x \rho u = 0, \\ \partial_t \rho u + \partial_x(\rho u^2 + q) = \dfrac{\rho}{\delta}(c\beta_x - u), \\ \partial_t \rho V + \partial_x \rho V u = -\dfrac{c^2 \rho}{\delta}(c\beta_x - u), \\ \partial_t \rho e + \partial_x(\rho e + q)u = 0, \\ \partial_t q + u\partial_x q + \dfrac{a^2}{\rho}\partial_x u = \dfrac{\rho}{\delta}(\Pi - q). \end{cases} \tag{2.47}$$

Lastly, in order to ease up the model analysis, we write System (2.47) in terms of primitive variables. We introduce the internal energy per unit mass ε such that $e = \varepsilon + \frac{u^2}{2}$. This enables us to write the conservative form of System (2.47). Then, the relaxation system to be considered in the following model analysis is :

$$\begin{cases} \partial_t \rho + \rho\partial_x u + u\partial_x \rho = 0, \\ \partial_t u + u\partial_x u + \dfrac{1}{\rho}\partial_x q = \dfrac{1}{\delta}(c\beta_x - u), \\ \partial_t V + u\partial_x V = -\dfrac{c^2}{\delta}(c\beta_x - u), \\ \partial_t \varepsilon + u\partial_x \varepsilon + \dfrac{q}{\rho}\partial_x u = 0, \\ \partial_t q + u\partial_x q + \dfrac{a^2}{\rho}\partial_x u = \dfrac{1}{\delta}(\Pi - q). \end{cases} \tag{2.48}$$

Let us define the relaxation primitive state vector as :

$$W = (\rho, u, V, \varepsilon, q).$$

This relaxation state vector W is expected to be in the following admissible space :

$$\Omega = \{(\rho, u, V, \varepsilon, q) \in \mathbb{R}^5, \rho > 0, u \in \mathbb{R}, V \in \mathbb{R}, \varepsilon > 0, q \in \mathbb{R}\}. \tag{2.49}$$

This relaxation state vector will be said to be at the equilibrium as soon as we have :

$$W = (\rho, u = c\beta_x, V, \varepsilon, q = \Pi).$$

Indeed, formally, let δ tend to zero, then u tends to $c\beta_x$ and q tends to Π. Then, from the equations governing ρv and ρe in System (2.40), we recover the equations governing the radiative energy and the radiative flux.

2.4.2 Riemann problem

We here study the solutions of the Riemann problem without the source terms. Let us consider the above System (2.48) without the source terms :

$$\begin{cases} \partial_t \rho + \rho \partial_x u + u \partial_x \rho = 0, \\ \partial_t u + u \partial_x u + \dfrac{1}{\rho} \partial_x q = 0, \\ \partial_t V + u \partial_x V = 0, \\ \partial_t \varepsilon + u \partial_x \varepsilon + \dfrac{q}{\rho} \partial_x u = 0, \\ \partial_t q + u \partial_x q + \dfrac{a^2}{\rho} \partial_x u = 0. \end{cases} \tag{2.50}$$

The given data for this Riemann problem is made of two constant states, the state vector W_L on the left side and the state vector W_R on the right side separated by a discontinuity located at $x = 0$.

$$W(x, 0) = \begin{cases} W_L & \text{if} \quad x < 0, \\ W_R & \text{if} \quad x > 0. \end{cases} \tag{2.51}$$

The eigenvalues associated to this System (2.50) are the simple eigenvalues $\lambda^{\pm} = u \pm \frac{a}{\rho}$ and the triple eigenvalue $\lambda^0 = u$. Note that a is a parameter to be determined. A particularity of this relaxation model is also that, even if ρ is an unknown of the system, it is though a parameter which value has to be determined arbitrarily. The initial given data of the Riemann problem deal with ρe and ρv, while q and u are determined through equilibrium states. Meanwhile, ρ_L and ρ_R are not known from the start and then are seen as new parameters. The parameters a, ρ_L and ρ_R will be useful to ensure the final scheme stability (see later in Section 2.4.3).

Concerning the standard algebra of System (2.50), first, let us consider the central wave of wavespeed $\lambda^0 = u$. An associated eigenvector is $r^0 = (1, 0, 0, 1, 1)^T$. We check the nature of the field with the operation $\nabla_W \lambda^0 \cdot r^0$. It turns out that it is equal

to zero which means that the field is linearly degenerate. Also, we determine the Riemann invariants associated with this field. They clearly come up as :

$$u \quad \text{and} \quad q,$$

which are thus constant across the contact wave with velocity $\lambda^0 = u$.

Next, considering the wave of wavespeed $\lambda^- = u - \frac{a}{\rho}$. An associated eigenvector is $r^- = (1, -a/\rho^2, a^2/\rho^2, q/\rho^2, 0)^T$. We have $\nabla_W \lambda^- \cdot r^- = 0$ so the field is also linearly degenerate. And the Riemann invariants associated with the λ^- field are

$$V,\ au + q,\ u - \frac{a}{\rho},\ \frac{q^2}{2} - a^2\varepsilon,$$

which are constant across the linearly degenerate wave.

As for the $\lambda^+ = u + \frac{a}{\rho}$ field, the associated eigenvector is determined as $r^+ = (1, a/\rho^2, a^2/\rho^2, q/\rho^2, 0)^T$. It also comes that $\nabla_W \lambda^+ \cdot r^+ = 0$ then the field is once again linearly degenerate. And the Riemann invariants associated with the λ^+ field are

$$V,\ au - q,\ u + \frac{a}{\rho},\ \frac{q^2}{2} - a^2\varepsilon.$$

The approximate solution of this Riemann problem containing three contact discontinuities is given by :

$$W(x,t) = \begin{cases} W_L & \text{if} \quad x/t < u_L - \frac{a}{\rho_L}, \\ W_L^\star & \text{if} \quad u_L - \frac{a}{\rho_L} < x/t < u^\star, \\ W_R^\star & \text{if} \quad u^\star < x/t < u_R + \frac{a}{\rho_R}, \\ W_R & \text{if} \quad x/t > u_R + \frac{a}{\rho_R}, \end{cases} \tag{2.52}$$

and is summed up in Figure 2.5. Note that this structure is valid when the waves remain ordered, that is to say when $u_L - \frac{a}{\rho_L} < u^\star < u_R + \frac{a}{\rho_R}$. Such an order of the waves will be imposed later on by the positivity of the intermediate densities.

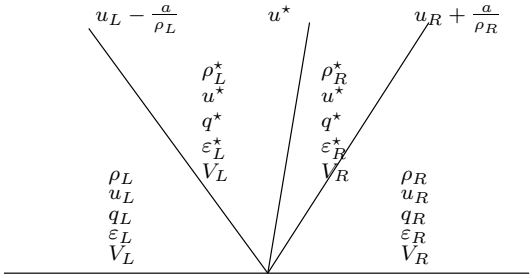

FIGURE 2.5 – Relaxation scheme - Riemann problem

The Riemann invariants allow us to write some relations to help closing the system. Indeed, across the contact wave λ^0, we have :

$$\begin{cases} u_L^\star = u_R^\star = u^\star, \\ q_L^\star = q_R^\star = q^\star. \end{cases} \tag{2.53}$$

Across the wave λ^- we have :

$$\begin{cases} V_L = V_L^\star, \\ au_L + q_L = au_L^\star + q_L^\star, \\ u_L - a/\rho_L = u_L^\star - a/\rho_L^\star, \\ q_L^2/2 - a^2\epsilon_L = q_L^{\star,2}/2 - a^2\epsilon_L^\star. \end{cases} \tag{2.54}$$

Finally, across the wave λ^+, the relations resulting from the knowledge of the Riemann invariants are :

$$\begin{cases} V_R = V_R^\star, \\ au_R - q_R = au_R^\star - q_R^\star, \\ u_R + a/\rho_R = u_R^\star + a/\rho_R^\star, \\ q_R^2/2 - a^2\epsilon_R = q_R^{\star,2}/2 - a^2\epsilon_R^\star. \end{cases} \tag{2.55}$$

The remaining variables to determine in each region are resumed in Figure 2.5.

The variables in the intermediate regions can now be expressed explicitly. Solving (2.53), (2.54) and (2.55), we have :

$$u^\star = \frac{u_L + u_R}{2} + \frac{q_L - q_R}{2a}, \tag{2.56}$$

$$q^\star = \frac{q_L + q_R}{2} + \frac{a}{2}(u_L - u_R), \tag{2.57}$$

$$\begin{cases} \varepsilon_L^\star = \varepsilon_L + \dfrac{q^{\star 2} - q_L^2}{2a^2}, \\ \varepsilon_R^\star = \varepsilon_R + \dfrac{q^{\star 2} - q_R^2}{2a^2}, \end{cases} \tag{2.58}$$

$$\begin{cases} \rho_L^\star = \dfrac{a\rho_L}{a + \rho_L(u^\star - u_L)}, \\ \rho_R^\star = \dfrac{a\rho_R}{a + \rho_R(u_R - u^\star)}. \end{cases} \tag{2.59}$$

Meanwhile, some parameters such as ρ_L, ρ_R and a have to be chosen properly for the scheme to verify the required physical properties as the energy positivity and the flux limitation, ρ_L, ρ_R and a being positive parameters. The relations outlined in the following subsection enable us to set the position of the Riemann problem waves and ensure the good ordering of the waves.

2.4.3 Model properties

From the construction of the relaxation model (2.48), we have at our disposal some parameters which we can fiddle with in order to ensure the preservation of the important mathematical properties. Particularly the position of the Riemann solver waves depend on the ρ_L, ρ_R and a parameters (see Figure 2.5), and is determined with the objective to have the radiative energy positivity and the radiative flux limitation verified.

In all the upcoming, the left and right variables are assumed to respect the needed properties, namely the radiative energy positivity and the radiative flux limitation, and we make sure that the variables in the star region observe them as well. Then the approximate Riemann solution of the relaxation model is included in the solutions admissible space Ω defined by (1.31).

Density positivity. The parameter ρ must remain positive. According to the relations (2.59) concerning $\rho^\star_{L,R}$ the following lemma can be written.

Proposition 3. *Assume W_L and W_R in Ω. Let us set :*

$$\Delta_{\rho,L} = \rho_L^2(\frac{u_R - u_L}{2})^2 - 2\rho_L(q_L - q_R)$$

and

$$\Delta_{\rho,R} = \rho_R^2(\frac{u_R - u_L}{2})^2 - 2\rho_R(q_R - q_L).$$

There exist a real number a big enough such that :

$$\text{if} \quad \Delta_{\rho,L} \geq 0, \quad a > max\left(-\rho_L\frac{u_R - u_L}{4} \pm \frac{\sqrt{\Delta_{\rho,L}}}{2}, 0\right), \tag{2.60}$$

$$\text{else if} \quad \Delta_{\rho,L} < 0, \quad a > 0,$$

and

$$\text{if} \quad \Delta_{\rho,R} \geq 0, \quad a > max\left(-\rho_R\frac{u_R - u_L}{4} \pm \frac{\sqrt{\Delta_{\rho,R}}}{2}, 0\right), \tag{2.61}$$

$$\text{else if} \quad \Delta_{\rho,R} < 0, \quad a > 0.$$

Then $\rho^\star_L > 0$ and $\rho^\star_R > 0$. As a consequence, the waves are ordered, and we have :

$$u_L - \frac{a}{\rho_L} < u^\star < u_R + \frac{a}{\rho_R}. \tag{2.62}$$

Proof. We first consider equation (2.59) where a and ρ_L are positive parameters. Then, for $\rho^\star_L$ to be positive, the inequality :

$$a + \rho_L(u^\star - u_L) > 0,$$

has to be verified. Including (2.56), this statement appears to be equivalent to :

$$a^2 + \rho_L\frac{u_R - u_L}{2}a + \rho_L\frac{q_L - q_R}{2} > 0. \tag{2.63}$$

If the discriminant of (2.63) is negative, then (2.63) is always verified and $\rho^\star_L > 0$. And if the discriminant of (2.63) is positive, then a must verify (2.60) for $\rho^\star_L$ to be positive.

Next, let us consider equation (2.59) where a and ρ_R are positive parameters. Then, for $\rho_R^\star$ to be positive, the inequality :

$$a + \rho_L(u_R - u^\star) > 0,$$

has to be verified. Including (2.56), this statement appears to be equivalent to :

$$a^2 + \rho_R \frac{u_R - u_L}{2} a + \rho_L \frac{q_R - q_L}{2} > 0. \tag{2.64}$$

If the discriminant of (2.64) is negative, then (2.64) is always verified and $\rho_R^\star > 0$. And if the discriminant of (2.64) is positive, then a must verify (2.61) for $\rho_R^\star$ to be positive.

Concerning the wave order, from the positiveness of $\rho_L^\star$ and $\rho_R^\star$, we immediately have :

$$u^\star - \frac{a}{\rho_L^\star} < u^\star < u^\star + \frac{a}{\rho_R^\star}.$$

Then (2.62) easily comes from the continuity of the Riemann invariants. □

Radiative energy positivity. We now make sure the radiative energy remains positive, that is to say that $E_{L,R}^\star > 0$. From (2.36), let us write the following equalities :

$$E_{L,R}^\star = (\rho e)_{L,R}^\star,$$

which also writes :

$$E_{L,R}^\star = \rho_{L,R}^\star \varepsilon_{L,R}^\star + \rho_{L,R}^\star \frac{u^{\star,2}}{2}.$$

Knowing from Proposition 3 that $\rho_{L,R}^\star > 0$, we then at most need to have $\varepsilon_{L,R}^\star > 0$ for the positivity of the radiative energy to be preserved.

We use the parameter a and determine its value in such a way that $\varepsilon_{L,R}^\star$ is positive and therefore ensure that the radiative energy is positive.

Proposition 4. *Assume W_L and W_R in Ω. Let us set :*

$$\Delta_{E,L} = \left(\frac{(q_L + q_R)(u_L - u_R)}{4}\right)^2 - 2\left(\varepsilon_L + \frac{(u_L - u_R)^2}{8}\right)\left(\left(\frac{q_L + q_R}{2}\right)^2 - q_L^2\right)$$

and

$$\Delta_{E,R} = \left(\frac{(q_L + q_R)(u_L - u_R)}{4}\right)^2 - 2\left(\varepsilon_R + \frac{(u_L - u_R)^2}{8}\right)\left(\left(\frac{q_L + q_R}{2}\right)^2 - q_R^2\right).$$

There exist a real number a big enough such that :

$$\text{if} \quad \Delta_{E,L} \geq 0, \quad a > max\left(\frac{-\frac{(q_L+q_R)(u_L-u_R)}{4} \pm \sqrt{\Delta_{E,L}}}{2\left(\varepsilon_L + \frac{(u_L-u_R)^2}{8}\right)}, 0 \right), \tag{2.65}$$

$$\text{else if} \quad \Delta_{E,L} < 0, \quad a > 0,$$

and

$$\text{if} \quad \Delta_{E,R} \geq 0, \quad a > max\left(\frac{-\frac{(q_L+q_R)(u_L-u_R)}{4} \pm \sqrt{\Delta_{E,R}}}{2\left(\varepsilon_R + \frac{(u_L-u_R)^2}{8}\right)}, 0 \right), \tag{2.66}$$

$$\text{else if} \quad \Delta_{E,R} < 0, \quad a > 0.$$

Then $\varepsilon_L^\star > 0$ *and* $\varepsilon_R^\star > 0$.

Proof. Let us start from the expression for $\varepsilon_L^\star$ in (2.58). We are looking to prove that :

$$\varepsilon_L + \frac{q^{\star,2} - q_L^2}{2a^2} > 0,$$

which, using (2.57), is equivalent with proving :

$$\varepsilon_L + \frac{1}{2a^2}\left[\left(\frac{q_L+q_R}{2} + \frac{a}{2}(u_L-u_R)\right)^2 - q_L^2\right] > 0, \tag{2.67}$$

And then, developing (2.67), it leaves :

$$\left(\varepsilon_L + \frac{(u_L-u_R)^2}{8}\right)a^2 + \frac{(q_L+q_R)(u_L-u_R)}{4}a + \frac{1}{2}\left(\left(\frac{q_L+q_R}{2}\right)^2 - q_L^2\right) > 0 \tag{2.68}$$

Knowing that $\varepsilon_L + \frac{(u_L-u_R)^2}{8} > 0$, if the discriminant of (2.68) is negative, then (2.68) is always verified and $\varepsilon_L^\star > 0$. And if the discriminant of (2.68) is positive, then a must verify (2.65) for $\varepsilon_L^\star$ to be positive.

Next, we consider the expression for $\varepsilon_R^\star$ in (2.58). We want to prove that :

$$\varepsilon_R + \frac{q^{\star,2} - q_R^2}{2a^2} > 0,$$

which, using (2.57), is equivalent with proving :

$$\varepsilon_R + \frac{1}{2a^2}\left[\left(\frac{q_L+q_R}{2} + \frac{a}{2}(u_L-u_R)\right)^2 - q_R^2\right] > 0, \tag{2.69}$$

And then, developing (2.69), it leaves :

$$\left(\varepsilon_R + \frac{(u_L - u_R)^2}{8}\right) a^2 + \frac{(q_L + q_R)(u_L - u_R)}{4} a + \frac{1}{2}\left(\left(\frac{q_L + q_R}{2}\right)^2 - q_R^2\right) > 0 \quad (2.70)$$

Knowing that $\varepsilon_R + \frac{(u_L - u_R)^2}{8} > 0$, if the discriminant of (2.70) is negative, then (2.70) is always verified and $\varepsilon_R^\star > 0$. And if the discriminant of (2.70) is positive, then a must verify (2.66) for $\varepsilon_R^\star$ to be positive. □

Flux limitation. The flux limitation is also enforced through several additional constraints. From (2.36), the intermediate non dimensional fluxes write :

$$\frac{F_{x,L}^\star}{cE_L^\star} = \frac{F_{x,L}/\rho_L + c^2\left[(u_R - u_L)/2 + (q_L - q_R)/2a\right]}{c\left[E_L/\rho_L + (q_R^2 - q_L^2)/4a^2 + (q_L u_L - q_R u_R)/2a + (u_R^2 - u_L^2)/4\right]}, \quad (2.71)$$

$$\frac{F_{x,R}^\star}{cE_R^\star} = \frac{F_{x,R}/\rho_R + c^2\left[(u_L - u_R)/2 + (q_L - q_R)/2a\right]}{c\left[E_R/\rho_R + (q_L^2 - q_R^2)/4a^2 + (q_L u_L - q_R u_R)/2a + (u_L^2 - u_R^2)/4\right]}. \quad (2.72)$$

The flux limitation imposed to the intermediate states reads : $-1 \leq F_{x,L}^\star/cE_L^\star \leq 1$ and $-1 \leq F_{x,R}^\star/cE_R^\star \leq 1$. We first enforce the denominator of (2.71) and (2.72) to be positive imposing constraints on ρ_L, ρ_R and a.

Proposition 5. *Let us set :*

$$D_L = (q_L u_L - q_R u_R)^2 - (4E_L/\rho_L + u_R^2 - u_L^2)(q_R^2 - q_L^2)$$

and

$$D_R = (q_L u_L - q_R u_R)^2 - (4E_R/\rho_R + u_L^2 - u_R^2)(q_L^2 - q_R^2).$$

There exist $\rho_L > 0$ small enough and the parameter a big enough such that :

$$\text{if} \quad D_L \geq 0, \quad a > max\left(\frac{-(q_L u_L - q_R u_R) \pm \sqrt{D_L}}{4E_L/\rho_L + u_R^2 - u_L^2}, 0\right), \quad (2.73)$$

$$\text{else if} \quad D_L < 0, \quad a > 0,$$

and

$$\frac{1}{\rho_L} \geq \frac{u_L^2 - u_R^2}{4E_L}. \quad (2.74)$$

Then :

$$c\left[\frac{E_L}{\rho_L} + \frac{q_R^2 - q_L^2}{4a^2} + \frac{q_L u_L - q_R u_R}{2a} + \frac{u_R^2 - u_L^2}{4}\right] > 0. \quad (2.75)$$

In addition, there exist $\rho_R > 0$ small enough and the parameter a big enough such that :

$$\text{if} \quad D_R \geq 0, \quad a > max\left(\frac{-(q_L u_L - q_R u_R) \pm \sqrt{D_R}}{4E_R/\rho_R + u_L^2 - u_R^2}, 0\right), \tag{2.76}$$

$$\text{else if} \quad D_R < 0, \quad a > 0,$$

and

$$\frac{1}{\rho_R} \geq \frac{u_R^2 - u_L^2}{4E_R}. \tag{2.77}$$

Then :

$$c\left[\frac{E_R}{\rho_R} + \frac{q_L^2 - q_R^2}{4a^2} + \frac{q_L u_L - q_R u_R}{2a} + \frac{u_L^2 - u_R^2}{4}\right] > 0. \tag{2.78}$$

Proof. Assume $a > 0$. We multiply (2.75) by a^2 and we obtain :

$$\left(\frac{E_L}{\rho_L} + \frac{u_R^2 - u_L^2}{4}\right) a^2 + \frac{q_L u_L - q_R u_R}{2} a + \frac{q_R^2 - q_L^2}{4} > 0. \tag{2.79}$$

We then impose $\frac{E_L}{\rho_L} + \frac{u_R^2 - u_L^2}{4} > 0$ with (2.74). If the discriminant D_L is negative, (2.79) is thus verified. And if D_L is positive, with (2.73), (2.79) is true.

Next, multiplying (2.78) by a^2, we obtain :

$$\left(\frac{E_R}{\rho_R} + \frac{u_L^2 - u_R^2}{4}\right) a^2 + \frac{q_L u_L - q_R u_R}{2} a + \frac{q_L^2 - q_R r^2}{4} > 0.$$

We then impose $\frac{E_R}{\rho_R} + \frac{u_L^2 - u_R^2}{4} > 0$ with (2.77). If the discriminant D_R is negative, (2.80) is thus verified. And if D_R is positive, with (2.76), (2.80) is true. □

Assuming the above constraints on ρ_L, ρ_R and a, it is now just a matter of matching with the following inequalities :

• $F_{x,L}^\star / cE_L^\star \leq 1$ is ensured thanks to :

$$\begin{aligned} a^2 \left[\frac{4}{\rho_L}(F_{x,L} - cE_L) + 2c^2(u_R - u_L) - c(u_R^2 - u_L^2)\right] \\ + a\left[2c^2(q_L - q_R) - 2c(q_L u_L - q_R u_R)\right] - c(q_R^2 - q_L^2) \leq 0. \end{aligned} \tag{2.80}$$

• $F_{x,L}^\star / cE_L^\star \geq -1$ is verified if :

$$\begin{aligned} a^2 \left[\frac{4}{\rho_L}(F_{x,L} + cE_L) + 2c^2(u_R - u_L) + c(u_R^2 - u_L^2)\right] \\ + a\left[2c^2(q_L - q_R) + 2c(q_L u_L - q_R u_R)\right] + c(q_R^2 - q_L^2) \geq 0. \end{aligned} \tag{2.81}$$

• $F^\star_{x,R}/cE^\star_R \leq 1$ is verified if :

$$\begin{aligned} a^2 \left[\frac{4}{\rho_R}(F_{x,R} - cE_R) + 2c^2(u_L - u_R) - c(u_L^2 - u_R^2) \right] \\ +a \left[2c^2(q_L - q_R) - 2c(q_L u_L - q_R u_R) \right] - c(q_L^2 - q_R^2) \leq 0. \end{aligned} \tag{2.82}$$

• And $F^\star_{x,R}/cE^\star_R \geq -1$ is verified if :

$$\begin{aligned} a^2 \left[\frac{4}{\rho_R}(F_{x,R} + cE_R) + 2c^2(u_L - u_R) + c(u_L^2 - u_R^2) \right] \\ +a \left[2c^2(q_L - q_R) + 2c(q_L u_L - q_R u_R) \right] + c(q_L^2 - q_R^2) \geq 0. \end{aligned} \tag{2.83}$$

The next propositions ensure the flux limitations, the proofs are not detailed here as the formulas are too extensive, even if they do not hold particular difficulties.

Proposition 6. *There exist $\rho_L > 0$ small enough and a big enough defined as follows :*

$$\text{if} \quad d_{L,1} \geq 0, \quad a > max \left(\frac{-(2c^2(q_L - q_R) - 2c(q_L u_L - q_R u_R)) \pm \sqrt{d_{L,1}}}{2\left(\frac{4}{\rho_L}(F_{x,L} - cE_L) + 2c^2(u_R - u_L) - c(u_R^2 - u_L^2)\right)}, 0 \right) \tag{2.84}$$

$$\text{else if} \quad d_{L,1} < 0, \quad a > 0,$$

where

$$\begin{aligned} d_{L,1} = &\left(2c^2(q_L - q_R) - 2c(q_L u_L - q_R u_R)\right)^2 \\ &-4\left(\frac{4}{\rho_L}(F_{x,L} - cE_L) + 2c^2(u_R - u_L) - c(u_R^2 - u_L^2)\right)\left(-c(q_R^2 - q_L^2)\right). \end{aligned}$$

And also :

$$\text{if} \quad d_{L,2} \geq 0, \quad a > max \left(\frac{-(2c^2(q_L - q_R) - 2c(q_L u_L - q_R u_R)) \pm \sqrt{d_{L,2}}}{2\left(\frac{4}{\rho_L}(F_{x,L} + cE_L) + 2c^2(u_R - u_L) - c(u_R^2 - u_L^2)\right)}, 0 \right) \tag{2.85}$$

$$\text{else if} \quad d_{L,2} < 0, \quad a > 0,$$

where

$$\begin{aligned} d_{L,2} = &\left(2c^2(q_L - q_R) - 2c(q_L u_L - q_R u_R)\right)^2 \\ &-4\left(\frac{4}{\rho_L}(F_{x,L} + cE_L) + 2c^2(u_R - u_L) - c(u_R^2 - u_L^2)\right)\left(-c(q_R^2 - q_L^2)\right). \end{aligned}$$

Meanwhile, the parameter ρ_L is determined with :

$$\frac{1}{\rho_L} \geq max \left(\frac{c(u_R^2 - u_L^2) - 2c^2(u_R - u_L)}{4(F_{x,L} - cE_L)}, \frac{-c(u_R^2 - u_L^2) - 2c^2(u_R - u_L)}{4(F_{x,L} + cE_L)}, 0 \right). \tag{2.86}$$

Then $-1 \leq F^{\star}_{x,L}/cE^{\star}_{L} \leq 1$.

In addition, there exist $\rho_R > 0$ *small enough and a big enough defined as follows :*

$$\textit{if} \quad d_{R,1} < 0, \quad a > max\left(\frac{-(2c^2(q_L-q_R)-2c(q_Lu_L-q_Ru_R)) \pm \sqrt{d_{R,1}}}{2\left(\frac{4}{\rho_R}(F_{x,R}-cE_R)+2c^2(u_L-u_R)-c(u_L^2-u_R^2)\right)}, 0\right) \quad (2.87)$$

$$\textit{else if} \quad d_{R,1} < 0, \quad a > 0,$$

where

$$d_{R,1} = \left(2c^2(q_L-q_R)-2c(q_Lu_L-q_Ru_R)\right)^2 - 4\left(\frac{4}{\rho_R}(F_{x,R}-cE_R)+2c^2(u_L-u_R)-c(u_L^2-u_R^2)\right)\left(-c(q_L^2-q_R^2)\right).$$

And also :

$$\textit{if} \quad d_{R,2} < 0, \quad a > max\left(\frac{-(2c^2(q_L-q_R)-2c(q_Lu_L-q_Ru_R)) \pm \sqrt{d_{R,2}}}{2\left(\frac{4}{\rho_R}(F_{x,R}+cE_R)+2c^2(u_L-u_R)-c(u_L^2-u_R^2)\right)}, 0\right) \quad (2.88)$$

$$\textit{else if} \quad d_{R,2} < 0, \quad a > 0,$$

$$d_{R,2} = \left(2c^2(q_L-q_R)-2c(q_Lu_L-q_Ru_R)\right)^2 - 4\left(\frac{4}{\rho_R}(F_{x,R}+cE_R)+2c^2(u_L-u_R)-c(u_L^2-u_R^2)\right)\left(-c(q_L^2-q_R^2)\right).$$

Meanwhile, the parameter ρ_R *is determined with :*

$$\frac{1}{\rho_R} \geq max\left(\frac{c(u_L^2-u_R^2)-2c^2(u_L-u_R)}{4(F_{x,R}-cE_R)}, \frac{-c(u_L^2-u_R^2)-2c^2(u_L-u_R)}{4(F_{x,R}+cE_R)}, 0\right). \quad (2.89)$$

Then $-1 \leq F^{\star}_{x,R}/cE^{\star}_{R} \leq 1$.

Following all the above properties, several constraints are imposed on the parameters a and $\rho_{L,R}$ for the radiative energy positivity and radiative flux limitation to be preserved. To sum it up, a has to simultaneously verify (2.65), (2.66), (2.73), (2.76), (2.84), (2.85), (2.87) and (2.88). And in the mean time ρ_L and ρ_R verify (2.60), (2.61), (2.74), (2.77), (2.86) and (2.89). Note that these constraints tend to widen the numerical cone (see Figure 2.5) and may cause excessive numerical viscosity.

2.4.4 Relaxation scheme procedure

On the basis of the relaxation model (2.48), we describe the numerical procedure that is commonly used in the framework of relaxation schemes, using the notations introduced in Section 2.2 and considering a structured mesh in space and time defined by the cells $I_i = (x_{i-\frac{1}{2}}, x_{i+\frac{1}{2}})$ and the time intervals $[t^n, t^{n+1})$ (see Figure 2.1).

At the time t^n, we know the state vector $U^n = (E^n, F^n)$, and we aim to calculate the state vector U^{n+1} at the time t^{n+1}. With this purpose,, we use a relaxation procedure based on (2.47) and composed of two steps.

In the first step, working with the relaxation model (2.47) in its conservative form, we aim to evolve the solution U^n to $U^{n+1,-}$. We define the conservative relaxation state vector :

$$w_i^n = (\rho_i^n, (\rho u)_i^n, (\rho v)_i^n, (\rho e)_i^n, (\rho q)_i^n),$$

and write a Godunov type solver for this model. It is summed up as :

$$\partial_t w + \partial_x G(w) = 0, \tag{2.90}$$

where

$$G(w) = (\rho u, \rho u^2 + q, \rho uv, (\rho e + q)u, \rho uq + a^2 u). \tag{2.91}$$

The Riemann problem solution for this equation is obtained through (2.56), (2.57), (2.58), and (2.59).

The updated state vector $w_i^{n+1,-}$ is then determined with a Godunov type scheme through :

$$w_i^{n+1,-} = w_i^n - \frac{\Delta t}{\Delta x}\left(G(w^h(x_{i+\frac{1}{2}}, t^{n+1,-}, w_i^n, w_{i+1}^n)) - G(w^h(x_{i-\frac{1}{2}}, t^{n+1,-}, w_{i-1}^n, w_i^n))\right) \tag{2.92}$$

where $w^h(x_{i+\frac{1}{2}}, t^{n+1,-}, w_i^n, w_{i+1}^n)$ is the Riemann problem solution at the interface, where w_i^n and w_{i+1}^n are known, and under the CFL like condition :

$$\frac{\Delta t}{\Delta x}\max_i\left(\left|u_i^n + \frac{a_{i-\frac{1}{2}}}{\rho_R^{i-\frac{1}{2}}}\right|, \left|u_i^n - \frac{a_{i+\frac{1}{2}}}{\rho_L^{i+\frac{1}{2}}}\right|\right) \leq \frac{1}{2}. \tag{2.93}$$

Next, the second step is dedicated to the actual relaxation enforcing the updated state to be at the equilibrium. To access such an issue, the system solved is the following :

$$\partial_t w = \frac{\rho}{\delta}(0, c\beta_x - u, 0, 0, q - \Pi), \tag{2.94}$$

with $w_i^{n+1,-}$ as initial data. It also writes as :

$$\begin{cases} \partial_t \rho = 0, \\ \partial_t \rho u = \dfrac{\rho}{\delta}(c\beta_x - u), \\ \partial_t \rho v = 0, \\ \partial_t \rho e = 0, \\ \partial_t \rho q = \dfrac{\rho}{\delta}(q - \Pi). \end{cases} \tag{2.95}$$

Whenever δ tends to zero, as $u_i^{n+1} = (c\beta_x)_i^{n+1}$ and $q_i^{n+1} = \Pi_i^{n+1}$, the updated state vector at the time t^{n+1} is given by w_i^{n+1} and the solution of (2.94) is given by :

$$\left\{ \begin{array}{l} \rho_i^{n+1} = \rho_i^{n+1,-}, \\ (\rho e)_i^{n+1} = (\rho e)_i^{n+1,-}, \\ (\rho v)_i^{n+1} = (\rho v)_i^{n+1,-}, \end{array} \right. \tag{2.96}$$

And thus, having $E_i^{n+1} = (\rho e)_i^{n+1}$ and $F_i^{n+1} = (\rho v)_i^{n+1}$, the updated state vector $U_i^{n+1} = (E_i^{n+1}, F_i^{n+1})$ is deduced. The scheme can then be written as a usual approximate Riemann solver :

$$\begin{array}{l} E_i^{n+1} = E_i^n - \dfrac{\Delta t}{\Delta x}(\mathcal{F}^E_{i+\frac{1}{2}} - \mathcal{F}^E_{i-\frac{1}{2}}), \\ F_i^{n+1} = F_i^n - \dfrac{\Delta t}{\Delta x}(\mathcal{F}^F_{i+\frac{1}{2}} - \mathcal{F}^F_{i-\frac{1}{2}}), \end{array} \tag{2.97}$$

where

$$\mathcal{F}^E_{i+\frac{1}{2}} = G^{\rho e}\left(w^h(x_{i+\frac{1}{2}}, t^{n+1}, w_i^n, w_{i+1}^n)\right)$$

and

$$\mathcal{F}^F_{i+\frac{1}{2}} = G^{\rho v}\left(w^h(x_{i+\frac{1}{2}}, t^{n+1}, w_i^n, w_{i+1}^n)\right)$$

are respectively determined through the components of the vector defined by (2.91) associated to the ρe and ρv components of the state vector of conservative variables w.

Note that, in order to reduce the numerical viscosity, the parameters $a_{i+\frac{1}{2}}$ and $\rho_{L,R}^{i+\frac{1}{2}}$ are locally determined at each interface according to (2.65), (2.66), (2.73), (2.76), (2.84), (2.85), (2.87) and (2.88) concerning a, and according to ρ_L and ρ_R verify (2.60), (2.61), (2.74), (2.77), (2.86) and (2.89) concerning $\rho_{L,R}$.

This procedure is quite simple to code and some results are presented against the HLLC solution in Section 2.6. We finally set the scheme robustness.

Theorem 7. *Consider an admissible sequence $(U_i^n)_{i\in\mathbb{Z}}$ in $\mathcal{A}$ defined by (1.31). Define the updated sequence $(U_i^{n+1})_{i\in\mathbb{Z}}$ by the scheme (2.97) under the CFL like condition (2.93) and with a and $\rho_{L,R}$ determined according to (2.65), (2.66), (2.73), (2.76), (2.84), (2.85), (2.87), (2.88) and (2.60), (2.61), (2.74), (2.77), (2.86), (2.89). Then we have U_i^{n+1} is in $\mathcal{A}$ for all $i \in \mathbb{Z}$.*

Proof. Consider $(U_i^n)_{i\in\mathbb{Z}}$ in $\mathcal{A}$ and $(U_i^{n+1})_{i\in\mathbb{Z}}$ defined by (2.97) under the CFL like condition (2.93). U_i^{n+1} results from the following integration in the cell $(x_{i-\frac{1}{2}}, x_{i+\frac{1}{2}})$, $i \in \mathbb{Z}$:

$$U_i^{n+1} = \frac{1}{\Delta x}\int_{x_{i-\frac{1}{2}}}^{x_{i+\frac{1}{2}}} U^h(x, t^{n+1})dx, \tag{2.98}$$

where U^h is the juxtaposition of the non-interacting approximate Riemann problems. From the propositions 4 and 6, we have that each of the approximate states satisfies

the energy positivity property and the flux limitation property. Therefore, focusing first on the energy positivity, we can write :

$$E^h(x,t^{n+1}) > 0 \quad \text{for all} \quad x \in (x_{i-\frac{1}{2}}, x_{i+\frac{1}{2}}) \quad \text{and} \quad i \in \mathbb{Z}.$$

So it comes :

$$E_i^{n+1} = \frac{1}{\Delta x} \int_{x_{i-\frac{1}{2}}}^{x_{i+\frac{1}{2}}} E^h(x,t^{n+1}) dx \; > \; 0, \tag{2.99}$$

and then, $E_i^{n+1} \; > \; 0$ for all $i \in \mathbb{Z}$.

As for the flux limitation property, we have :

$$F_x^h(x,t^{n+1}) - cE^h(x,t^{n+1}) < 0 \quad \text{for all} \quad x \in (x_{i-\frac{1}{2}}, x_{i+\frac{1}{2}}) \quad \text{and} \quad i \in \mathbb{Z},$$

and

$$F_x^h(x,t^{n+1}) + cE^h(x,t^{n+1}) > 0 \quad \text{for all} \quad x \in (x_{i-\frac{1}{2}}, x_{i+\frac{1}{2}}) \quad \text{and} \quad i \in \mathbb{Z}.$$

So it comes :

$$F_{x,i}^{n+1} - cE_i^{n+1} = \frac{1}{\Delta x} \int_{x_{i-\frac{1}{2}}}^{x_{i+\frac{1}{2}}} (F_x^h(x,t^{n+1}) - cE^h(x,t^{n+1})) dx \; < \; 0, \tag{2.100}$$

then $F_{x,i}^{n+1} - cE_i^{n+1} < 0$ for all $i \in \mathbb{Z}$. And :

$$F_{x,i}^{n+1} + cE_i^{n+1} = \frac{1}{\Delta x} \int_{x_{i-\frac{1}{2}}}^{x_{i+\frac{1}{2}}} (F_x^h(x,t^{n+1}) - cE^h(x,t^{n+1})) dx \; > \; 0, \tag{2.101}$$

then $F_{x,i}^{n+1} + cE_i^{n+1} > 0$ for all $i \in \mathbb{Z}$. Therefore U_i^{n+1} is in $\mathcal{A}$ for all $i \in \mathbb{Z}$. □

2.5 The HLLC scheme

The HLLC scheme developed in this section is based on the classical HLL method (see [27]). The HLL scheme is known to be stable but rather viscous. The numerical viscosity comes from the presence of a single intermediate state in the constructed Riemann problem. This property, and the not satisfying numerical results we obtain, raise the need to have at our disposal a more accurate tool. The present HLLC method comes from an improved HLL method designed to exactly capture the stationary contact wave which influence is outlined in two dimensional configurations. It then allows us to integrate the solution over two intermediate states as for the relaxation model but aiming to profit from a more accurate approximation of the Riemann solution.

2.5.1 Linearisations

Let us start again with the 1D simplified system (2.33) with no source terms and only x-directed contributions. For the sake of simplicity, let us set the outer wavespeeds as b_L and b_R verifying $b_L < 0 < b_R$. We also set :

$$U = \begin{pmatrix} E \\ F_x \end{pmatrix} \quad \text{and} \quad \mathcal{F} = \begin{pmatrix} F_x \\ c^2 P_{xx} \end{pmatrix}.$$

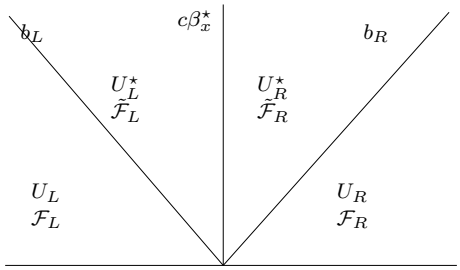

FIGURE 2.6 – HLLC scheme - Riemann problem

In order to introduce linearisations inspired by the above relaxation method and such as (2.39), and given the radiative pressure written in the form

$$\mathbf{P} = \left(\frac{1-\chi(f)}{2}\mathbf{I} + \frac{3\chi(f)-1}{2}\frac{F_x^2}{F^2} \right) E,$$

we choose to introduce the variables β_x and Π as :

$$\Pi = \frac{1-\chi(f)}{2}E \quad \text{and} \quad \beta_x = \frac{3\chi(f)-1}{2}\frac{F_x}{F^2}cE. \tag{2.102}$$

Therefore simple relations, similar to (2.39), that will reveal themselves quite handy in the following developments can be written. They are :

$$\begin{cases} F_x = c\beta_x(E+\Pi), \\ P_{xx} = \dfrac{\beta_x F_x}{c} + \Pi. \end{cases} \tag{2.103}$$

These relations turn out to be useful for the determination of the flux functions and intermediate states of the given approximate Riemann problem. They actually constitute the fundamental elements of the present HLLC method for radiative transfer. From these, we have been able to derive an accurate and stable scheme for the resolution of the radiative transfer equation.

We propose an HLLC type solver considering two intermediate states, separated by a wave of which we note the speed as $c\beta_x^\star$. The approximate Riemann solution thus writes :

$$U(x/t) = \begin{cases} U_L & \text{if } x/t < b_L, \\ U_L^\star & \text{if } b_L < x/t < c\beta_x^\star, \\ U_R^\star & \text{if } c\beta_x^\star < x/t < b_R, \\ U_R & \text{if } x/t > b_R, \end{cases} \tag{2.104}$$

where the corresponding approximate flux is :

$$\mathcal{H}(x/t) = \begin{cases} \mathcal{F}(U_L) & \text{if } x/t < b_L, \\ \tilde{\mathcal{F}}_L & \text{if } b_L < x/t < c\beta_x^\star, \\ \tilde{\mathcal{F}}_R & \text{if } c\beta_x^\star < x/t < b_R, \\ \mathcal{F}(U_R) & \text{if } x/t > b_R. \end{cases} \tag{2.105}$$

Let us remind that as in this approximate Riemann solver, we have $\tilde{\mathcal{F}}_L \neq \mathcal{F}(U_L^\star)$ and $\tilde{\mathcal{F}}_R \neq \mathcal{F}(U_R^\star)$.

Based on (2.103), we propose the following linearisations :

$$\begin{cases} F_{x,L}^\star = c\beta_{x,L}^\star(E_L^\star + \Pi_L^\star), \\ \tilde{P}_{xx,L} = \dfrac{\beta_{x,L}^\star \tilde{F}_{x,L}}{c} + \Pi_L^\star. \end{cases} \quad \begin{cases} F_{x,R}^\star = c\beta_{x,R}^\star(E_R^\star + \Pi_R^\star), \\ \tilde{P}_{xx,R} = \dfrac{\beta_{x,R}^\star \tilde{F}_{x,R}}{c} + \Pi_R^\star, \end{cases} \tag{2.106}$$

where $\beta_{x,L,R}^\star$ and $\Pi_{L,R}^\star$ are relevant linearisations of β_x and Π defined by Equation (2.102). In addition, $\beta_{x,L,R}^\star$ and $\Pi_{L,R}^\star$ being continuous across the middle wave separating the two intermediate states, we have $\beta_{x,L}^\star = \beta_{x,R}^\star = \beta_x^\star$ and $\Pi_L^\star = \Pi_R^\star = \Pi^\star$. Let us also point out that $F_{x,L}^\star = \tilde{F}_{x,L}$ and $F_{x,R}^\star = \tilde{F}_{x,R}$.

We can now focus on the determination of the $U_{L,R}^\star$ and $\tilde{\mathcal{F}}_{L,R}$ variables.

2.5.2 Flux functions and intermediate states

The same way as for the HLL scheme, the approximate Rankine-Hugoniot relations are used to evaluate $E_{L,R}^\star$, $F_{x,L,R}^\star$, $\tilde{F}_{x,L,R}$ and $\tilde{P}_{xx,L,R}$. We write the Rankine-Hugoniot relations across the waves of speeds b_L and b_R :

$$\begin{cases} \tilde{F}_{x,L} - F_{x,L} = b_L(E_L^\star - E_L), \\ \tilde{F}_{x,R} - F_{x,R} = b_R(E_R^\star - E_R), \end{cases} \tag{2.107}$$

$$\begin{cases} c^2(\tilde{P}_{xx,L} - P_{xx,L}) = b_L(F_{x,L}^\star - F_{x,L}), \\ c^2(\tilde{P}_{xx,R} - P_{xx,R}) = b_R(F_{x,R}^\star - F_{x,R}), \end{cases} \tag{2.108}$$

In the process of the Riemann problem resolution, our first objective is to determine $U_{L,R}^\star$ and $\tilde{\mathcal{F}}_{L,R}$. Let us note the appearence of some HLL typical relations for the radiative transfer resolution, as they are also visible and used in [6]. Let us remind here the HLL flux functions and intermediate states in the star region and the corresponding flux functions :

$$\begin{aligned} E_{HLL}^\star &= \frac{b_R E_R - b_L E_L}{b_R - b_L} - \frac{1}{b_R - b_L}(F_{x,R} - F_{x,L}), \\ F_{x,HLL}^\star &= \frac{b_R F_{x,R} - b_L F_{x,L}}{b_R - b_L} - \frac{c^2}{b_R - b_L}(P_{xx,R} - P_{xx,L}), \end{aligned} \tag{2.109}$$

$$\begin{aligned} \tilde{F}_{x,HLL} &= \frac{b_R F_{x,L} - b_L F_{x,R}}{b_R - b_L} + \frac{b_R b_L}{b_R - b_L}(E_R - E_L), \\ \tilde{P}_{xx,HLL} &= \frac{b_R P_{xx,L} - b_L P_{xx,R}}{b_R - b_L} + \frac{b_R b_L}{c^2(b_R - b_L)}(F_{x,R} - F_{x,L}). \end{aligned} \tag{2.110}$$

Making use of the linearisations (2.106), it clearly comes the expressions for the radiative energy in the star region, they write as follows :

$$\begin{cases} E_L^\star = \dfrac{F_{x,L} - b_L E_L - c\beta_x^\star \Pi^\star}{c\beta_x^\star - b_L}, \\ E_R^\star = \dfrac{F_{x,R} - b_R E_R - c\beta_x^\star \Pi^\star}{c\beta_x^\star - b_R}. \end{cases} \tag{2.111}$$

And from (2.106), knowing $E_{L,R}^\star$, it is easy to determine $F_{x,L,R}^\star$ with :

$$\begin{cases} F_{x,L}^\star = c\beta_x^\star (E_L^\star + \Pi^\star), \\ F_{x,R}^\star = c\beta_x^\star (E_R^\star + \Pi^\star). \end{cases} \tag{2.112}$$

The remaining variables to explicitly express are $\beta_x^\star$ and $\Pi^\star$. We show in the following that $\beta_x^\star$ comes out as the solution of a quadratic equation involving the HLL variables, and $\Pi^\star$ is linearly related to the same HLL variables. The next two propositions 8 and 9 allow us to establish this quadratic equation.

Proposition 8. *The states $\beta_x^\star$ and $\Pi^\star$ verify the relation*

$$F_{x,HLL}^\star = c\beta_x^\star (\Pi^\star + E_{HLL}^\star), \tag{2.113}$$

where $E_{HLL}^\star$ and $F_{x,HLL}^\star$ are the intermediate states from the HLL scheme.

Proof. Let us recall the HLL intermediate states expressions obtained from the Rankine-Hugoniot relations written accross the numerical waves of speed b_L and b_R are given by (2.109).

In the next step, starting from (2.108) and inserting a few relations from (2.106), we can write :

$$(c\beta_x^\star)^2 (E_L^\star + \Pi^\star) + c^2 \Pi^\star - c^2 P_{xx,L} = b_L (c\beta_x^\star (E_L^\star + \Pi^\star) - F_{x,L}),$$

and

$$(c\beta_x^\star)^2 (E_R^\star + \Pi^\star) + c^2 \Pi^\star - c^2 P_{xx,R} = b_R (c\beta_x^\star (E_R^\star + \Pi^\star) - F_{x,R}).$$

And with (2.111) we finally obtain :

$$(c\beta_x^\star + b_L) F_{x,L} - c\beta_x^\star \Pi^\star b_L - c\beta_x^\star b_L E_L + c^2 \Pi^\star - c^2 P_{xx,L} = 0, \tag{2.114}$$

and

$$(c\beta_x^\star + b_R) F_{x,R} - c\beta_x^\star \Pi^\star b_R - c\beta_x^\star b_R E_R + c^2 \Pi^\star - c^2 P_{xx,R} = 0. \tag{2.115}$$

Then, (2.114)-(2.115) well gives relation (2.113). □

Proposition 9. *The states $\beta_x^\star$ and $\Pi^\star$ verify the relation*

$$\tilde{P}_{xx,HLL} = \Pi^\star + \frac{\beta_x^\star}{c}\tilde{F}_{x,HLL}. \tag{2.116}$$

where $\tilde{F}_{x,HLL}$ and $\tilde{P}_{xx,HLL}$ are the fluxes used in the HLL scheme.

Proof. Let us recall the HLL fluxes obtained from the Rankine-Hugoniot relations written accross the numerical waves of speed b_L and b_R are given by (2.110).

In a first step, we multiply the first equation from (2.108) by b_R and the second one by b_L. And then substracting them, we get :

$$c^2(b_R\tilde{P}_{xx,L} - b_L\tilde{P}_{xx,R}) + b_Rb_L(F^\star_{x,L} - F^\star_{x,R}) = (b_R - b_L)\tilde{P}_{xx,HLL}.$$

We then use (2.106) to replace $\tilde{P}_{xx}$ and $F_x^\star$ in the first member of this equation. We obtain :

$$c\beta_x^\star(b_R\tilde{F}_{x,L} - b_L\tilde{F}_{x,R}) + c^2\Pi^\star(b_R - b_L) + c\beta_x^\star b_Rb_L(E^\star_R - E^\star_L) = (b_R - b_L)\tilde{P}_{xx,HLL}.$$

And finally, thanks to the Rankine-Hugoniot relations in (2.107) we replace the $\tilde{F}_x$ variables. It comes (2.116). □

A second degree equation can then be obtained from (2.113) and (2.116), this equation will allow us to evaluate the $\beta_x^\star$ variable. It is :

$$\beta_x^{\star 2}\tilde{F}_{x,HLL} - c(\tilde{P}_{xx,HLL} + E^\star_{HLL})\beta_x^\star + F^\star_{x,HLL} = 0. \tag{2.117}$$

The fluxes for this solver are then fully specified thanks to (2.111), (2.112), $\Pi^\star$, $\beta_x^\star$ and (2.106). The scheme robustness must then be studied.

2.5.3 Robustness

First the existence of the $\beta_x^\star$ variable is to be checked.

Lemma 10. *Equation (2.117) admits at least one solution in $\mathbb{R}$.*

Proof. We just need to proove that the discriminant of Equation (2.117) is positive. Let D be the discriminant of Equation (2.117) given by :

$$D = c^2(\tilde{P}_{xx,HLL} + E^\star_{HLL})^2 - 4\tilde{F}_{x,HLL}F^\star_{x,HLL}.$$

However, with (2.113) and (2.116) we have :

$$\tilde{F}_{x,HLL}F^\star_{x,HLL} = c^2(\Pi^\star + E^\star_{HLL})(\tilde{P}_{xx,HLL} - \Pi^\star).$$

It follows that a factorisation of D leads to

$$D = c^2(E^\star_{HLL} - \tilde{P}_{xx,HLL} + 2\Pi^\star)^2.$$

Therefore, the discriminant of Equation (2.117) is positive. □

We are now going to show that there only exists one root to Equation (2.117) in the interval $(b_L/c, b_R/c)$. With this point, we first need the following technical statement that will be useful to show the existence of this single root in $(b_L/c, b_R/c)$.

Lemma 11. *Assume b_L and b_R such that $-c \leq b_L \leq 0$ and $0 \leq b_R \leq +c$. Then the two following inequalities hold :*

$$b_L^2 E_L - 2b_L F_L + c^2 P_L \geq 0, \tag{2.118}$$

and

$$b_R^2 E_R - 2b_R F_R + c^2 P_R \geq 0. \tag{2.119}$$

Proof. We get back to the photons distribution function I and we use the moments definitions (1.4) for a given frequency :

$$\begin{aligned} E &= \frac{1}{c}\int_{-1}^{1} I(\mu)d\mu, \\ F &= \frac{1}{c}\int_{-1}^{1} c\mu I(\mu)d\mu, \\ P &= \frac{1}{c}\int_{-1}^{1} \mu^2 I(\mu)d\mu, \end{aligned}$$

where $\mu = cos(\Omega)$. Hence for all b in $\mathbb{R}$ we have :

$$\int_{-1}^{1} (\frac{b}{c} - \mu)^2 I(\mu)d\mu \geq 0, \tag{2.120}$$

which is equivalent to :

$$\int_{-1}^{1} \left(\frac{b^2}{c^2} I(\mu) - 2\frac{b}{c}\mu I(\mu) + \mu^2 I(\mu) \right) d\mu \geq 0. \tag{2.121}$$

And, from the definitions of the radiative energy, flux and pressure tensor, it comes :

$$\frac{b^2}{c} E - 2\frac{b}{c} F + cP \geq 0. \tag{2.122}$$

The proof is achieved. □

Now we turn establishing the existence of $\beta_x^\star$ in $(b_L/c, b_R/c)$.

Lemma 12. *Assume $-1 \leq b_L/c \leq 0 \leq b_R/c \leq 1$. Assume b_L and b_R such that :*

$$b_L b_R E_R - (b_L + b_R) F_R + c^2 P_R \leq 0, \tag{2.123}$$

and

$$b_L b_R E_L - (b_L + b_R) F_L + c^2 P_L \leq 0. \tag{2.124}$$

Let us introduce :

$$\mathbb{P}(z) = z^2 \tilde{F}_{x,HLL} - c(\tilde{P}_{xx,HLL} + E^\star_{HLL})z + F^\star_{x,HLL}. \tag{2.125}$$

Then $\mathbb{P}(\beta)$ admits exactly one root in $(b_L/c, b_R/c)$. This root is denoted $\beta_x^\star$.

Proof. The proof rests upon the fact that $\beta_x^\star \in (b_L/c, b_R/c)$. If $\mathbb{P}(b_L/c)$ and $\mathbb{P}(b_R/c)$ are of opposite signs then $\beta_x^\star$ is the only solution in $(b_L/c, b_R/c)$ to the equation $\mathbb{P}(z) = 0$, where $\mathbb{P}(z)$ is defined by (2.125).

Let us first study the conditions for $\mathbb{P}(b_L/c) \geq 0$ to be verified. We have :

$$\mathbb{P}(b_L/c) = \frac{b_L^2}{c^2}(\tilde{F}_{x,HLL}) - b_L\left(E^\star_{HLL} + \tilde{P}_{xx,HLL}\right) + F^\star_{HLL}. \tag{2.126}$$

Next, multiplying by $(b_R - b_L)$ and replacing intermediate HLL states and fluxes with (2.109) and (2.110), it writes :

$$\begin{aligned}(b_R - b_L)\mathbb{P}(b_L/c) = \frac{b_L^2}{c^2}&\left(b_R F_L - b_L F_R + b_R b_L (E_R - E_L)\right)\\ &-b_L\left(b_R P_L - b_L P_R + \frac{b_R b_L}{c^2}(F_R - F_L)\right)\\ &-b_L\left(b_R E_R - b_L E_L - (F_R - F_L)\right)\\ &+b_R F_R - b_L F_L - c^2\left(P_R - P_L\right),\end{aligned}$$

which can also be written :

$$\begin{aligned}(b_R - b_L)\mathbb{P}(b_L/c) = &\left(1 - \frac{b_R b_L}{c^2}\right)\left(b_L^2 E_L - 2b_L F_L + c^2 P_L\right)\\ &+\left(\frac{b_L^2}{c^2} - 1\right)\left(b_L b_R E_R - (b_L + b_R)F_R + c^2 P_R\right).\end{aligned}$$

And then $\mathbb{P}(b_L/c) \geq 0$ if we have both (2.118) and (2.123) verified. In fact, (2.118) is verified for all b_L in $(-c, 0)$(see Lemma 11).

Let us now verify that $\mathbb{P}(b_R/c) \leq 0$. We have :

$$\mathbb{P}(b_R/c) = \frac{b_R^2}{c^2}\tilde{F}_{x,HLL} - b_R\left(E^\star_{HLL} + \tilde{P}_{xx,HLL}\right) + F^\star_{HLL}. \tag{2.127}$$

Next, multiplying by $(b_R - b_L)$ and replacing intermediate HLL states and fluxes with (2.109) and (2.110), it writes :

$$\begin{aligned}(b_R - b_L)\mathbb{P}(b_R/c) = \frac{b_R^2}{c^2}&\left(b_R F_L - b_L F_R + b_R b_L (E_R - E_L)\right)\\ &-b_R\left(b_R P_L - b_L P_R + \frac{b_R b_L}{c^2}(F_R - F_L)\right)\\ &-b_R\left(b_R E_R - b_L E_L - (F_R - F_L)\right)\\ &+b_R F_R - b_L F_L - c^2\left(P_R - P_L\right).\end{aligned}$$

Therefore :

$$\begin{aligned}(b_R - b_L)\mathbb{P}(b_R/c) = &\left(\frac{b_R b_L}{c^2} - 1\right)\left(b_R^2 E_R - 2b_R F_R + c^2 P_R\right)\\ &+\left(1 - \frac{b_R^2}{c^2}\right)\left(b_L b_R E_L - (b_L + b_R)F_L + c^2 P_L\right).\end{aligned}$$

And then $\mathbb{P}(b_R/c) \leq 0$ if and only if we have both (2.119) and (2.124) verified. (2.119) is here again true for all b_R in $(0, +c)$(see Lemma 11). $\square$

At this stage of the demonstration, for varying b_L and b_R, we know that the scheme is well defined and we are able to approximate the Riemann solver, and particularly the $\beta_x^\star$ 'contact wave velocity' as the solution of a quadratic equation. It now remains to show that the radiative energy positivity and the radiative flux limitation are well preserved. With this aim, we decide to work into a defined space such that the wave speeds are set as :

$$b_L = -c \quad \text{and} \quad b_R = +c.$$

In order to establish the robustness of the developed HLLC like scheme, let us start with two basic lemmas that will be useful in the following.

Lemma 13. *Assume U to be given in $\mathcal{A}$, then we have :*

$$1 \pm 2f + \chi > 0, \tag{2.128}$$

where $f = F_x/cE$ and $\chi = P_{xx}/E$.

Proof. Showing (2.128) is equivalent with showing :

$$E + P_{xx} \pm 2\frac{F_x}{c} > 0. \tag{2.129}$$

After the work by Dubroca-Feugeas [17], the radiative energy E and the radiative flux F_x are the first two moments in the x-direction of a positive radiative intensity I. As a consequence, E and F_x rewrite as follows :

$$E =< 1, I > \quad \text{and} \quad \frac{F_x}{c} =< \mu_x, I > . \tag{2.130}$$

In addition, involving such notations, the radiative pressure is nothing but the following closure :

$$P_{xx} =< \mu_x^2, I > . \tag{2.131}$$

Arguing such a reformulation, we have :

$$E + P_{xx} \pm 2\frac{F_x}{c} =< (1 \pm \mu_x)^2, I >, \tag{2.132}$$

and the proof is achieved. $\square$

Lemma 14. *Assume U to be given in $\mathcal{A}$, then we have :*

$$3 + 2f - \chi > 0, \tag{2.133}$$

where $f = F_x/cE$ and $\chi = P_{xx}/E$.

Proof. Showing (2.133) is equivalent with showing :

$$3E + 2\frac{F_x}{c} - P_{xx} > 0. \tag{2.134}$$

After the work by Dubroca-Feugeas [17], the radiative energy E and the radiative flux F_x are the first two moments in the x-direction of a positive radiative intensity I. As a consequence, E and F_x rewrite as follows :

$$E =< 1, I > \quad \text{and} \quad \frac{F_x}{c} =< \mu_x, I > . \tag{2.135}$$

In addition, involving such notations, the radiative pressure is nothing but the following closure :

$$P_{xx} =< \mu_x^2, I > . \tag{2.136}$$

Arguing such a reformulation, we have :

$$3E + 2\frac{F_x}{c} - P_{xx} =< 3 + 2\mu_x - \mu_x^2, I >, \tag{2.137}$$

where $3 + 2\mu_x - \mu_x^2 > 0$ as $\mu = cos\Omega$ is in $(-1, 1)$. and the proof is achieved. □

We show next that the intermediate states are in the admissible space $\mathcal{A}$. In the extremal case where the signal velocities of the approximate Riemann solver is taken as the speed of light c, we can prove the robustness of the HLLC approximate Riemann solver.

Theorem 15. *Assume U is given in $\mathcal{A}$. If $b_L = -c$ and $b_R = c$, then the approximated states $U_L^\star$ and $U_R^\star$ generated by the HLLC Riemann solver are physically admissible :*

1. *the intermediate energies are positive, $E_L^\star \geq 0$ and $E_R^\star \geq 0$,*
2. *the intermediate states are flux limited, $|F_{x,L}^\star| \leq cE_L^\star$ and $|F_{x,R}^\star| \leq cE_R^\star$.*

Proof. Let us first focus on the left discontinuity. The Rankine-Hugoniot conditions across the left discontinuity are given by the first equations of (2.107) and (2.108). And with $b_L = -c$, it comes :

$$F_{x,L}^* - F_{x,L} = -c(E_L^\star - E_L), \tag{2.138}$$

$$c^2(\tilde{P}_{xx,L} - P_{xx,L}) = -c(F_{x,L}^\star - F_{x,L}). \tag{2.139}$$

The first point of the proof concerns $E_L^\star \leq 0$. As we have from (2.112) that $F_{x,L}^\star = c\beta_x^\star(E_L^\star + \Pi^\star)$ we can deduce from (2.138) that :

$$E_L^\star = \frac{F_{x,L} + cE_L - c\beta_x^\star\Pi^\star}{c(\beta_x^\star + 1)}, \tag{2.140}$$

and

$$F^\star_{x,L} = \beta^\star_x \frac{F_{x,L} + cE_L + c\Pi^\star}{\beta^\star_x + 1}. \tag{2.141}$$

Solving (2.139) thanks to (2.138) and the linearisation $\tilde{P}_{xx,L} = \beta^\star_x F^\star_{x,L}/c + \Pi^\star$ from (2.106), we can deduce from (2.141) that :

$$\Pi^\star = \frac{F_{x,L} + cP_{xx,L} - \beta^\star_x(F_{x,L} + cE_L)}{c(\beta^\star_x + 1)}, \tag{2.142}$$

and by replacing the value of $\Pi^\star$ in (2.140) we obtain :

$$E^\star_L = E_L \frac{(1+f_L)(\beta^\star_x)^2 + (1-\chi_L)\beta^\star_x + 1 + f_L}{(1+\beta^\star_x)^2}, \tag{2.143}$$

where $P_{xx,L} = \chi_L E_L$ and $F_{x,L} = cf_L E_L$ with $f_L \in [-1,1]$ and $\chi_L \in [\frac{1}{3}, 1]$.

In the same way, the value of the flux can be computed from (2.141) and written as :

$$F^\star_{x,L} = c\beta^\star_x E_L \frac{(1+f_L)(1+2f_L+\chi_L)}{(1+\beta^\star_x)^2}. \tag{2.144}$$

In order to prove that $E^\star_L \geq 0$, as $|\beta^\star_x| < 1$, one need to show that the following second order polynom of unknown β_x from (2.143),

$$(1+f_L)(\beta^\star_x)^2 + (1-\chi_L)\beta^\star_x + 1 + f_L,$$

is always non-negative. In fact, as the zero order coefficient is positive, it will be sufficient to show that the discriminant of the polynom is always negative. In fact, this discriminant can be factorised as :

$$(1-\chi_L)^2 - 4(1+f_L)^2 = -(1+2f_L+\chi_L)(3+2f_L-\chi_L) \leq 0.$$

From Lemma (13), we have $(1 \pm 2f_L + \chi_L) \geq 0$ and from Lemma (13), we have $(3 + 2f_L - \chi_L) \geq 0$, hence the radiative energy of the left intermediate state $E^\star_L$ is always non negative.

Now, in order to prove the flux limitation, we need to show that $cE^\star_L \pm F^\star_{x,L} \geq 0$. Thanks to (2.143) and (2.144), these quantities can be written as :

$$cE^\star_L + F^\star_{x,L} = cE_L(1+f_L)$$

and

$$cE^\star_L - F^\star_{x,L} = cE_L \frac{(1+f_L)(\beta^\star_x)^2 + 2(f_l+\chi_L)\beta^\star_x + 1 + f_L}{(1+\beta^\star_x)^2}.$$

Having $f_L \in [-1,1]$ and E_L positive, it is evident that $cE^\star_l + F^\star_{x,L} \geq 0$. Next, the sign of $cE^\star_L - F^\star_{x,L}$ is given by the sign of the following second order polynom of unknown β_x :

$$(1+f_L)(\beta^\star_x)^2 + 2(f_L+\chi_L)\beta^\star_x + 1 + f_L. \tag{2.145}$$

The discriminant of this polynom can be written as :

$$(f_L + \chi_L)^2 - (1 + f_L)^2 = -(1 - \chi_L)(1 + 2f_L + \chi_L).$$

As $(1 \pm 2f_L + \chi_L) \geq 0$ from Lemma (14) and $\chi_L \leq 1$, the discriminant of the polynom (2.145) is always negative. Hence the left state is flux limited. The proof concerning the right state is similar and is omitted here. □

2.5.4 Numerical scheme

Now, working with constant wave speeds $b_L = -c$ and $b_R = +c$ as we will mostly do, we use the obtained approximate Riemann solver

$$U^h(x,t) = \begin{cases} U_L & \text{if } x/t < -c, \\ U_L^\star & \text{if } -c < x/t < c\beta_x^\star, \\ U_R^\star & \text{if } c\beta_x^\star < x/t < c, \\ U_R & \text{if } x/t > c, \end{cases} \tag{2.146}$$

where the wave speed $c\beta_x^\star$ is in $(-c, c)$ and we derive the Godunov type scheme. We consider a uniform mesh defined by the cell $[x_{i-\frac{1}{2}}, x_{i+\frac{1}{2}})$ where $x_{i+\frac{1}{2}} = x_i + \Delta x/2$ for all i in $\mathbb{Z}$ with a constant increment Δx. The time discretisation is given by $t^{n+1} = t^n + \Delta t$ where Δt is restricted according to the CFL like condition :

$$\frac{c\Delta t}{\Delta x} \leq \frac{1}{2}. \tag{2.147}$$

. As usual, at the time t^n, we assume to be known a piecewise constant approximation of $U(x, t^n)$ defined as follows :

$$U^h(x, t^n) = U_i^n \quad \text{if} \quad x \in (x_{i-\frac{1}{2}}, x_{i+\frac{1}{2}}). \tag{2.148}$$

At each cell interface $x_{i+\frac{1}{2}}$, we set the approximate Riemann solver defined by (2.146) with $U_L = U_i^n$ and $U_R = U_{i+1}^n$. Under the CFL restriction (2.147), we thus consider a juxtaposition of non-interacting Riemann solvers (see Figure 2.7), denoted $U^h(x,t)$ for $t \in [t^n, t^n + \Delta t)$.

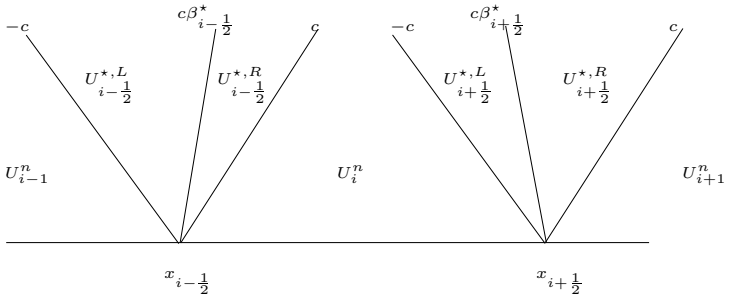

FIGURE 2.7 – Successive Riemann problems

The updated state vector is obtained as follows :

$$U_{i+1}^n = \frac{1}{\Delta x}\int_{x_{i-\frac{1}{2}}}^{x_{i+\frac{1}{2}}} U^h(x, t^n + \Delta t)dx. \tag{2.149}$$

A standard computation gives the following detailed HLLC scheme :

$$\begin{aligned} E_i^{n+1} &= E_i^n - \frac{\Delta t}{\Delta x}(\mathcal{F}^E_{i+\frac{1}{2}} - \mathcal{F}^E_{i-\frac{1}{2}}), \\ (F_x)_i^{n+1} &= (F_x)_i^n - \frac{\Delta t}{\Delta x}(\mathcal{F}^{F_x}_{i+\frac{1}{2}} - \mathcal{F}^{F_x}_{i-\frac{1}{2}}), \end{aligned} \tag{2.150}$$

where we have set the notations as :

$$\begin{aligned} \mathcal{F}^E_{i+\frac{1}{2}} &= \begin{cases} c(\beta_x^\star)_{i+\frac{1}{2}}(E^{\star,L}_{i+\frac{1}{2}} + \Pi^\star_{i+\frac{1}{2}}) & \text{if} \quad (\beta_x^\star)_{i+\frac{1}{2}} > 0, \\ c(\beta_x^\star)_{i+\frac{1}{2}}(E^{\star,R}_{i+\frac{1}{2}} + \Pi^\star_{i+\frac{1}{2}}) & \text{otherwise,} \end{cases} \\ \mathcal{F}^{F_x}_{i+\frac{1}{2}} &= \Pi^\star_{i+\frac{1}{2}} + \frac{(\beta_x^\star)_{i+\frac{1}{2}}}{c}\mathbf{F}^E_{i+\frac{1}{2}}. \end{aligned} \tag{2.151}$$

For the sake of completeness, let us recall that $(\beta_x^\star)_{i+\frac{1}{2}}$ is the single solution in $(-1, 1)$ of the following equation :

$$X^2(\tilde{F}_x^{HLL})_{i+\frac{1}{2}} - c((\tilde{P}_{xx}^{HLL})_{i+\frac{1}{2}} + (E^{\star,HLL})_{i+\frac{1}{2}})X + (F_x^{\star,HLL})_{i+\frac{1}{2}} = 0, \tag{2.152}$$

while we have :

$$\begin{aligned} \Pi^\star_{i+\frac{1}{2}} &= (\tilde{P}_{xx}^{HLL})_{i+\frac{1}{2}} - \frac{(\beta_x^\star)_{i+\frac{1}{2}}}{c}(\tilde{F}_x^{HLL})_{i+\frac{1}{2}}, \\ E^{\star,L}_{i+\frac{1}{2}} &= \frac{1}{1 + (\beta_x^\star)_{i+\frac{1}{2}}}\left(E_i^n - (\beta_x^\star)_{i+\frac{1}{2}}\Pi^\star_{i+\frac{1}{2}} + \frac{(F_x)_i^n}{c}\right), \\ E^{\star,R}_{i+\frac{1}{2}} &= \frac{1}{1 - (\beta_x^\star)_{i+\frac{1}{2}}}\left(E_{i+1}^n + (\beta_x^\star)_{i+\frac{1}{2}}\Pi^\star_{i+\frac{1}{2}} + \frac{(F_x)_{i+1}^n}{c}\right), \end{aligned} \tag{2.153}$$

where we have set :

$$\begin{aligned} E^{\star,HLL}_{i+\frac{1}{2}} &= \frac{cE_{i+1}^n + cE_i^n}{2c} - \frac{1}{2c}((F_x)_{i+1}^n - (F_x)_i^n), \\ (F_x^{\star,HLL})_{i+\frac{1}{2}} &= \frac{(F_x)_{i+1}^n + (F_x)_i^n}{2} - \frac{c}{2}((P_{xx})_{i+1}^n - (P_{xx})_i^n), \\ (\tilde{F}_x^{HLL})_{i+\frac{1}{2}} &= \frac{(F_x)_i^n + (F_x)_{i+1}^n}{2} - \frac{c}{2}(E_{i+1}^n - E_i^n), \\ (\tilde{P}_{xx}^{HLL})_{i+\frac{1}{2}} &= \frac{c(P_{xx})_i^n + c(P_{xx})_{i+1}^n}{2c} - \frac{1}{2c}((F_x)_{i+1}^n - (F_x)_i^n). \end{aligned} \tag{2.154}$$

The derivation of the HLLC type scheme to approximate the weak solution of (2.1) is thus completed.

Let us now set the scheme robustness.

Theorem 16. *Consider an admissible sequence $(U_i^n)_{i\in\mathbb{Z}}$ in $\mathcal{A}$. Define the updated sequence $(U_i^{n+1})_{i\in\mathbb{Z}}$ by the scheme (2.150), (2.151), (2.153) and (2.154) under the CFL like condition (2.147). Then we have U_i^{n+1} is in $\mathcal{A}$ for all $i \in \mathbb{Z}$.*

Proof. Consider $(U_i^n)_{i\in\mathbb{Z}}$ in $\mathcal{A}$ and $(U_i^{n+1})_{i\in\mathbb{Z}}$ defined by (2.150), (2.151), (2.153) and (2.154) under the CFL like condition (2.147). U_i^{n+1} results from the following integration in the cell $(x_{i-\frac{1}{2}}, x_{i+\frac{1}{2}})$, $i \in \mathbb{Z}$:

$$U_i^{n+1} = \frac{1}{\Delta x} \int_{x_{i-\frac{1}{2}}}^{x_{i+\frac{1}{2}}} U^h(x, t^{n+1}) dx, \tag{2.155}$$

where U^h is the juxtaposition of the non interacting approximate Riemann problems. From the theorem 15, we have that each of the approximate states satisfies the energy positivity property and the flux limitation property. Therefore, focusing first on the energy positivity, we can write :

$$E^h(x, t^{n+1}) > 0 \quad \text{for all} \quad x \in (x_{i-\frac{1}{2}}, x_{i+\frac{1}{2}}) \quad \text{and} \quad i \in \mathbb{Z}.$$

So it comes :

$$E_i^{n+1} = \frac{1}{\Delta x} \int_{x_{i-\frac{1}{2}}}^{x_{i+\frac{1}{2}}} E^h(x, t^{n+1}) dx \; > \; 0, \tag{2.156}$$

and then, $E_i^{n+1} > 0$ for all $i \in \mathbb{Z}$.

As for the flux limitation property, we have :

$$F_x^h(x, t^{n+1}) - cE^h(x, t^{n+1}) < 0 \quad \text{for all} \quad x \in (x_{i-\frac{1}{2}}, x_{i+\frac{1}{2}}) \quad \text{and} \quad i \in \mathbb{Z},$$

and

$$F_x^h(x, t^{n+1}) + cE^h(x, t^{n+1}) > 0 \quad \text{for all} \quad x \in (x_{i-\frac{1}{2}}, x_{i+\frac{1}{2}}) \quad \text{and} \quad i \in \mathbb{Z}.$$

So it comes :

$$F_{x,i}^{n+1} - cE_i^{n+1} = \frac{1}{\Delta x} \int_{x_{i-\frac{1}{2}}}^{x_{i+\frac{1}{2}}} (F_x^h(x, t^{n+1}) - cE^h(x, t^{n+1})) dx \; < \; 0, \tag{2.157}$$

then $F_{x,i}^{n+1} - cE_i^{n+1} < 0$ for all $i \in \mathbb{Z}$. And :

$$F_{x,i}^{n+1} + cE_i^{n+1} = \frac{1}{\Delta x} \int_{x_{i-\frac{1}{2}}}^{x_{i+\frac{1}{2}}} (F_x^h(x, t^{n+1}) - cE^h(x, t^{n+1})) dx \; > \; 0, \tag{2.158}$$

then $F_{x,i}^{n+1} + cE_i^{n+1} > 0$ for all $i \in \mathbb{Z}$. Therefore U_i^{n+1} is in $\mathcal{A}$ for all $i \in \mathbb{Z}$. □

2.6 Comparison

Simple 1D numerical tests have been undergone to test the accuracy of the developed schemes. A comparison with Lax-Friedrichs' scheme is made and shown in Figure 2.8. The figure plots a non-dimensional radiative energy. The non-dimensional input data are $E_L = 6$, $F_L = 2$ in the interval $(0, 0.5)$, and $E_R = 5$, $F_R = 3$ in the interval $(0.5, 1)$. The CFL condition is set to 0.5 and the calculation is performed over 200 points. The displayed results are obtained from first order computations and compared to a reference solution obtained with the use of Lax-Friedrichs' scheme over 40000 points.

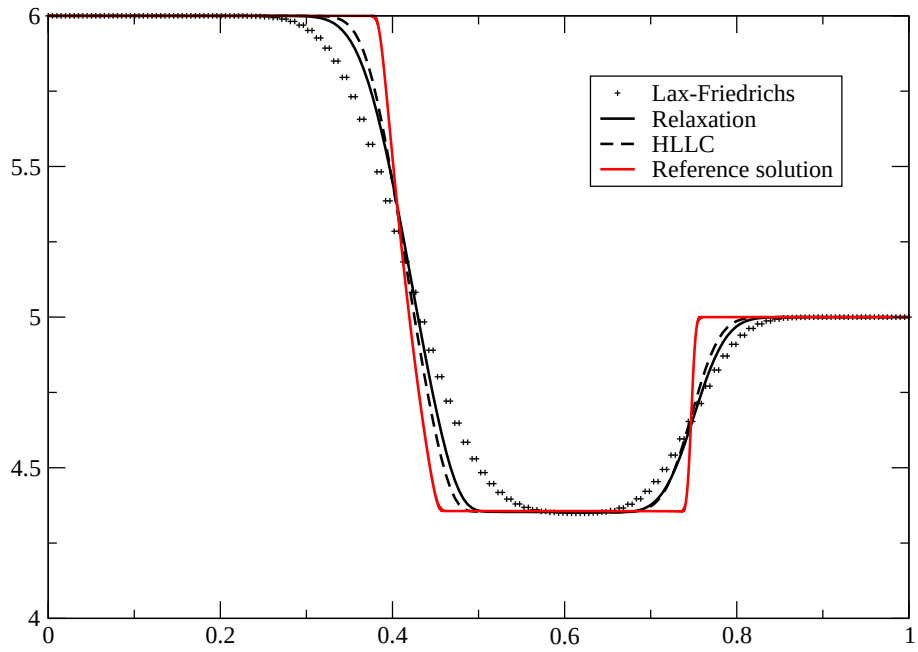

FIGURE 2.8 – Comparison between HLLC, Relaxation and Lax-Friedrichs' schemes.

The graph 2.8 shows that a considerable improvement in accuracy is made thanks to the relaxation and HLLC schemes. Moreover, in the case of the HLLC scheme, a sharper solution than with the relaxation scheme is obtained. The stability conditions determined in Section 2.4.3 are too much restrictive and while the numerical cone narrows, some accuracy is lost. Note that for this 1D case with only x-directed contributions, no difference is observed between the HLL and HLLC schemes. Also note that the Lax-Friedrichs solution is not smooth with the low resolution set for the domain discretisation, whereas HLLC and relaxation provide with smooth solutions.

Relying on the results presented here, the following of the study is focusing on the HLLC scheme that gives more accurate solutions. In Chapter 3, MUSCL-like schemes are applied to raise the resolution to a second-order accuracy solution. A suitable calculation of the solution in the asymptotic regimes is also ensured with the use of an asymptotic-preserving scheme detailed in Chapter 3. A two dimensional extension is then performed, and curvilinear geometries are also envisaged in Chapter 4.

Chapitre 3

High order extension and asymptotic preserving property of the HLLC scheme

3.1 Introduction

So far, we have developed accurate approximate Riemann solvers for the M_1 radiative model. Amongst the relaxation and HLLC like solvers detailed in Chapter 2, we selected the HLLC like solver which reveals to be more accurate, and we add some features to it in order to account for the source terms first, and to raise the accuracy to second order. The following developments presented in this chapter then focus on upgrades of the scheme that would give it additional accuracy capabilities.

Indeed, the HLLC-like Riemann solver developed in the precedent chapter is proved robust, but we aim to apply it to test cases with very stiff source terms and for a wide range of propagation regimes. These regimes are designated as 'asymptotic' regimes, and extend from the diffusion regime in optically thick mediums to the transport regime in transparent mediums. In relation with the treatment of these limit regimes, existing asymptotic preserving schemes are often too sophisticated and based on a control of the Riemann solver (see [25], [21]). In order to preserve our scheme properties and precision capabilities, we choose a method that performs adequate corrections of the source terms.

In order to add even more precision to our model, we suggest to raise the order of accuracy to a second order scheme in space. Amongst various existing methods to raise a scheme to higher orders of accuracy, because some of them tend to enhance instabilities or are not convenient to apply to our scheme, we choose to apply a MUSCL type scheme [41] [47] of which we present the principle in this section. This method involves the use of slope limiters in order to avoid any instability that could be enhanced by a non regular monotony of the solution, and for the admissible states to be preserved.

3.2 Asymptotic preserving scheme

Let us now take the source terms into account and deal with their influence on the radiative propagation regime. Indeed, according to the value of the source terms, the nature of the system to solve may be modified. A relaxation approach to the asymptotic scheme is presented in [7].

The limit regimes are a diffusion regime when the opacities are very big, and a transport regime when the opacities are very small. As discussed in Section 1.3.3, these two asymptotic regimes are properly handled by the M_1 model (as well as the intermediate regime). For our numerical procedure to remain asymptotic preserving, we here present an appropriate method for our needs. The system of equations we consider is the following one dimensional simplified subsystem :

$$\begin{cases} \partial_t E + \partial_x F_x = c\sigma(aT^4 - E), \\ \partial_t F_x + \partial_x P_{xx} = -c\sigma F_x, \\ \partial_t(\rho C_v T) = -c\sigma(aT^4 - E). \end{cases} \tag{3.1}$$

When $\sigma = 0$, the asymptotic behaviour of System (3.1) is a transport-like system of equations written :

$$\begin{cases} \partial_t E + \partial_x F_x = 0, \\ \partial_t F_x + c^2 \partial_x P_{xx} = 0, \\ \partial_t(\rho C_v T) = 0, \end{cases} \tag{3.2}$$

which is actually identical with (2.1) for which we have developed an approximate Riemann solver in the precedent chapter.

Meanwhile, when the opacities become large, the system degenerates into a parabolic system. Indeed, let us introduce a rescaling factor ϵ, a Knudsen number like, to rewrite the system as follows :

$$\begin{cases} \epsilon\partial_t E + \partial_x F_x = \frac{c\sigma}{\epsilon}(aT^4 - E), \\ \epsilon\partial_t F_x + c^2 \partial_x P_{xx} = -\frac{c\sigma}{\epsilon} F_x, \\ \epsilon\partial_t(\rho C_v T) = -\frac{c\sigma}{\epsilon}(aT^4 - E). \end{cases} \tag{3.3}$$

Therefore, when ϵ tends to infinity and in a stationary configuration, as shown in Section 1.3.3, we obtain the following diffusion behaviour in the opaque asymptotic limit :

$$\begin{cases} E = aT^4, \\ F_x = 0, \\ \partial_t(\rho C_v T + aT^4) - div(\dfrac{4cT^3}{3\sigma}\nabla T) = 0. \end{cases} \tag{3.4}$$

This regime is a continuous phenomenon. Note that (3.4) is obtained through a Chapman-Enskog expansion.

These models are important to consider as various regimes can coexist in a given application. We then want to be able to adequately predict the solution in the limit regimes. The work by Gosse-Toscani [22] presents an approach applied to the

Telegraph equations, while the work by Buet-Cordier [10] presents an asymptotic preserving method based on relaxation schemes, and in [6] an asymptotic preserving scheme with application to radiative transfer is shown. However, these methods are asymptotic preserving through a modification of the numerical dependance cone, whereas with the HLLC Riemann solver developed in Chapter 2, we mostly work with fixed numerical cones where $b_L = -c$ and $b_R = c$. We thus want to extend the standard asymptotic preserving methods in order to match our specific needs.

The asymptotic preserving scheme presented here is developed in [6] and we detail here the main particularities.

In Section 2.5, we have proposed a finite volume scheme to approximate the solutions of (3.2). This scheme is easily extended to take into account the matter temperature which is governed by the stationary equation (omitting the source term) :

$$\partial_t(\rho C_v T) = 0. \tag{3.5}$$

Hence, to approximate the free streaming region associated to the M_1 model, and governed by System (3.2), we have derived the following contact discontinuity preserving scheme given by :

$$W_i^{n+1} = W_i^n - \frac{\Delta t}{\Delta x}\left(\mathcal{F}_{i+\frac{1}{2}} - \mathcal{F}_{i-\frac{1}{2}}\right), \tag{3.6}$$

where

$$W_i^n = \left(E_i^n, F_{x,i}^n, T_i^n\right)^T \quad \text{and} \quad \mathcal{F}_{i+\frac{1}{2}} = \left(\mathcal{F}_{i+\frac{1}{2}}^E, \mathcal{F}_{i+\frac{1}{2}}^{F_x}, 0\right)^T,$$

and where the formulas (2.151)-(2.152)-(2.153) are used. For the sake of simplicity in the forthcoming developments, we set $\bar{\mathcal{F}}(W) = (F_x, P_{xx}, 0)^T$.

Now, we propose to modify this method to introduce a suitable discretisation of the source term in order to approximate the system (3.1). In this sense, we adopt a recent approach introduced by Berthon-Turpault [8]. The involved technique used a relevant formulation of the hyperbolic system with source term (3.1).

To address such an issue, we intend to modify the Riemann solver. We suggest first a reformulation of the source terms, introducing the function R, and then write the system of equations (3.1) as :

$$\partial_t W + \partial_x \bar{\mathcal{F}}(W) = c\sigma(R(x, W) - W). \tag{3.7}$$

To determine the function R, assumptions on the opacities must be made.

Lemma 17. *If we set $\sigma^m = max(\sigma, \frac{\sigma a T^3}{\rho C_v})$, then there exists two positive coefficients σ_1 and σ_2 such that :*

$$\begin{aligned} \sigma^m &= \sigma + \sigma_1, \\ \sigma^m &= \frac{\sigma a T^3}{\rho C_v} + \sigma_2. \end{aligned} \tag{3.8}$$

With these notations, the system (3.1) can be written in the form (3.7) if we set $\sigma = c\sigma^m$ *and*

$$R(x,W) = \left(\frac{\sigma a T^4 + \sigma_1 E}{\sigma^m}, \frac{\sigma_1 F_x}{\sigma^m}, \frac{\frac{\sigma E}{\rho C_v} + \sigma_2 T}{\sigma^m} \right)^T . \tag{3.9}$$

Proof. Involving the definition of σ_1 and σ_2, the components of the source term in (3.1) write :

$$\begin{aligned}
\sigma a T^4 + \sigma E = \sigma a T^4 - (\sigma^m - \sigma_1) E = \sigma^m \left(\frac{\sigma a T^4 + \sigma_1 E}{\sigma^m} - E \right), \\
-\sigma F_x = \sigma^m \left(\frac{\sigma_1 F_x}{\sigma^m} - F_x \right), \\
\frac{\sigma E - \sigma a T^4}{\rho C_v} = \sigma^m \left(\frac{\frac{\sigma E}{\rho C_v} + \sigma_2 T}{\sigma^m} - T \right).
\end{aligned}$$

The system (3.1) thus writes in the following form :

$$\begin{aligned}
\partial_t E + \partial_x F_x = c\sigma^m \left(\frac{\sigma a T^4 + \sigma_1 E}{\sigma^m} - E \right), \\
\partial_t F_x + c^2 \partial_x P_{xx} = c\sigma^m (\frac{\sigma_1 F_x}{\sigma^m} - F_x), \\
\partial_t T = c\sigma^m \left(\frac{\frac{\sigma E}{\rho C_v} + \sigma_2 T}{\sigma^m} - T \right).
\end{aligned}$$

The definition of $R(x,W)$ is easily deduced from the last result and the proof is therefore achieved. □

Next, we suggest to modify the intermediate state function involved in the HLLC scheme (2.150). Let us introduce a notation such that the intermediate state $W^\star$ is defined through the HLLC Riemann solver, containing two intermediate states :

$$W^\star(x/t) = \begin{cases} W_L^\star & \text{if} \quad -c < x/t < c\beta_x^\star, \\ W_R^\star & \text{if} \quad c\beta_x^\star < x/t < c, \end{cases} \tag{3.10}$$

where we have set :

$$\begin{aligned}
W_{L,R} = (U_{L,R}, T_{L,R})^T, \\
W_{L,R}^\star = (U_{L,R}^\star, T_{L,R})^T.
\end{aligned} \tag{3.11}$$

Then, the approximate solver $U^{\mathcal{R}}$, defined by (2.146), is corrected as follows :

$$\tilde{W}^{\mathcal{R}}(x/t, W_L, W_R) = \begin{cases} W_L & \text{if} \quad x/t < -c, \\ \alpha W^\star(x/t) + (1-\alpha) R(0^+, W_L) & \text{if} \quad -c < x/t < 0, \\ \alpha W^\star(x/t) + (1-\alpha) R(0^-, W_R) & \text{if} \quad 0 < x/t < c, \\ W_R & \text{if} \quad x/t > c, \end{cases} \tag{3.12}$$

where

$$\alpha = \frac{2}{2 + \sigma \Delta x}, \tag{3.13}$$

where we remind that $U = (E, F_x)$, and $0^{\pm}$ denotes the left and right limit as x/t goes to zero. Note that the corrected intermediate states are a convex combination of the approximate state for the system (3.2) and the source term. Therefore, when $\sigma = 0$, then $\alpha = 1$ and we get the expected transport regime. Whereas, when σ tends to infinity, α tends to zero, the intermediate states tend to R and the diffusion regime is reached.

We adopt the new approximate Riemann solver (3.12) to define a Godunov type scheme. We then consider the juxtaposition, denoted $\tilde{W}^h(x,t)$ for $t \in (t^n, t^n + \Delta t)$, of the Riemann solver stated at each interface $x_{i+\frac{1}{2}}$, and we write :

$$\tilde{W}^h(x, t^n + \Delta t) = \tilde{W}^{\mathcal{R}}\left(\frac{x - x_{i+\frac{1}{2}}}{t^n + \Delta t}; W_i^n, W_{i+1}^n\right). \tag{3.14}$$

And the updated state at $t^n + \Delta t$ in each cell $(x_{i-\frac{1}{2}}, x_{i+\frac{1}{2}})$ is defined as follows :

$$W_i^{n+1} = \frac{1}{\Delta x} \int_{x_{i-\frac{1}{2}}}^{x_{i+\frac{1}{2}}} \tilde{W}^h(x, t^n + \Delta t) dx. \tag{3.15}$$

We now want to write this integral formulation under a conservation form supplemented by a relevant discretisation of the source term. To do so we consider this integral formulation into two parts, one related to the interval $(x_{i-\frac{1}{2}}, x_i)$ and the second one related to the interval $(x_i, x_{i+\frac{1}{2}})$. We have :

$$\begin{aligned} \frac{1}{\Delta x} \int_{x_{i-\frac{1}{2}}}^{x_i} \tilde{W}^h(x, t^n + \Delta t) dx = \frac{\alpha_{i-\frac{1}{2}}}{\Delta x} \int_{x_{i-\frac{1}{2}}}^{x_i} W^h(x, t^n + \Delta t) dx \\ + \frac{1 - \alpha_{i-\frac{1}{2}}}{\Delta x} \left(\int_{x_{i-\frac{1}{2}}}^{x_i + c\Delta t} R(x_{i-\frac{1}{2}}^+, W_i^n) dx + \int_{x_i + c\Delta t}^{x_i} W_i^n dx \right). \end{aligned} \tag{3.16}$$

And a straightforward computation gives :

$$\begin{aligned} \frac{1}{\Delta x} \int_{x_{i-\frac{1}{2}}}^{x_i} \tilde{W}^h(x, t^n + \Delta t) dx = \frac{1}{2} W_i^n + \frac{\Delta t}{\Delta x} \alpha_{i-\frac{1}{2}} \mathcal{F}_{i-\frac{1}{2}} - \frac{\Delta t}{\Delta x} \bar{\mathcal{F}}(W_i^n) \\ + \frac{\Delta t}{\Delta x} (1 - \alpha_{i-\frac{1}{2}}) S_{i-\frac{1}{2}}^+, \end{aligned} \tag{3.17}$$

where

$$S_{i-\frac{1}{2}}^+ = c \left(R(x_{i-\frac{1}{2}}^+, W_i^n) - W_i^n \right) + \bar{\mathcal{F}}(W_i^n), \tag{3.18}$$

with

$$R(x_{i-\frac{1}{2}}^+, W_i^n) = \left(\frac{\sigma a (T_i^n)^4 + \sigma_1 E_i^n}{\sigma^m}, \frac{\sigma_1 F_{x,i}^n}{\sigma^m}, \frac{\frac{\sigma E_i^n}{\rho C_v} + \sigma_2 T_i^n}{\sigma^m} \right)^T. \tag{3.19}$$

Similarly, we have :

$$\begin{aligned}\frac{1}{\Delta x}\int_{x_i}^{x_{i+\frac{1}{2}}}\tilde{W}^h(x,t^n+\Delta t)dx = \frac{1}{2}W_i^n + \frac{\Delta t}{\Delta x}\alpha_{i+\frac{1}{2}}\mathcal{F}_{i+\frac{1}{2}} - \frac{\Delta t}{\Delta x}\bar{\mathcal{F}}(W_i^n)\\ +\frac{\Delta t}{\Delta x}(1-\alpha_{i+\frac{1}{2}})S^-_{i+\frac{1}{2}},\end{aligned} \tag{3.20}$$

where

$$S^-_{i+\frac{1}{2}} = -c\left(W_i^n - R(x^-_{i+\frac{1}{2}},W_i^n)\right) - \bar{\mathcal{F}}(W_i^n), \tag{3.21}$$

with

$$R(x^-_{i+\frac{1}{2}},W_i^n) = \left(\frac{\sigma a(T_i^n)^4+\sigma_1 E_i^n}{\sigma^m}, \frac{\sigma_1 F^n_{x,i}}{\sigma^m}, \frac{\frac{\sigma E_i^n}{\rho C_v}+\sigma_2 T_i^n}{\sigma^m}\right)^T. \tag{3.22}$$

Let us note that through the expressions (3.19) and (3.19), we have that :

$$R(x^+_{i-\frac{1}{2}},W_i^n) = R(x^-_{i+\frac{1}{2}},W_i^n). \tag{3.23}$$

Finally, the scheme reads as follows :

$$\begin{aligned}W_i^{n+1} = W_i^n - \frac{\Delta t}{\Delta x}\left(\alpha_{i+\frac{1}{2}}\mathcal{F}_{i+\frac{1}{2}} - \alpha_{i-\frac{1}{2}}\mathcal{F}_{i-\frac{1}{2}}\right)\\ +\Delta t\left(\frac{1-\alpha_{i-\frac{1}{2}}}{\Delta x}S^+_{i-\frac{1}{2}} + \frac{1-\alpha_{i+\frac{1}{2}}}{\Delta x}S^-_{i\frac{1}{2}}\right).\end{aligned} \tag{3.24}$$

Theorem 18. *Assume W_i^n in $\mathcal{A}$ for all $i\in\mathbb{Z}$. Assume that the scheme (2.150)-(2.151)-(2.153)-(2.154) preserves $\mathcal{A}$ under the CFL condition (2.147). Assume $R(x^+_{i-\frac{1}{2}},W_i^n)$ and $R(x^-_{i+\frac{1}{2}},W_i^n)$ defined by (3.19) and (3.22) are in $\mathcal{A}$. Then the updated state W_i^{n+1} defined by (3.24) is in $\mathcal{A}$ for all $i\in\mathbb{Z}$.*

Proof. Since $\mathcal{A}$ is a convex space, from the definition of W_i^{n+1} given by (3.15), the result is established as soon as we have $\tilde{W}^h(x,t^n+\Delta t)\in\mathcal{A}$ for all $x\in\mathbb{R}$. Now, $\tilde{W}^h$ turns out to be the juxtaposition of the form $\tilde{W}^{\mathcal{R}}$ given by (3.12) composed of states $W_i^n\in\mathcal{A}$ and convex combinations of states in $\mathcal{A}$. We immediately deduce that $\tilde{W}^h(x,t^n+\Delta t)\in\mathcal{A}$ for all $x\in\mathbb{R}$, which concludes the proof. □

In the limit of a rescaling parameter the scheme must be able to restore a relevant approximation of the diffusive equation (1.52). We introduce the Knudsen like number ϵ into the numerical scheme and substitute Δt and σ by $\Delta t/\epsilon$ and σ/ϵ. The rescaled scheme thus reads :

$$\begin{aligned}W_i^{n+1} = W_i^n - \frac{\Delta t}{\Delta x}\left(\alpha^\epsilon_{i+\frac{1}{2}}\mathcal{F}_{i+\frac{1}{2}} - \alpha^\epsilon_{i-\frac{1}{2}}\mathcal{F}_{i-\frac{1}{2}}\right)\\ +\frac{\Delta t}{\epsilon}\left(\frac{\sigma}{2\epsilon+\sigma\Delta x}S^+_{i-\frac{1}{2}} + \frac{\sigma}{2\epsilon+\sigma\Delta x}S^-_{i+\frac{1}{2}}\right),\end{aligned} \tag{3.25}$$

where

$$\alpha^{\epsilon}_{i+\frac{1}{2}} = \frac{2}{2\epsilon + \sigma\Delta x}. \tag{3.26}$$

We study the behaviour of the rescaled scheme as ϵ tends to zero. In the limit of ϵ tending to zero, the scheme (3.25) reduces to :

$$S^{+}_{i-\frac{1}{2}} + S^{-}_{i+\frac{1}{2}} = 0, \tag{3.27}$$

to obtain :

$$(R(x^{-}_{i+\frac{1}{2}}, W^n_i) - W^n_i) + (R(x^{+}_{i-\frac{1}{2}}, W^n_i) - W^n_i) = 0. \tag{3.28}$$

As a consequence, thanks to (3.23), the limit state vector satisfies :

$$E^n_i = a(T^n_i)^4, \quad (F_x)^n_i = 0. \tag{3.29}$$

Concerning the limit temperature, the following discrete diffusion equation is obtained :

$$\begin{aligned}(\rho C_v T + aT^4)^{n+1}_i &= (\rho C_v T + aT^4)^n_i \\ &+c\frac{\Delta t}{\Delta x^2}\left(\frac{(\rho C_v T + aT^4)^n_{i+1} - (\rho C_v T + aT^4)^n_i}{\sigma} + \frac{(\rho C_v T + aT^4)^n_{i-1} - (\rho C_v T + aT^4)^n_i}{\sigma}\right).\end{aligned} \tag{3.30}$$

Then, the limit diffusion equation is written in the following discrete form :

$$(\rho C_v T + aT^4)^{n+1}_i = (\rho C_v T + aT^4)^n_i + \frac{\Delta t}{\Delta x^2}\frac{c}{\sigma}\left(a(T^n_{i+1})^4 - 2a(T^n_i)^4 + a(T^n_{i-1})^4\right) \tag{3.31}$$

However, this diffusion limit is not appropriate as it should involve the diffusion coefficient $\frac{c}{3\sigma}$ rather than $\frac{c}{\sigma}$. In [8], the authors propose a correction to the asymptotic preserving scheme (3.24) in order to obtain the correct asymptotic limit. An additional free parameter $\bar{\sigma} \geq 0$ is introduced, which can be seen as a new degree of freedom essential to ensure the expected diffusive regime.

The source term is thus rewritten and we write (3.1) in the following form :

$$\begin{aligned}\partial_t W + \partial_x \bar{\mathcal{F}}(W) &= c\sigma(R(x,W) - W) + \bar{\sigma}(W - W), \\ &= c(\sigma + \bar{\sigma})\left(\frac{\sigma}{\sigma + \bar{\sigma}}R(x,W) + \frac{\bar{\sigma}}{\sigma + \bar{\sigma}}W - W\right)\end{aligned} \tag{3.32}$$

It then comes :

$$\partial_t W + \partial_x \bar{\mathcal{F}}(W) = c(\sigma + \bar{\sigma})(\bar{R}(x,W) - W), \tag{3.33}$$

where $R(x,W)$ is defined by (3.9) and $\bar{R}(x,W)$ is set as :

$$\bar{R}(x,W) = \frac{\sigma}{\sigma + \bar{\sigma}}R(x,W) + \frac{\bar{\sigma}}{\sigma + \bar{\sigma}}W. \tag{3.34}$$

Let us note that since $\mathcal{A}$ is a convex space and the parameters σ and $\bar{\sigma}$ are positive, we have $\bar{R}(x,W)$ in $\mathcal{A}$ for all $W \in \mathcal{A}$. Moreover, the new formulation is free from the definition of $\bar{\sigma}$. Here again, we then consider the juxtaposition, denoted $W^h(x,t)$ for $t \in (t^n, t^n + \Delta t)$, of the Riemann solver stated at each interface. The updated state vector is defined as (3.15), and the resulting scheme reads :

$$\begin{aligned} W_i^{n+1} = W_i^n - \frac{\Delta t}{\Delta x}\left(\alpha_{i+\frac{1}{2}}\mathcal{F}_{i+\frac{1}{2}} - \alpha_{i-\frac{1}{2}}\mathcal{F}_{i-\frac{1}{2}}\right) \\ +\Delta t\left(\frac{\sigma+\bar{\sigma}_{i-\frac{1}{2}}}{2+(\sigma+\bar{\sigma}_{i-\frac{1}{2}})\Delta x}S^+_{i-\frac{1}{2}} + \frac{\sigma+\bar{\sigma}_{i+\frac{1}{2}}}{2+(\sigma+\bar{\sigma}_{i+\frac{1}{2}})\Delta x}S^-_{i+\frac{1}{2}}\right), \end{aligned} \tag{3.35}$$

where :

$$\begin{aligned} S^-_{i+\frac{1}{2}} &= c(W_i^n - \bar{R}(x^-_{i+\frac{1}{2}}, W_i^n)) - \bar{\mathcal{F}}(W_i^n), \\ S^+_{i-\frac{1}{2}} &= c(\bar{R}(x^+_{i-\frac{1}{2}}, W_{i+1}^n) - W_i^n) + \bar{\mathcal{F}}(W_i^n), \\ \bar{R}(x^-_{i+\frac{1}{2}}, W_i^n) &= \frac{\sigma}{\sigma+\bar{\sigma}_{i+\frac{1}{2}}}R(x^-_{i+\frac{1}{2}}, W_i^n) + \frac{\bar{\sigma}_{i+\frac{1}{2}}}{\sigma+\bar{\sigma}_{i+\frac{1}{2}}}W_i^n, \\ \bar{R}(x^+_{i-\frac{1}{2}}, W_i^n) &= \frac{\sigma}{\sigma+\bar{\sigma}_{i-\frac{1}{2}}}R(x^+_{i-\frac{1}{2}}, W_i^n) + \frac{\bar{\sigma}_{i-\frac{1}{2}}}{\sigma+\bar{\sigma}_{i-\frac{1}{2}}}W_i^n, \end{aligned} \tag{3.36}$$

and

$$\alpha_{i+\frac{1}{2}} = \frac{2}{2+(\sigma+\bar{\sigma}_{i+\frac{1}{2}})\Delta x}. \tag{3.37}$$

Now, the free parameter $\bar{\sigma}_{i+\frac{1}{2}}$ is fixed in order to satisfy the required asymptotic preserving property. Indeed, in the limit of a rescaling parameter the scheme must be able to restore a relevant approximation of the diffusive equation (1.52). With this aim, we introduce the Knudsen like number ϵ into the numerical scheme. As a consequence, we substitute Δt, σ and $\bar{\sigma}_{i+\frac{1}{2}}$ by $\Delta t/\epsilon$, σ/ϵ and $\bar{\sigma}_{i+\frac{1}{2}}/\epsilon$. The rescaled scheme thus reads as follows :

$$\begin{aligned} W_i^{n+1} = W_i^n - \frac{\Delta t}{\Delta x}\left(\alpha^\epsilon_{i+\frac{1}{2}}\mathcal{F}_{i+\frac{1}{2}} - \alpha^\epsilon_{i-\frac{1}{2}}\mathcal{F}_{i-\frac{1}{2}}\right) \\ +\frac{\Delta t}{\epsilon}\left(\frac{\sigma+\bar{\sigma}_{i-\frac{1}{2}}}{2\epsilon+(\sigma+\bar{\sigma}_{i-\frac{1}{2}})\Delta x}S^+_{i-\frac{1}{2}} + \frac{\sigma+\bar{\sigma}_{i+\frac{1}{2}}}{2\epsilon+(\sigma+\bar{\sigma}_{i+\frac{1}{2}})\Delta x}S^-_{i+\frac{1}{2}}\right), \end{aligned} \tag{3.38}$$

where

$$\alpha^\epsilon_{i+\frac{1}{2}} = \frac{2}{2\epsilon+(\sigma+\bar{\sigma}_{i+\frac{1}{2}})\Delta x}. \tag{3.39}$$

Next, we study the behaviour of the rescaled scheme as ϵ tends to zero. In the limit of ϵ tending to zero, the scheme (3.38) reduces to :

$$S^+_{i-\frac{1}{2}} + S^-_{i+\frac{1}{2}} = 0, \tag{3.40}$$

to obtain :

$$(\bar{R}(x^-_{i+\frac{1}{2}}, W_i^n) - W_i^n) + (\bar{R}(x^+_{i-\frac{1}{2}}, W_i^n) - W_i^n) = 0, \tag{3.41}$$

which may also be written :

$$\begin{aligned}\left(\frac{\sigma}{\sigma+\bar{\sigma}_{i+\frac{1}{2}}}R(x^-_{i+\frac{1}{2}}, W_i^n) + \frac{\bar{\sigma}_{i+\frac{1}{2}}}{\sigma+\bar{\sigma}_{i+\frac{1}{2}}}W_i^n - W_i^n\right)\\ + \left(\frac{\sigma}{\sigma+\bar{\sigma}_{i-\frac{1}{2}}}R(x^+_{i-\frac{1}{2}}, W_i^n) + \frac{\bar{\sigma}_{i-\frac{1}{2}}}{\sigma+\bar{\sigma}_{i-\frac{1}{2}}}W_i^n - W_i^n\right) = 0,\end{aligned} \tag{3.42}$$

and it comes :

$$\frac{\sigma}{\sigma+\bar{\sigma}_{i+\frac{1}{2}}}\left(R(x^-_{i+\frac{1}{2}}, W_i^n) - W_i^n\right) + \frac{\sigma}{\sigma+\bar{\sigma}_{i-\frac{1}{2}}}\left(R(x^+_{i-\frac{1}{2}}, W_i^n) - W_i^n\right) = 0. \tag{3.43}$$

As a consequence, thanks to (3.23), the limit state vector satisfies :

$$E_i^n = a(T_i^n)^4, \quad (F_x)_i^n = 0. \tag{3.44}$$

Concerning the limit temperature, the following discrete diffusion equation is obtained :

$$\begin{aligned}&(\rho C_v T + aT^4)_i^{n+1} = (\rho C_v T + aT^4)_i^n\\ &+c\frac{\Delta t}{\Delta x^2}\left(\frac{(\rho C_v T + aT^4)_{i+1}^n - (\rho C_v T + aT^4)_i^n}{\sigma+\bar{\sigma}_{i+\frac{1}{2}}} + \frac{(\rho C_v T + aT^4)_{i-1}^n - (\rho C_v T + aT^4)_i^n}{\sigma+\bar{\sigma}_{i-\frac{1}{2}}}\right).\end{aligned} \tag{3.45}$$

We note that enforcing :

$$\bar{\sigma}_{i+\frac{1}{2}} = \begin{cases} 2\sigma + 3\sigma\rho C_v \dfrac{T_{i+1}^n - T_i^n}{a(T_{i+1}^n)^4 - a(T_i^n)^4} & \text{if} \quad T_{i+1}^n \neq T_i^n, \\ 2\sigma + 3\sigma\rho C_v \dfrac{1}{4a(T_i^n)^3} & \text{else,} \end{cases} \tag{3.46}$$

allows us to write the relevant limit diffusion equation in the following discrete form :

$$(\rho C_v T + aT^4)_i^{n+1} = (\rho C_v T + aT^4)_i^n + \frac{\Delta t}{\Delta x^2}\frac{c}{3\sigma}\left(a(T_{i+1}^n)^4 - 2a(T_i^n)^4 + a(T_{i-1}^n)^4\right) \tag{3.47}$$

Thanks to Theorem 18, the scheme preserves the radiative energy positiveness, the normalized flux limitation, and the total flux conservation. It is also shown that the standard diffusion regime is recovered in the relaxation limit. This asymptotic preserving scheme is tested and used in the numerical experiments presented in the following sections.

3.3 Second order MUSCL scheme

In this section, we aim to improve the accuracy of the solution raising the order of accuracy of the scheme to a second order version in space.

There exist various methods dealing with the order of accuracy of a solution. Some methods, based on the Generalised Riemann Problem (GRP) [5], [42], are too complicated to implement in the case of non-linear problems such as ours. Indeed, these methods are applicable when the Riemann problem is known, which is not our case. High order methods such as the Piecewise Parabolic Method (PPM) also exist (see [14]). And others such as the ENO [26] and WENO [23] methods involve even higher order of precision, but they appear not to be stable enough for the very stiff cases we want to run.

We then choose to make use of the MUSCL (Monotonic Upstream Schemes for Conservation Laws) approach to fulfill the second order accuracy requirement. It was developed, amongst others, by Van Leer [47] (see also [9], [19] and [41]). This method consists in using piecewise linear reconstructions of the solution, instead of piecewise constant functions. This is applied together with a limitation procedure useful to ensure the stability, as the slopes are sometimes too steep.

The method difficulty indeed rests upon the choice of an appropriate slope in order to allow an adequate reconstruction. If the slope is badly chosen, instabilities may occur in the solution. We are then led to limitate this slope, but just enough to avoid instabilities, and not too much for the solution to remain accurate.

Let us remind the procedure used for first order approximations. Let us consider piecewise constant approximations $U^h(x,t^n)$. We have : $U^h(x,t^n) = U_i^n$ if $x \in (x_{i-1/2}, x_{i+1/2})$ where U_i^n is a constant. The process to obtain the updated solution

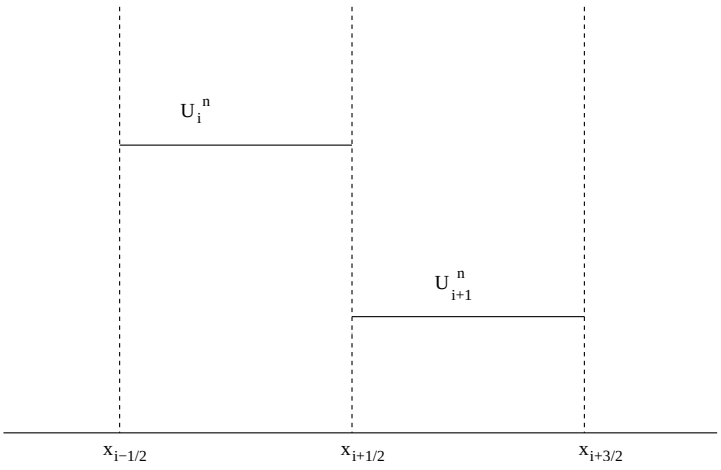

FIGURE 3.1 – First order approximation - Piecewise constant functions

at t^{n+1} is obtained through two steps. The first step is the evolution step where an approximate Riemann solver is used to define an approximation of the solution at the time $t^n + \Delta t$. In a second step, the updated solution is obtained through a juxtaposition of non-interacting Riemann problems at the date $t^n + \Delta t$, under the

CFL-like condition (2.5). The solution is thus obtained through a L^2-projection onto each grid cell :

$$U_i^{n+1} = \frac{1}{\Delta x} \int_{x_{i-1/2}}^{x_{i+1/2}} U^h(x, t^{n+1}) dx.$$

to get :

$$U_i^{n+1} = U_i^n + \frac{\Delta t}{\Delta x} \left(F(U_{i+1}^n, U_i^n) - F(U_i^n, U_{i-1}^n) \right), \tag{3.48}$$

where F is the numerical flux at the $x_{i\pm\frac{1}{2}}$ interface, and the scheme is consistent since $F(U, U) = F(U)$.

Second order reconstuction. Now, we extend the definition in order to obtain a second order scheme in space. In the case of a second order approximation, $U^h(x, t^n)$ is defined thanks to piecewise linear functions $U_i^n(x)$. If $x \in (x_{i-1/2}, x_{i+1/2})$, we have : $U^h(x, t^n) = U_i^n(x)$. And we define :

$$U^h(x, t^n) = U_i^n + s_i(x - x_i) \quad \text{if} \quad x \in (x_{i-1/2}, x_{i+1/2}), \tag{3.49}$$

where s_i is a suitably chosen slope for the $U^h(x, t^n)$ linear function defined locally in the cell $(x_{i-1/2}, x_{i+1/2})$. Therefore, on the edges of the cell, we are led to define

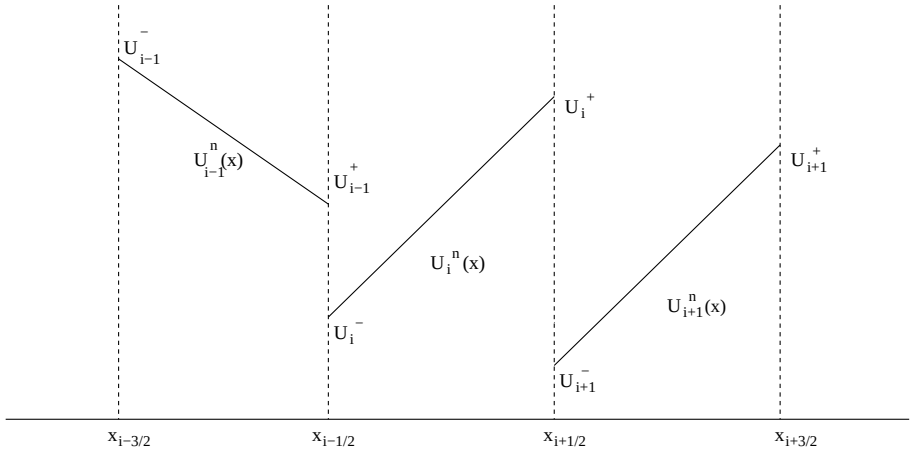

FIGURE 3.2 – Second order approximation - Piecewise linear functions

the 'inner approximations' (approximations at the interfaces) such as :

$$\begin{aligned} U_i^+ &= U_i^n + s_i(x_{i+1/2} - x_i), \\ &= U_i^n + s_i \frac{\Delta x}{2}, \\ U_i^- &= U_i^n + s_i(x_{i-1/2} - x_i), \\ &= U_i^n - s_i \frac{\Delta x}{2}. \end{aligned} \tag{3.50}$$

In the present MUSCL procedure, the approximations at the interfaces are replaced, in the numerical flux F, by reconstructions at the interfaces. And it comes the following flux balance involving the inner approximations defined in (3.50) :

$$U_i^{n+1} = U_i^n - \frac{\Delta t}{\Delta x}\left(F(U_i^+, U_{i+1}^-) - F(U_{i-1}^+, U_i^-)\right). \tag{3.51}$$

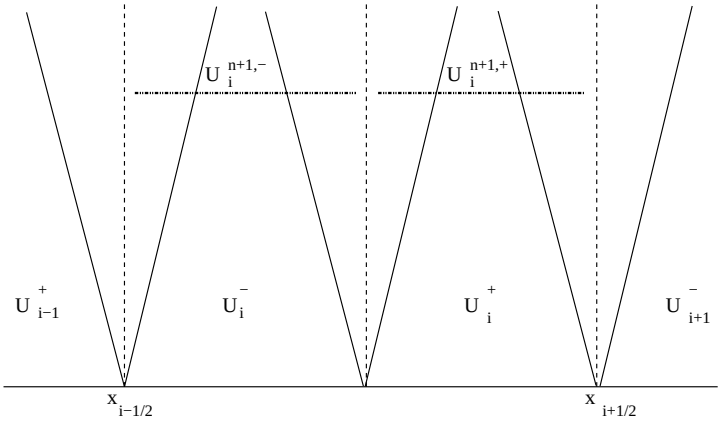

FIGURE 3.3 – Second order reconstruction

We now want to make sure that we are able to preserve the admissible states (defined by the $\mathcal{A}$ admissible space (1.31), with $\mathcal{A}$ convex). We will show that the MUSCL procedure is actually a convex combination of two first order schemes, and this property will allow the preservation of the admissible states.

Indeed, the Riemann problem being resumed as in Figure 3.3, it is possible to write the scheme as in a first order resolution. Let us consider two constant states, one on the interface $(x_{i-1/2}, x_i)$ and the other on the interface $(x_i, x_{i+1/2})$. Then we evolve this sequence of constant states using the first order scheme (3.48), and we obtain the following relations :

$$\begin{cases} U_i^{n+1,-} = U_i^- - \dfrac{\Delta t}{\Delta x/2}\left(F(U_i^-, U_i^+) - F(U_{i-1}^+, U_i^-)\right) & \text{if} \quad x \in (x_{i-\frac{1}{2}}, x_i), \\ U_i^{n+1,+} = U_i^+ - \dfrac{\Delta t}{\Delta x/2}\left(F(U_i^+, U_{i+1}^-) - F(U_i^-, U_i^+)\right) & \text{if} \quad x \in (x_i, x_{i+\frac{1}{2}}). \end{cases} \tag{3.52}$$

Therefore, with :

$$U_i^{n+1} = \frac{1}{2}\left(U_i^{n+1,-} + U_i^{n+1,+}\right), \tag{3.53}$$

we obtain again (3.51). The MUSCL scheme is then nothing but the half-sum (3.53) of $U_i^{n+1,-}$ and $U_i^{n+1,+}$. To ensure the stability, assuming $U_i^{n,-}$ and $U_i^{n,+}$ in $\mathcal{A}$, it is sufficient to have $U_i^{n+1,-}$ and $U_i^{n+1,+}$ in $\mathcal{A}$, which is the case through (3.52) under the appropriate CFL-like condition :

$$c\frac{\Delta t}{\Delta x/2} \leq \frac{1}{2}, \tag{3.54}$$

similar to (2.147).

The MUSCL procedure is thus robust as it preserves the admissible states under the CFL-like condition (3.54). The remaining challenge is now to determine a slope limiter ensuring that this property preserving the admissible states is satisfied.

Slope limiter. The values of $U_i^n(x)$ at the extreme points of the cell are usually called boundary extrapolated values. An important property for these boundary values to verify is that they must not disturb the monotony of the slope. Slope limiters ensure the stability of the scheme by calculating the suitable slope for the monotony to be respected. In the following we will use standard limiters from the litterature. A commonly used tool is the Minmod slope limiter. The Minmod function is defined as follows :

$$minmod(a,b) = max(0, min(a,b)) + min(0, max(a,b)). \tag{3.55}$$

Hence, the boundary extrapolated values are defined as :

$$U_i^{\pm} = U_i^n \pm \Delta U, \tag{3.56}$$

where

$$\Delta U = \frac{1}{2} minmod\left(U_i^n - U_{i-1}^n, U_{i+1}^n - U_i^n\right). \tag{3.57}$$

An other slope limiter used in the computations presented in Chapter 5 is the so-called Superbee limiter [39] [41]. The formulation of the Superbee limiter is as follows :

$$superbee(a,b) = max(0, min(2a, 2b, a+b)) + min(0, max(2a, 2b, a+b)). \tag{3.58}$$

Extra limitation. Let us start with an example showing that the only slope limiters presented above may not be enough to ensure the preservation of the admissible states.

Let us set, in a non-dimensional case where $c = 1$, the three admissible state vectors :

$$U_{i-1} = \begin{pmatrix} 3 \\ 2 \end{pmatrix}, \quad U_i = \begin{pmatrix} 3.1 \\ 3 \end{pmatrix}, \quad \text{and} \quad U_{i+1} = \begin{pmatrix} 4.1 \\ 4 \end{pmatrix}.$$

According to the Minmod limitation (3.57), we have :

$$\Delta U_i = \begin{pmatrix} 0.05 \\ 0.5 \end{pmatrix}.$$

Then, through (3.56), it comes :

$$U_i^+ = \begin{pmatrix} 3.15 \\ 3.5 \end{pmatrix}.$$

We thus have that the energy positivity is preserved, whereas the flux limitation property is not ensured, and U_i^+ is not in $\mathcal{A}$. It then appears that an additional limitation is needed for the MUSCL procedure to be robust.

This extra limitation is defined as follows.

Let us set the parameter θ defined in $(0,1)$ such that :

$$U_i^{\pm} = U_i \pm \theta \Delta U_i. \tag{3.59}$$

Note that when $\theta = 0$, we recover a first order scheme that is known robust from Section 2.5.3. Meanwhile, when $\theta = 1$, we recover the slope defined by the slope limiters such as Minmod or Superbee presented above.

Now, setting

$$\Delta U_i = \begin{pmatrix} \Delta E_i \\ \Delta F_i \end{pmatrix},$$

it remains to determine the θ parameter such that the flux limitation is ensured, which is equivalent to have :

$$(F_i^{\pm})^2 \leq c^2 (E_i^{\pm})^2.$$

Then, with (3.59), we have :

$$(F_i \pm \theta \Delta F_i)^2 \leq c^2 (E_i \pm \theta \Delta E_i)^2,$$

which may also be written as :

$$c^2 E_i^2 - F_i^2 \pm 2\theta \left(c^2 E_i \Delta E_i - F_i \Delta F_i \right) + \theta^2 \left(c^2 \Delta E_i^2 - \Delta F_i^2 \right) \geq 0. \tag{3.60}$$

The reduced determinant for the quadratic equation in (3.60) is :

$$D = \left(c^2 E_i \Delta E_i - F_i \Delta F_i \right)^2 - \left(c^2 E_i^2 - F_i^2 \right) \left(c^2 \Delta E_i^2 - \Delta F_i^2 \right).$$

Therefore, if $D < 0$ then the radiative flux is limited even with $\theta = 1$. And if $D \geq 0$, we determine the solution of the quadratic equation from (3.60). There are four of them, which are expressed as :

$$\theta_j = \frac{\mp \left(c^2 E_i \Delta E_i - F_i \Delta F_i \right) \pm \sqrt{D}}{c^2 \Delta E_i^2 - \Delta F_i^2}, \tag{3.61}$$

and the parameter θ ensuring that the MUSCL procedure preserves the admissible states is determined through the relation :

$$\theta = \min \left(1, \min_{\theta_j > 0} \theta_j \right). \tag{3.62}$$

The applications shown in Chapter 5 and 6 show how accurate the solution is thanks to the second order MUSCL scheme. However, some stability issues may be observed, mostly with the use of the Superbee slope limiter. Note also that the CFL number has to be reduced when performing a second order approximation.

Chapitre 4

Numerical approximation of the M_1 model in two dimensions

4.1 Introduction

In the precedent chapters, we have detailed the development of an HLLC type scheme for the resolution of the hyperbolic M_1 system. A second order reconstruction has been added as an option for the approximation accuracy to be improved, and then the source terms are taken into account through an asymptotic preserving correction allowing a proper treatment of the limit regimes such as diffusion in opaque mediums and transport in transparent mediums.

This HLLC type scheme has been developed in Chapter 2 on the basis of the one dimensional subsystem (2.1). In particular, even if the structure of the considered subsystem (2.1) is only made of two fields, the developments performed in Chapter 2 are done considering a Riemann problem containing three fields : the two non-linear fields, and an additional stationary wave. This three waves configuration has actually been envisaged in expectation of the stationary contact wave that appears when considering the full one dimensional system :

$$\begin{cases} \partial_t E + \partial_x F_x = 0, \\ \partial_t F_x + c^2 \partial_x P_{xx} = 0, \\ \partial_t F_y + c^2 \partial_x P_{xy} = 0. \end{cases} \tag{4.1}$$

The scheme should then be more easily adapted to the System (4.1) and to two dimensional configurations.

Therefore, in this chapter, we choose to include the y-directed contribution of the flux and write the scheme for the complete 1D system. Next, we present the procedure to extend the scheme to two dimensional computational domains. This will allow us to perform calculations on two dimensional cartesian grids. In the second section, as curved bodies are considered in the applications we aim to perform, and in order to be able to refine the computational domain where severe gradients are experienced, we decide to make use of generalised curvilinear coordinates so that we will be able to compute flows around curved bodies. We then present the procedure used to get the original scheme to deal with various geometries.

4.2 Two dimensional scheme

The HLLC scheme is known and explicitly written for a simplified 1D system of the M_1 model in Section 2.5. We now want to write the complete one dimensional scheme that takes into account the F_y component. In a second step, we present the quite straigthforward procedure applied to work with two dimensional domains.

4.2.1 Full 1D scheme

The same study as in Section 2.5.1 is made, except that we now decide to consider the full 1D system of the M_1 model in its conservative form (4.1) where the radiative pressure is defined by :

$$\mathbf{P} = \frac{1}{2}\left((1-\chi(f))\mathbf{I} + (3\chi(f)-1)\frac{\mathbf{F}\otimes\mathbf{F}}{||\mathbf{F}||^2}\right)E \tag{4.2}$$

and where :

$$\chi(f) = \frac{3+4f^2}{5+2\xi}, \quad \xi = \sqrt{4-3f^2}, \quad f = \frac{||\mathbf{F}||}{cE}. \tag{4.3}$$

Let us precise additional notations in this full 1D configuration, we have :

$$\Pi = \frac{1-\chi(f)}{2}E, \tag{4.4}$$

$$\beta_x = \frac{3\chi(f)-1}{2}\frac{F_x}{\|\mathbf{F}\|^2}cE, \tag{4.5}$$

so we can rewrite (4.1) in the following form :

$$\begin{cases} \partial_t E + \partial_x F_x = 0, \\ \partial_t F_x + \partial_x(c\beta_x F_x + c^2\Pi) = 0, \\ \partial_t F_y + \partial_x(c\beta_x F_y) = 0, \end{cases} \tag{4.6}$$

The notations used in the sequel concerning the state variable and the flux function are :

$$U = \begin{pmatrix} E \\ F_x \\ F_y \end{pmatrix}, \mathcal{F} = \begin{pmatrix} F_x \\ c^2 P_{xx} \\ c^2 P_{xy} \end{pmatrix} = \begin{pmatrix} F_x \\ c\beta_x F_x + c^2\Pi \\ c\beta_x F_y \end{pmatrix}.$$

The aim here is to approximate the Riemann solution of (4.1). As the three fields where already taken into account in Section 2.5, the Riemann problem remains as sketched in Figure 2.6 and the approximate Riemann solver is still written in the following form :

$$U^h(x,t) = \begin{cases} U_L & \text{if } x/t < b_L, \\ U_L^\star & \text{if } b_L < x/t < c\beta_x^\star, \\ U_R^\star & \text{if } c\beta_x^\star < x/t < b_R, \\ U_R & \text{if } x/t > b_R, \end{cases} \tag{4.7}$$

where the wave speed $c\beta_x^\star$ is proved to be in (b_L, b_R) according to Lemma 11, and where we have to approximate the intermediate states :

$$U_L^\star = (E_L^\star, F_{x,L}^\star, F_{y,L}^\star) \quad \text{and} \quad U_R^\star = (E_R^\star, F_{x,R}^\star, F_{y,R}^\star)$$

and the approximate flux functions :

$$\tilde{\mathcal{F}}_L = (\tilde{F}_{x,L}, c^2\tilde{P}_{xx,L}, c^2\tilde{P}_{xy,L}) \quad \text{and} \quad \tilde{\mathcal{F}}_R = (\tilde{F}_{x,R}, c^2\tilde{P}_{xx,R}, c^2\tilde{P}_{xy,R}).$$

With this objective in mind, after Harten-Lax-Van Leer [27], we write the Rankine-Hugoniot like conditions across each wave with speed b_L and b_R :

$$\left\{ \begin{array}{l} b_L(U_L^\star - U_L) = \tilde{\mathcal{F}}_L - \mathcal{F}(U_L), \\ b_R(U_R^\star - U_R) = \tilde{\mathcal{F}}_R - \mathcal{F}(U_R). \end{array} \right. \tag{4.8}$$

Several supplementary conditions have to be considered. We enforce the continuity of the Riemann invariants across the middle wave with velocity $c\beta_x^\star$. Hence, we have :

$$\left\{ \begin{array}{l} (\beta_x)_L^\star = (\beta_x)_R^\star = \beta_x^\star, \\ \Pi_L^\star = \Pi_R^\star = \Pi^\star. \end{array} \right. \tag{4.9}$$

We complete the system to be solved by several linearisations which retranscribe the relations linking the Riemann invariants (β_x, Π) and the radiative state vector U. Then, we set :

$$\left\{ \begin{array}{l} F_{x,L}^\star = \tilde{F}_{x,L} = c\beta_x^\star(E_L^\star + \Pi^\star), \\ F_{y,L}^\star = \tilde{F}_{y,L}, \\ \tilde{P}_{xx,L} = \dfrac{\beta_x^\star \tilde{F}_{x,L}}{c} + \Pi^\star, \\ \tilde{P}_{xy,L} = \dfrac{\beta_x^\star \tilde{F}_{y,L}}{c}, \end{array} \right. \quad \left\{ \begin{array}{l} F_{x,R}^\star = \tilde{F}_{x,R} = c\beta_x^\star(E_R^\star + \Pi^\star), \\ F_{y,R}^\star = \tilde{F}_{y,R}, \\ \tilde{P}_{xx,R} = \dfrac{\beta_x^\star \tilde{F}_{x,R}}{c} + \Pi^\star, \\ \tilde{P}_{xy,R} = \dfrac{\beta_x^\star \tilde{F}_{y,R}}{c}. \end{array} \right. \tag{4.10}$$

The unknowns $U_{L,R}^\star$, $\tilde{F}_{L,R}$ and $(\beta_x^\star, \Pi^\star)$ are solution of the system made of (4.8) and (4.10). As a consequence, the approximate Riemann solver (4.7) is fully characterised as soon as the system (4.8)-(4.10) is solved. Let us specify the Rankine-Hugoniot relations for each component of the state vector, it comes the already known relations (2.107) and (2.108), and concerning the third component, we have :

$$\left\{ \begin{array}{l} c^2(\tilde{P}_{xy,L} - P_{xy,L}) = b_L(F_{y,L}^\star - F_{y,L}), \\ c^2(\tilde{P}_{xy,R} - P_{xy,R}) = b_R(F_{y,R}^\star - F_{y,R}). \end{array} \right. \tag{4.11}$$

Considering the full 1D system (4.1) does not change anything to the second degree equation (2.117) involving the $\beta_x^\star$ variable, speed of the Riemann problem contact wave. Indeed, Equations (2.113) and (2.116) are still valid.

The intermediate state radiative variables $E_{L,R}^\star$ and $F_{x,L,R}^\star$ are determined as in (2.111) and (2.112). Let us remind these relations :

$$\left\{ \begin{array}{l} E_L^\star = \dfrac{F_{x,L} - b_L E_L - c\beta_x^\star \Pi^\star}{c\beta_x^\star - b_L}, \\ E_R^\star = \dfrac{F_{x,R} - b_R E_R - c\beta_x^\star \Pi^\star}{c\beta_x^\star - b_R}, \end{array} \right. \tag{4.12}$$

and

$$\begin{cases} F^\star_{x,L} = c\beta^\star_x(E^\star_L + \Pi^\star), \\ F^\star_{x,R} = c\beta^\star_x(E^\star_R + \Pi^\star). \end{cases} \tag{4.13}$$

Meanwhile, $F^\star_{y,L,R}$ is given by :

$$\begin{cases} F^\star_{y,L} = \dfrac{c^2 P_{xy,L} - b_L F_{y,L}}{c\beta^\star_x - b_L}, \\ F^\star_{y,R} = \dfrac{c^2 P_{xy,R} - b_R F_{y,R}}{c\beta^\star_x - b_R}. \end{cases} \tag{4.14}$$

Numerical scheme. Now, we use the obtained approximate Riemann solver (4.7) to derive the Godunov type scheme in the case where $b_L = -c$ and $b_R = c$,. We consider a uniform mesh defined by the cell $[x_{i-\frac{1}{2}}, x_{i+\frac{1}{2}})$ where $x_{i+\frac{1}{2}} = x_i + \Delta x/2$ for all i in $\mathbb{Z}$ with a constant increment Δx. The time discretisation is given by $t^{n+1} = t^n + \Delta t$ where Δt is restricted according to a CFL-like condition given by :

$$c\frac{\Delta t}{\Delta x} \leq \frac{1}{2}. \tag{4.15}$$

As usual, at the time t^n, we assume to be known a piecewise constant approximation of $U(x, t^n)$ defined as follows :

$$U^h(x, t^n) = U^n_i \quad \text{if} \quad x \in (x_{i-\frac{1}{2}}, x_{i+\frac{1}{2}}). \tag{4.16}$$

At each cell interface $x_{i+\frac{1}{2}}$, we set the approximate Riemann solver defined by (4.7) with $U_L = U^n_i$ and $U_R = U^n_{i+1}$. Under the CFL restriction (4.15), we thus consider a juxtaposition of non-interacting Riemann solvers (see Figure 4.1), denoted $U^h(x, t)$ for $t \in [t^n, t^n + \Delta t)$.

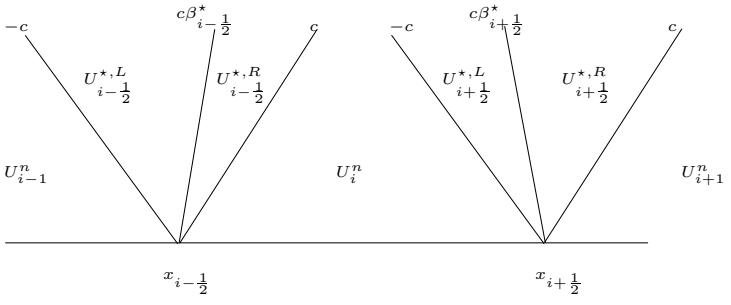

FIGURE 4.1 – Successive Riemann problems

The updated state vector is obtained as follows :

$$U^n_{i+1} = \frac{1}{\Delta x}\int_{x_{i-\frac{1}{2}}}^{x_{i+\frac{1}{2}}} U^h(x, t^n + \Delta t)dx. \tag{4.17}$$

A standard computation gives the following detailed scheme :

$$\begin{aligned}
E_i^{n+1} &= E_i^n - \frac{\Delta t}{\Delta x}(\mathcal{F}^E_{i+\frac{1}{2}} - \mathcal{F}^E_{i-\frac{1}{2}}),\\
(F_x)_i^{n+1} &= (F_x)_i^n - \frac{\Delta t}{\Delta x}(\mathcal{F}^{F_x}_{i+\frac{1}{2}} - \mathcal{F}^{F_x}_{i-\frac{1}{2}}),\\
(F_y)_i^{n+1} &= (F_y)_i^n - \frac{\Delta t}{\Delta x}(\mathcal{F}^{F_y}_{i+\frac{1}{2}} - \mathcal{F}^{F_y}_{i-\frac{1}{2}}),
\end{aligned} \tag{4.18}$$

where we have set the notations as :

$$\begin{aligned}
\mathcal{F}^E_{i+\frac{1}{2}} &= \begin{cases} c(\beta_x^\star)_{i+\frac{1}{2}}(E^{\star,L}_{i+\frac{1}{2}} + \Pi^\star_{i+\frac{1}{2}}) & \text{if} \quad (\beta_x^\star)_{i+\frac{1}{2}} > 0,\\ c(\beta_x^\star)_{i+\frac{1}{2}}(E^{\star,R}_{i+\frac{1}{2}} + \Pi^\star_{i+\frac{1}{2}}) & \text{otherwise,}\end{cases}\\
\mathcal{F}^{F_x}_{i+\frac{1}{2}} &= \Pi^\star_{i+\frac{1}{2}} + \frac{(\beta_x^\star)_{i+\frac{1}{2}}}{c}\mathbf{F}^E_{i+\frac{1}{2}},\\
\mathcal{F}^{F_y}_{i+\frac{1}{2}} &= \begin{cases} \dfrac{(\beta_x^\star)_{i+\frac{1}{2}}}{1+(\beta_x^\star)_{i+\frac{1}{2}}}\left((P_{xy})_i^n + \dfrac{(F_y)_i^n}{c}\right) & \text{if} \quad (\beta_x^\star)_{i+\frac{1}{2}} > 0,\\ \dfrac{-(\beta_x^\star)_{i+\frac{1}{2}}}{1-(\beta_x^\star)_{i+\frac{1}{2}}}\left((P_{xy})_{i+1}^n + \dfrac{(F_y)_{i+1}^n}{c}\right) & \text{otherwise.}\end{cases}
\end{aligned} \tag{4.19}$$

For the sake of completeness, let us recall that $(\beta_x^\star)_{i+\frac{1}{2}}$ is the single solution in $(-1,1)$ of the following equation :

$$X^2(\tilde{F}_x^{HLL})_{i+\frac{1}{2}} - c((\tilde{P}_{xx}^{HLL})_{i+\frac{1}{2}} + (E^{\star,HLL})_{i+\frac{1}{2}})X + (F_x^{\star,HLL})_{i+\frac{1}{2}} = 0, \tag{4.20}$$

while we have :

$$\begin{aligned}
\Pi^\star_{i+\frac{1}{2}} &= (\tilde{P}_{xx}^{HLL})_{i+\frac{1}{2}} - \frac{(\beta_x^\star)_{i+\frac{1}{2}}}{c}(\tilde{F}_x^{HLL})_{i+\frac{1}{2}},\\
E^{\star,L}_{i+\frac{1}{2}} &= \frac{1}{1+(\beta_x^\star)_{i+\frac{1}{2}}}\left(E_i^n - (\beta_x^\star)_{i+\frac{1}{2}}\Pi^\star_{i+\frac{1}{2}} + \frac{(F_x)_i^n}{c}\right),\\
E^{\star,R}_{i+\frac{1}{2}} &= \frac{1}{1-(\beta_x^\star)_{i+\frac{1}{2}}}\left(E_{i+1}^n + (\beta_x^\star)_{i+\frac{1}{2}}\Pi^\star_{i+\frac{1}{2}} + \frac{(F_x)_{i+1}^n}{c}\right),
\end{aligned} \tag{4.21}$$

and where the $E^{\star,HLL}_{i+\frac{1}{2}}$, $(F_x^{\star,HLL})_{i+\frac{1}{2}}$, $(\tilde{F}_x^{HLL})_{i+\frac{1}{2}}$ and $(\tilde{P}_{xx}^{HLL})_{i+\frac{1}{2}}$ variables are defined by (2.154). The derivation of the HLLC type scheme to approximate the weak solution of (4.1) is thus completed.

Robustness. The full 1D scheme here detailed is as much stable as the scheme developed in Section 2.5 with the simplified 1D system. The lemmas 10, 12 remain satisfied and the proofs are unchanged. As, for the robustness, it is numerically tested through the test cases presented in Chapters 5 and 6.

Next, let us deal with the accuracy of the scheme. We are here aiming to prove that the scheme (4.18)-(4.21) preserves the stationary contact waves.

Theorem 19. *Consider an admissible sequence $(U_i^n)_{i\in\mathbb{Z}}$ in $\mathcal{A}$. For all i in $\mathbb{Z}$, assume $(\beta_x)_i^n = 0$ where $(\beta_x)_i^n := (\beta_x)(U_i^n)$ is defined by (4.5). Let us set Π a positive constant. Assume $\Pi_i^n = \Pi$ for all $i \in \mathbb{Z}$ where $\Pi_i^n := \Pi(U_i^n)$ is given by (4.4). Then we have $U_i^{n+1} = U_i^n$ for all $i \in \mathbb{Z}$.*

This result is a direct consequence of the property of the approximate Riemann solver to exactly capture the stationary contact discontinuity.

Lemma 20. *Let U_L and U_R be given in $\mathcal{A}$, and assume that U_L and U_R define a stationary contact wave; namely $(\beta_x)_L = (\beta_x)_R = 0$ and $\Pi_L = \Pi_R$. Then the approximate Riemann solver, defined by (4.7), coincides with the exact stationary contact wave solution :*

$$U^{\mathcal{R}}(x,t) = \begin{cases} U_L & \text{if} \quad x/t < 0, \\ U_R & \text{if} \quad x/t > 0. \end{cases} \tag{4.22}$$

Proof. Arguing the definition of β_x, given by (4.5), as soon as $\beta_x = 0$ we have $F_x = 0$. As a consequence $(F_x)_L = (F_x)_R = 0$. In addition, the radiative pressure reads :

$$\begin{array}{l} (P_{xx})_L = (P_{xx})_R = \Pi, \\ (P_{xy})_L = (P_{xy})_R = 0. \end{array} \tag{4.23}$$

From these values, we note that $F_x^{\star,HLL} = 0$ and $\tilde{P}_{xx}^{HLL} = \Pi$.

We now evaluate the intermediate states of $U^{\mathcal{R}}$. First, $\beta_x^\star$ is the main solution in $(-1,1)$ of the following equation :

$$X^2 \tilde{F}_x^{HLL} - cX(\tilde{P}_{xx}^{HLL} + E^{\star,HLL}) = 0. \tag{4.24}$$

Hence, we have $\beta_x^\star = 0$. Next, from (2.116) we have $\Pi^\star = \Pi$. Concerning the radiative energy, from (4.12) we obtain $E_L^\star = E_L$ and $E_R^\star = E_R$. Arguing (4.10) we get $F_{x,L}^\star = F_{x,R}^\star = 0$ while (4.14) gives $F_{y,L}^\star = F_{y,L}$ and $F_{y,R}^\star = F_{y,R}$. The proof is thus completed. □

Proof.of Theorem 19.
Invoking Lemma 20, the expected result is an immediate consequence of the updated state vector definition (4.17). □

4.2.2 Validation of the full 1D scheme

The numerical test shown in Section 2.6 is here reproduced in a full one dimensional configuration. The above detailed HLLC-like aproximate Riemann solver is tested against the relaxation model presented in Section 2.4 and against the classical HLL and Lax-Friedrichs schemes. The comparison is shown in Figure 4.2

The figure plots a non-dimensional radiative energy. The non-dimensional input data are $E_L = 6$, $F_{x,L} = 2$, $F_{y,L} = 1$ in the interval $(0, 0.5)$, and $E_R = 5$, $F_{x,R} = 3$,

$F_{y,R} = 2$ in the interval $(0.5, 1)$. The CFL condition is set to 0.5 and the calculation is performed over 200 points. The displayed results are obtained from first order computations and compared to a reference solution obtained with the use of Lax-Friedrichs' scheme over 40000 points.

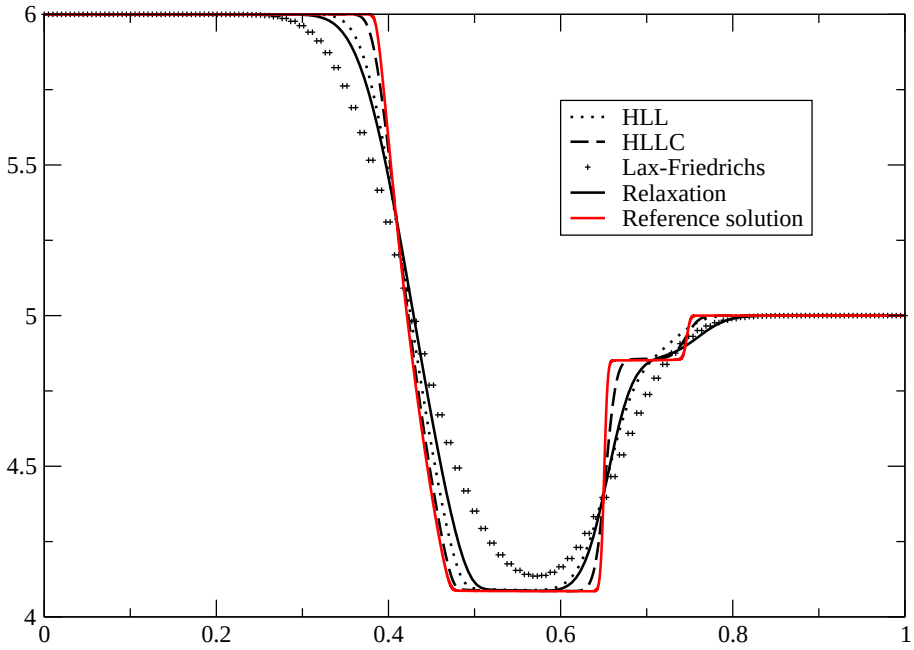

FIGURE 4.2 – Comparison between HLLC, HLL, Relaxation and Lax-Friedrichs' schemes.

The graph 4.2 confirms the improvement in accuracy made thanks to the HLLC approximate Riemann solver developed in this work. We can still observe that some accuracy is lost in the case of the relaxation solver because of the very restrictive conditions ensuring the robustness of the scheme, the results are even worse than those given by the HLL scheme.

Note that, for this full 1D case, a difference is observed between the HLL and HLLC schemes, whereas when performing this test in the simplified 1D configuration in Section 2.6, there was no difference between the HLL and HLLC schemes. Moreover, the HLLC scheme provides us with a sharper approximation of the solution.

4.2.3 2D extension

Let us get back to the notations and define the following vectors :

$$U = \begin{pmatrix} E \\ F_x \\ F_y \end{pmatrix}, \mathcal{F} = \begin{pmatrix} F_x \\ c^2 P_{xx} \\ c^2 P_{xy} \end{pmatrix} \text{and} \, \mathcal{G} = \begin{pmatrix} F_y \\ c^2 P_{yx} \\ c^2 P_{yy} \end{pmatrix}.$$

With these notations, we can write the system to be solved in 2D configurations. It takes the form :

$$\partial_t U + \partial_x \mathcal{F} + \partial_y \mathcal{G} = 0. \tag{4.25}$$

With $\mathcal{A} = \frac{\partial \mathcal{F}}{\partial U}$ and $\mathcal{B} = \frac{\partial \mathcal{G}}{\partial U}$ it comes :

$$\partial_t U + \mathcal{A}\partial_x U + \mathcal{B}\partial_y U = 0.$$

Equation (4.25) is integrated over a finite volume C_i.

$$\int_{c_i} (\partial_t U + \partial_x \mathcal{F} + \partial_y \mathcal{G})\, dxdy = 0, \tag{4.26}$$

where $\partial_x \mathcal{F} + \partial_y \mathcal{G}$ can also be written $div_{x,y} \begin{pmatrix} \mathcal{F} \\ \mathcal{G} \end{pmatrix}$. It comes that (4.26) is equivalent to :

$$\partial_t \int_{c_i} U + \int_{\partial_{c_i}} \begin{pmatrix} \mathcal{F} \\ \mathcal{G} \end{pmatrix} \cdot \vec{n}\, d\sigma = 0. \tag{4.27}$$

The method to determine the solution of a given 2D problem is therefore resumed to solving a Riemann problem in the $\vec{n}$ direction, where :

$$\begin{pmatrix} \mathcal{F} \\ \mathcal{G} \end{pmatrix} \cdot \vec{n} = \mathcal{F} n_x + \mathcal{G} n_y = \begin{pmatrix} F_x n_x + F_y n_y \\ c^2 P_{xx} n_x + c^2 P_{yx} n_y \\ c^2 P_{xy} n_x + c^2 P_{yy} n_y \end{pmatrix} = \begin{pmatrix} \vec{F} \cdot \vec{n} \\ c^2 \bar{\bar{P}} \vec{n} \end{pmatrix}.$$

The Riemann problem in two dimensions is resumed in Figure 4.3.

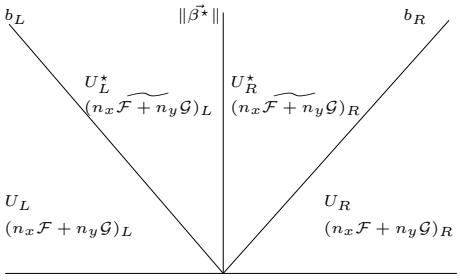

FIGURE 4.3 – HLLC 2D scheme

In addition, the radiative tensor $\bar{\bar{P}}$, which expression is given in Section 2.5.1, is written again with 2D notations. We remind some usual relations between vectors :

$$\vec{F} \otimes \vec{F}\vec{n} = \vec{F}^t \vec{F}\vec{n} = (\vec{F} \cdot \vec{n})\vec{F}.$$

Hence, once the vectors have been put right, we obtain :

$$\bar{\bar{P}}\vec{n} = \frac{1 - \chi(f)}{2} E\vec{n} + \frac{3\chi(f) - 1}{2} \frac{E}{\|\vec{F}\|^2} (\vec{F} \cdot \vec{n})\vec{F}.$$

The additional relations

$$\Pi = \frac{1-\chi(f)}{2}E, \quad \frac{3\chi(f)-1}{2} = \|\vec{\beta}\|\frac{\|\vec{F}\|}{cE} \quad \text{and} \quad \frac{\vec{F}}{\|\vec{F}\|} = \frac{\vec{\beta}}{\|\vec{\beta}\|}$$

allow us to write :

$$\bar{\bar{P}}\vec{n} = \Pi\vec{n} + (\vec{\beta}\cdot\vec{n})\frac{\vec{F}}{c}. \tag{4.28}$$

From (4.28), we can write the flux vector as :

$$\begin{pmatrix} \mathcal{F} \\ \mathcal{G} \end{pmatrix}\cdot\vec{n} = \begin{pmatrix} \vec{F}\cdot\vec{n} \\ c^2\Pi\vec{n} + c(\vec{\beta}\cdot\vec{n})\vec{F} \end{pmatrix}. \tag{4.29}$$

We do not detail here the well known Rankine-Hugoniot relations, it is straightforward to obtain the expressions of the radiative variables in the star region. Let us specify the linearisations with the 2D notations :

$$\begin{cases} \vec{F^\star}_{L,R} = \tilde{\vec{F}}_{L,R} = c\vec{\beta^\star}(E^\star_{L,R} + \Pi^\star), \\ \tilde{\bar{\bar{P}}}_{L,R}\vec{n} = \Pi^\star\vec{n} + (\vec{\beta^\star}\cdot\vec{n})\dfrac{\tilde{\vec{F}}_{L,R}}{c}. \end{cases} \tag{4.30}$$

The intermediate states of the Riemann problem are :

$$\begin{cases} E^\star_L = \dfrac{(\vec{F}\cdot\vec{n})_L - b_L E_L - c(\vec{\beta^\star}\cdot\vec{n})\Pi^\star}{c(\vec{\beta^\star}\cdot\vec{n}) - b_L}, \\ E^\star_R = \dfrac{(\vec{F}\cdot\vec{n})_R - b_R E_R - c(\vec{\beta^\star}\cdot\vec{n})\Pi^\star}{c(\vec{\beta^\star}\cdot\vec{n}) - b_R}, \end{cases} \tag{4.31}$$

and the intermediate fluxes are written :

$$\begin{cases} (\vec{F^\star}\cdot\vec{n})_L = \dfrac{c^2(\bar{\bar{P}}\vec{n})_L\cdot\vec{n} - b_L(\vec{F}\cdot\vec{n})_L - c^2\Pi^\star}{c(\vec{\beta^\star}\cdot\vec{n}) - b_L}, \\ (\vec{F^\star}\cdot\vec{n})_R = \dfrac{c^2(\bar{\bar{P}}\vec{n})_R\cdot\vec{n} - b_R(\vec{F}\cdot\vec{n})_R - c^2\Pi^\star}{c(\vec{\beta^\star}\cdot\vec{n}) - b_R}. \end{cases} \tag{4.32}$$

With 2D notations, the relations (2.113) and (2.116) are written as follows :

$$\vec{F}^\star_{HLL}\cdot\vec{n} = c(\vec{\beta^\star}\cdot\vec{n})(E^\star_{HLL} + \Pi^\star), \tag{4.33}$$

$$(\tilde{\bar{\bar{P}}}_{HLL}\vec{n})\cdot\vec{n} = \Pi^\star + (\vec{\beta^\star}\cdot\vec{n})\frac{\tilde{\vec{F}}_{HLL}\cdot\vec{n}}{c}. \tag{4.34}$$

And the second order degree equation of unknown $\vec{\beta^\star}\cdot\vec{n}$ is then :

$$(\vec{\beta^\star}\cdot\vec{n})^2(\tilde{\vec{F}}_{HLL}\cdot\vec{n}) - c(\vec{\beta^\star}\cdot\vec{n})\left(E^\star_{HLL} + (\tilde{\bar{\bar{P}}}_{HLL}\vec{n})\cdot\vec{n}\right) + \vec{F}^\star_{HLL}\cdot\vec{n} = 0. \tag{4.35}$$

Discretisation. The two dimensional procedure is said to be based on a dimensional splitting. Indeed, it sums up two resolutions of the 1D Riemann problem in each direction. For every time step, in the case of cartesian grids, the numerical fluxes are obtained in the x-direction first and then in the y-direction, and are used to update the solution at t^{n+1}.

We consider a uniform mesh defined by the finite volumes $(x_{i-\frac{1}{2}}, x_{i+\frac{1}{2}})\times(y_{i-\frac{1}{2}}, y_{i+\frac{1}{2}})$ where $x_{i+\frac{1}{2}} = x_i + \Delta x/2$ and $y_{i+\frac{1}{2}} = y_i + \Delta y/2$ for all i in $\mathbb{Z}$ with constant increments Δx and Δy. The time discretisation is given by $t^{n+1} = t^n + \Delta t$ where Δt is restricted according to a CFL-like condition given by :

$$c\frac{\Delta t}{\Delta x + \Delta y} \leq \frac{1}{2}. \tag{4.36}$$

Let us write the discretised form of Equation (4.25), we have :

$$\frac{1}{\Delta t}\left(U_{i,j}^{n+1} - U_{i,j}^{n}\right) + \frac{1}{\Delta x}\left(\mathcal{F}_{i+1/2,j} - \mathcal{F}_{i-1/2,j}\right) + \frac{1}{\Delta y}\left(\mathcal{G}_{i,j+1/2} - \mathcal{G}_{i,j-1/2}\right) = 0. \tag{4.37}$$

As usual, at the time t^n, we assume to be known a piecewise constant approximation of $U^h(x, t^n)$ defined as follows :

$$\begin{cases} U^h(x, t^n) = U_i^n & \text{if} \quad x \in (x_{i-\frac{1}{2}}, x_{i+\frac{1}{2}}), \\ U^h(y, t^n) = U_i^n & \text{if} \quad y \in (y_{i-\frac{1}{2}}, y_{i+\frac{1}{2}}). \end{cases} \tag{4.38}$$

At each cell interface $x_{i+\frac{1}{2}}$ or $y_{i+\frac{1}{2}}$ (depending on the direction in which we are working), we set the approximate Riemann solver defined by (4.7) with $U_L = U_i^n$ and $U_R = U_{i+1}^n$. Under the CFL restriction (4.36), we thus consider a juxtaposition of non-interacting Riemann solvers, which solutions are denoted $U^h(x, t)$ if working in the x direction or $U^h(y, t)$ if working in the y direction, and for $t \in [t^n, t^n + \Delta t)$.

The scheme (4.18)-(4.21) is then applied in each direction and the solution at the time $t^n + \Delta t$ is obtained through (4.37).

The stability and robustness of the 2D scheme thus depends on the 1D scheme for which the important properties have be shown in the precedent section. That is to say, the 2D HLLC type scheme presented here has its approximate solution in the admissible space $\mathcal{A}$, i.e. the energy positivity and flux limitation are preserved. Moreover, through the ability of the scheme to preserve the stationary contact wave, an improved accuracy is ensured compared to the Harten-Lax-Van Leer [27] scheme.

4.3 Curvilinear extension

As mentioned earlier, with the starting point of a two dimensional cartesian scheme, we want to make it able to deal with curved geometries i.e. with the associated curvilinear meshes, as well as with mesh refinements in areas where strong gradients are involved. The principle is presented in the following, as well as the parametric coefficients useful for this transformation.

4.3.1 The conform transformation

First, let us remind the M_1 system in its 2D form :

$$\partial_t U + \partial_x \mathcal{F} + \partial_y \mathcal{G} = 0, \tag{4.39}$$

which is integrated over a cell C_i :

$$\int_{c_i} (\partial_t U + \partial_x \mathcal{F} + \partial_y \mathcal{G})\, dxdy = 0.$$

We here aim to map the physical (x, y) space to a generalised curvilinear coordinate (ξ, η) space, in order to be able to consider rather arbitrary geometries. The discretisation of the governing equations is done in the generalised coordinate space, so are the computations.

An application φ defined as $\varphi : (x, y) \longrightarrow (\xi, \eta)$ ensures the conform transformation from the physical space to the generalised coordinate space. Indeed, for

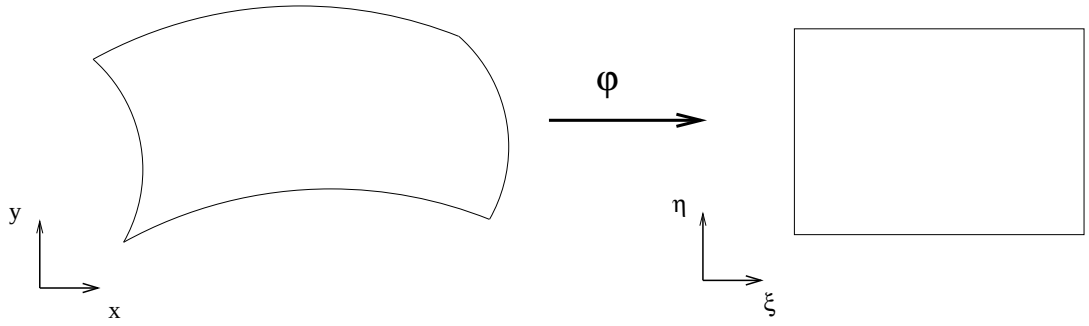

FIGURE 4.4 – Conform transformation

the spatial derivatives to be properly evaluated at every time step, we consider two distinct domains :

– the physical domain where the physical variables are initialized,
– the mathematical domain where the problem equations are discretised.

Computations in a two-dimensional curved region are more appropriately performed along a wall that coincides with lines of constant η for instance. In such a configuration, location along the wall will then correspond to specific values of ξ in the computational domain. The use of such a coordinate space is particularly justified when grid refinement is needed in parts of the physical domain where severe gradients are expected.

It is assumed that there is a single-valued relationship between the generalised coordinates and the physical coordinates, written as : $\xi = \xi(x, y)$ and $\eta = \eta(x, y)$. And the spatial derivatives of any function f depending on the physical variables (x, y) can be written :

$$\partial_x f = \partial_x \xi \partial_\xi f + \partial_x \eta \partial_\eta f,$$

$$\partial_y f = \partial_y \xi \partial_\xi f + \partial_y \eta \partial_\eta f.$$

The governing equations are transformed into corresponding equations containing partial derivatives with respect to ξ and η. The Jacobian matrix $\underline{J}$ of the transformation is :

$$\underline{J} = \begin{pmatrix} \partial_x \xi & \partial_y \xi \\ \partial_x \eta & \partial_y \eta \end{pmatrix},$$

and the determinant of the Jacobian matrix is given by :

$$J = \partial_x \xi \, \partial_y \eta - \partial_y \xi \, \partial_x \eta = \frac{1}{\partial_\xi x \, \partial_\eta y - \partial_\eta x \, \partial_\xi y},$$

so the inverse of the Jacobian matrix can be written as follows :

$$\underline{J}^{-1} = \begin{pmatrix} \partial_\xi x & \partial_\eta x \\ \partial_\xi y & \partial_\eta y \end{pmatrix} = \frac{1}{J} \begin{pmatrix} \partial_y \eta & -\partial_y \xi \\ -\partial_x \eta & \partial_x \xi \end{pmatrix}, \tag{4.40}$$

where $1/J$ actually represents the considered cell surface. Note that the involved derivatives of the mathematical coordinates as functions of the physical coordinates are usually designated as the parametric coefficients.

Proposition 21. *Eq.(4.39) can be written in the form :*

$$\frac{\partial \hat{U}}{\partial t} + \frac{\partial \hat{\mathcal{F}}}{\partial \xi} + \frac{\partial \hat{\mathcal{G}}}{\partial \eta} = 0, \tag{4.41}$$

where

$$\begin{cases} \hat{U} = \dfrac{U}{J}, \\ \hat{\mathcal{F}} = \left(\dfrac{\partial_x \xi}{J} \mathcal{F} + \dfrac{\partial_y \xi}{J} \mathcal{G} \right), \\ \hat{\mathcal{G}} = \left(\dfrac{\partial_x \eta}{J} \mathcal{F} + \dfrac{\partial_y \eta}{J} \mathcal{G} \right). \end{cases}$$

Proof. Let us denote by φ an arbitrary test function. The integration of Eq.(4.39) writes :

$$\int_0^{+\infty} \int_{c_i} \left(\frac{\partial W}{\partial t} + \frac{\partial \mathcal{F}}{\partial x} + \frac{\partial \mathcal{G}}{\partial y} \right) \varphi dt dx dy = 0.$$

Through Green's theorem, this is equivalent with writing :

$$\int_0^{+\infty} \int_{c_i} \left(W \frac{\partial \varphi}{\partial t} + \mathcal{F} \frac{\partial \varphi}{\partial x} + \mathcal{G} \frac{\partial \varphi}{\partial y} \right) dt dx dy = 0.$$

Using the following relations :

$$\begin{cases} dxdy = \frac{1}{J} d\xi d\eta, \\ \nabla\varphi = \nabla\xi \frac{\partial\varphi}{\partial\xi} + \nabla\eta \frac{\partial\varphi}{\partial\eta}, \end{cases}$$

we then obtain :

$$\int_0^{+\infty} \int_{c_i} \left[\frac{W}{J} \frac{\partial\varphi}{\partial t} + \left(\frac{\partial_x \xi}{J} \mathcal{F} + \frac{\partial_y \xi}{J} \mathcal{G} \right) \frac{\partial\varphi}{\partial\xi} + \left(\frac{\partial_x \eta}{J} \mathcal{F} + \frac{\partial_y \eta}{J} \mathcal{G} \right) \frac{\partial\varphi}{\partial\eta} \right] dt d\xi d\eta = 0.$$

Therefore it comes :

$$\int_0^{+\infty} \int_{c_i} \left[\frac{\partial}{\partial t} \left(\frac{W}{J} \right) + \frac{\partial}{\partial\xi} \left(\frac{\partial_x \xi}{J} \mathcal{F} + \frac{\partial_y \xi}{J} \mathcal{G} \right) + \frac{\partial}{\partial\eta} \left(\frac{\partial_x \eta}{J} \mathcal{F} + \frac{\partial_y \eta}{J} \mathcal{G} \right) \right] \varphi dt d\xi d\eta = 0, \quad (4.42)$$

which completes the proof. □

Note that if a source term is involved, the differential equation in curvilinear coordinates takes the form :

$$\frac{\partial \hat{U}}{\partial t} + \frac{\partial \hat{\mathcal{F}}}{\partial\xi} + \frac{\partial \hat{\mathcal{G}}}{\partial\eta} = \hat{S}, \quad (4.43)$$

where $\hat{S} = \frac{S}{J}$.

4.3.2 Numerical approximation

The equations are discretised in the (ξ, η) domain, and the mapping is arranged so that the mapping is uniform and rectangular in the computational domain. Curved lines of the physical grid are approximated by tangent lines, see Fig.(4.5). A discretisation of (4.41) gives :

$$\frac{1}{\Delta t} \left(\hat{U}_{i,j}^{n+1} - \hat{U}_{i,j}^{n} \right) + \frac{1}{\Delta\xi} \left(\hat{\mathcal{F}}_{i+1/2,j} - \hat{\mathcal{F}}_{i-1/2,j} \right) + \frac{1}{\Delta\eta} \left(\hat{\mathcal{G}}_{i,j+1/2} - \hat{\mathcal{G}}_{i,j-1/2} \right) = 0. \quad (4.44)$$

where

$$\begin{cases} \hat{\mathcal{F}}_{i+1/2,j} = \left(\frac{\partial_x \xi}{J} \right)_{i+1/2,j} \frac{\mathcal{F}_{i,j} + \mathcal{F}_{i+1,j}}{2} + \left(\frac{\partial_y \xi}{J} \right)_{i+1/2,j} \frac{\mathcal{G}_{i,j} + \mathcal{G}_{i+1,j}}{2}, \\ \left(\frac{\partial_x \xi}{J} \right)_{i+1/2,j} = (\partial_\eta y)_{i+1/2,j} = \frac{y_{B_{i,j}} - y_{C_{i,j}}}{\Delta\eta}, \\ \left(\frac{\partial_y \xi}{J} \right)_{i+1/2,j} = -(\partial_\eta x)_{i+1/2,j} = -\frac{x_{B_{i,j}} - x_{C_{i,j}}}{\Delta\eta}, \end{cases} \quad (4.45)$$

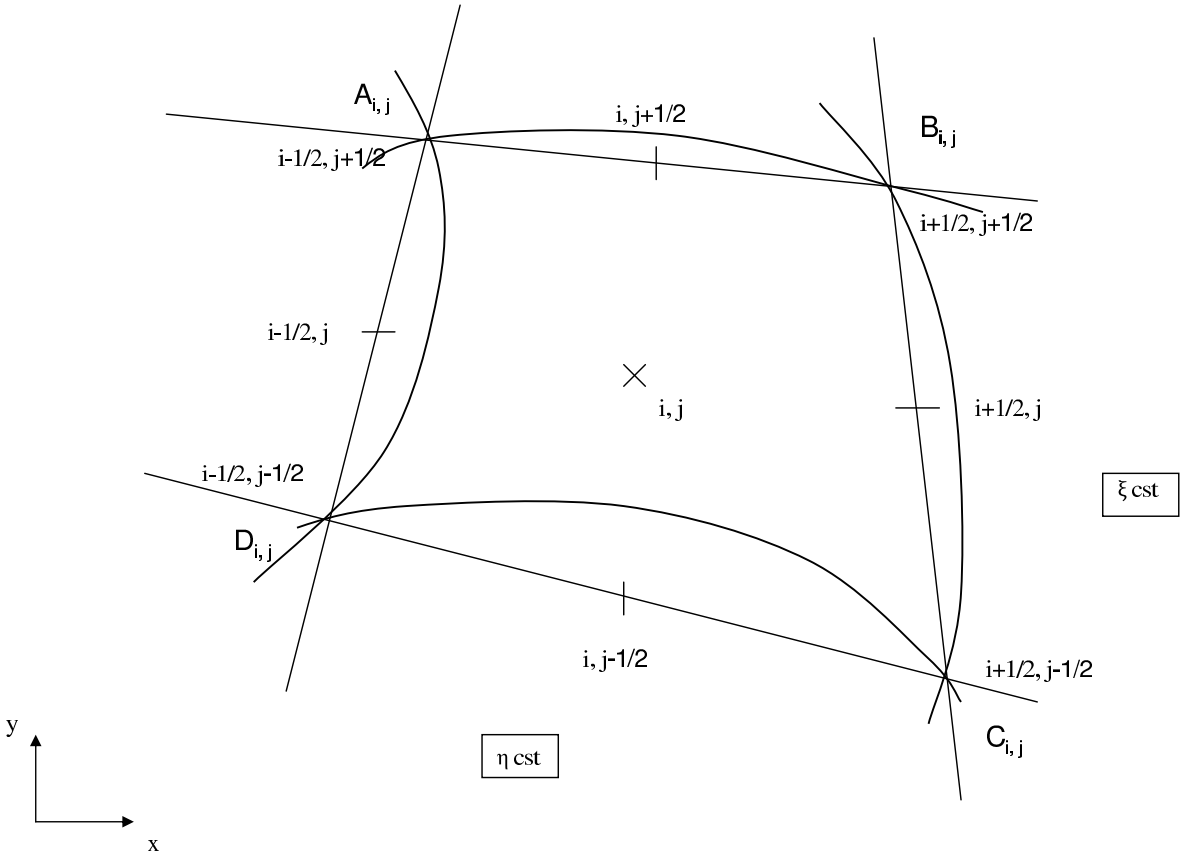

FIGURE 4.5 – Two dimensional curved grid

and

$$\begin{cases} \hat{\mathcal{G}}_{i,j+1/2} = \left(\dfrac{\partial_x \eta}{J}\right)_{i,j+1/2} \dfrac{\mathcal{F}_{i,j} + \mathcal{F}_{i,j+1}}{2} + \left(\dfrac{\partial_y \eta}{J}\right)_{i,j+1/2} \dfrac{\mathcal{G}_{i,j} + \mathcal{G}_{i,j+1}}{2}, \\ \left(\dfrac{\partial_x \eta}{J}\right)_{i,j+1/2} = -\left(\partial_\xi y\right)_{i,j+1/2} = -\dfrac{y_{B_{i,j}} - y_{A_{i,j}}}{\Delta\xi}, \\ \left(\dfrac{\partial_y \eta}{J}\right)_{i,j+1/2} = \left(\partial_\xi x\right)_{i,j+1/2} = \dfrac{x_{B_{i,j}} - x_{A_{i,j}}}{\Delta\xi}, \end{cases} \tag{4.46}$$

and finally :

$$\begin{cases} J_{i,j}^{-1} = \left(\dfrac{\partial_x \xi}{J}\right)_{i,j} \left(\dfrac{\partial_y \eta}{J}\right)_{i,j} - \left(\dfrac{\partial_y \xi}{J}\right)_{i,j} \left(\dfrac{\partial_x \eta}{J}\right)_{i,j}, \\ \left(\dfrac{\partial_x \xi}{J}\right)_{i,j} = \dfrac{1}{2}\left[\left(\dfrac{\partial_x \xi}{J}\right)_{i+1/2,j} + \left(\dfrac{\partial_x \xi}{J}\right)_{i-1/2,j}\right], \\ \left(\dfrac{\partial_x \eta}{J}\right)_{i,j} = \dfrac{1}{2}\left[\left(\dfrac{\partial_x \eta}{J}\right)_{i,j+1/2} + \left(\dfrac{\partial_x \eta}{J}\right)_{i,j-1/2}\right]. \end{cases} \tag{4.47}$$

The unitary normal vector $\vec{n}$ for each face of the control volume also needs to be

specified. We have :

$$\begin{cases} \begin{pmatrix} \frac{\partial_x \xi}{J} \\ \frac{\partial_y \xi}{J} \end{pmatrix}_{i,j+1/2} = \begin{pmatrix} \partial_\eta y \\ -\partial_\eta x \end{pmatrix}_{i,j+1/2} = \frac{1}{\Delta\eta} \begin{pmatrix} y_{B_{i,j}} - y_{C_{i,j}} \\ -(x_{B_{i,j}} - x_{C_{i,j}}) \end{pmatrix} = \frac{1}{\Delta\eta} \begin{pmatrix} x_{B_{i,j}} - x_{C_{i,j}} \\ y_{B_{i,j}} - y_{C_{i,j}} \end{pmatrix}^\perp, \\ \begin{pmatrix} \frac{\partial_x \eta}{J} \\ \frac{\partial_y \eta}{J} \end{pmatrix}_{i+1/2,j} = \begin{pmatrix} -\partial_\xi y \\ \partial_\xi x \end{pmatrix}_{i+1/2,j} = \frac{1}{\Delta\xi} \begin{pmatrix} -(y_{B_{i,j}} - y_{A_{i,j}}) \\ x_{B_{i,j}} - x_{A_{i,j}} \end{pmatrix} = \frac{1}{\Delta\xi} \begin{pmatrix} x_{B_{i,j}} - x_{A_{i,j}} \\ y_{B_{i,j}} - y_{A_{i,j}} \end{pmatrix}^\perp. \end{cases}$$

For instance, considering the face $AB_{i,j}$, its normal vector $\vec{n}_{(AB)_{i,j}}$ is colinear to $\Delta\xi \begin{pmatrix} \frac{\partial_x \eta}{J} \\ \frac{\partial_y \eta}{J} \end{pmatrix}_{i+1/2,j}$, as for the face $BC_{i,j}$, its normal vector $\vec{n}_{(BC)_{i,j}}$ is colinear to $\Delta\eta \begin{pmatrix} \frac{\partial_x \xi}{J} \\ \frac{\partial_y \xi}{J} \end{pmatrix}_{i,j+1/2}$.

Numerical experiments are performed in Chapter 5 to test the relevance of the curvilinear coordinates. A classical observation is that the use of a curvilinear mesh introduces numerical dissipation in the solution.

Indeed, the evaluation of the parametric coefficients, useful for the conform transformation realised here, plays an important part in the resulting precision of the scheme. The evaluation of these parametric coefficients may be done in two different ways : they can either be analytically calculated if the function of the transformation is known, or they can be numerically computed. The first option is used when one want to avoid the troncature error. However, it is known that this choice leads to a deterioration of the order of accuracy used in the numerical scheme. The second option that evaluates the derivatives from the discretised scheme is then prefered as it preserves the global accuracy. In addition, calculating the parametric coefficients numerically ensures the consistency, i.e. the constant solutions are preserved through this geometric conservation law.

Nevertheless, the use of a conform transformation in multidimensional domains adds up troncature errors, and particularly, they are related to the mesh orthogonality. The typical error is indeed proportional to $cos\theta$ where θ is the angle between the ξ and η axis. The numerical experiment presented in Section 5.7 tests the influence and pertinence of the use of curvilinear coordinates in the case of a curved geometry.

Chapitre 5

Validation of the approach

5.1 Introduction

So far, we have focused on the construction of an accurate Riemann solver for the resolution of the M_1 hyperbolic system. This Riemann solver is an HLLC scheme that has the capability to capture the contact wave and is then supposed to be more accurate than the classical HLL scheme.

In the present chapter, as well as in the following, we display the results obtained through various test cases, and compare the HLLC scheme against the HLL scheme. We here aim to put into light the improvement brought to the radiative transfer solution. In this chapter, we focus exclusively on pure radiative test cases, where no hydrodynamic calculation is involved. The first test case is a one dimensional case, whereas the next test cases are two dimensional.

The first test case deals with a Marshak wave. Indeed, we look at the time propagation of a heat wave and compare the HLL and HLLC numerical schemes, applied to the M_1 model, with a kinetic solution of the radiative transfer equation. We there check that there is no deterioration of the 1D solution through the numerical scheme.

From the second test case, two dimensional configurations are considered. A shadow cone is first studied. It is a very stiff test case, with an important discontinuity at the interface. It allows us to test the capability of the HLLC scheme to capture the discontinuity with good accuracy. The usefulness of the second order MUSCL and asymptotic preserving schemes is also tested through this test case.

We also look at the ability of our radiative transfer code to deal with curvilinear geometries through the elliptic thick cloud test case, where a cartesian mesh is considered in the first place, and then a curvilinear mesh is tried on. It is the only test case to involve non-constant opacities as the opacity is defined as a function of the density and temperature.

The numerical diffusion of the scheme is quantified through the single light beam test case. And finally, a double light beam case shows that some limitations are induced by the use of the M_1 model, even if the behaviour of the model is very satisfactory in the transport regime.

Finally, the last application deals with a medical application of radiation such as the photons propagation in brain tissues. Indeed, when using radiation as a cure, it

is important not to damage the healthy areas. For the simulation of human tissues, matters with scattering opacities non equal to zero are considered. We are then confronted to a test case with scattering mediums. The calculations are performed based on the M_1 model and with both HLL and HLLC schemes, and are compared to microscopic resolutions of the radiative transfer equation.

5.2 Marshak wave

The Marshak wave is a one-dimensional test case that focuses on the chronometric behaviour of the scheme. The considered slab of material is initially cool and in radiative equilibrium. A heat wave enters the domain and its evolution is observed.

In [46], this test case is used to compare the M_1 model behaviour with various diffusion models where the flux is artificially limited. The flux limiters used are Kershaw's, Minerbo's, Levermore's, and Levermore-Lorentz's [33]. A kinetic model is used as a reference solution, and it turns out that amongst the diffusion models, some are late, and some are early compared to the kinetic solution. However, the M_1 model is quite well behaving timewise, and is then a better choice when computing non-stationary cases.

Having this in mind, we here aim to check that using a different scheme than the usual HLL scheme does not deteriorate the non-stationary solution.

This test case is composed of a slab of material that extends from $x = 0m$ to $x = 0.1m$, and which mesh is divided into 10 cells. The initial temperature is equal to $300K$ and the source on the left side of the domain has a temperature of $1000K$. This source generates a thermal wave propagating into the initially cold medium.

The opacity is assumed to be constant equal to $\sigma = 100\,m^{-1}$ and the density multiplied by the heat capacity is $\rho C_v = 10^{-4} Jm^{-3}K^{-1}$. The results are compared with a full transport calculation [6] used as a reference solution. Note that in the present slab, the mean free path is equal to $\lambda = 1/\sigma = 0.01\,m$, which is actually equal to the spatial resolution $\Delta x = 0.01\,m$. The cells are then too large for the absorption phenomenon to be numerically visible, and the computation is thus comparable to a transport calculation.

The radiative temperature profiles observed at $t = 1.33\,10^{-7}s$ are shown in Figure 5.1. Computations with both HLL and HLLC schemes are compared, and also with the additional asymptotic scheme denoted 'AP' and presented in Section 3.2.

Results without the asymptotic preserving scheme are clearly early compared to the reference solution, whereas the use of the asymptotic preserving scheme allows a much better agreement with the reference solution. We also note that the HLLC and HLL schemes both give similar results from a chronometric point of view.

An additional test is performed with more points for the computation, that is to say with 50 points along the path (whereas there were only 10 before). The results are shown in Figure 5.2. We observe that the solution shows a rather good fit with the reference solution.

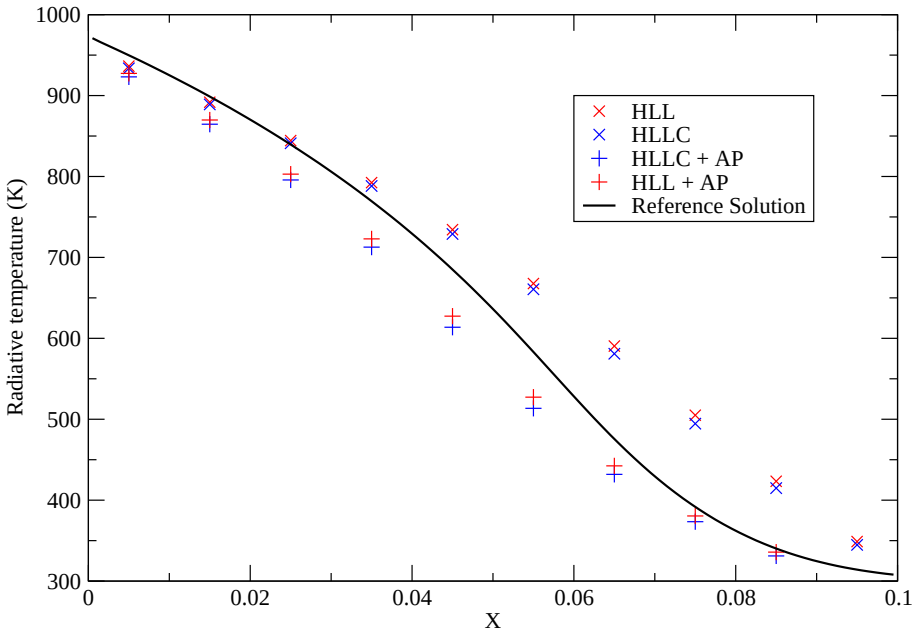

FIGURE 5.1 – Marshak wave at $t = 1.33\,10^{-7}s$.

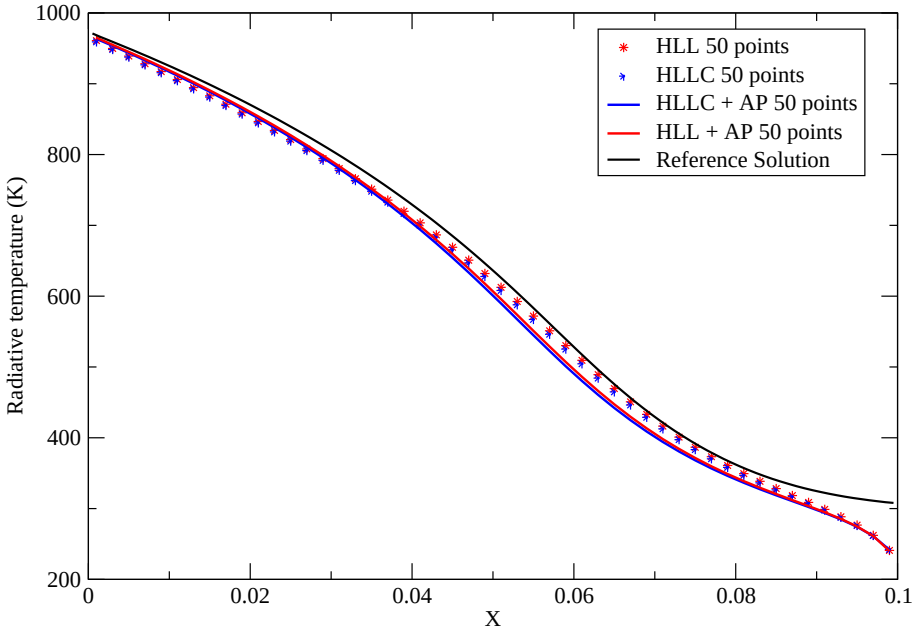

FIGURE 5.2 – Marshak wave at $t = 1.33\,10^{-7}s$ with a refined spatial discretisation.

5.3 Shadow cone

Let us now consider a 2D problem in order to focus on two dimensional effects. The design of this test case has been defined in order to realise mathematical experiments in the sense that the data have no physical meaning. This test case has very stiff initial conditions and demonstrates really well the quality of the solution provided by the solver. The discontinuity is indeed well pronounced between the matter

and transparent mediums, the input conditions we set in these regions and at their boundaries. Tests have been performed in [6], and we show here some improvements from the results obtained in [6].

The considered domain extends from $x = 0m$ to $x = 2m$ and from $y = 0m$ to $y = 1m$ as shown on Figure 5.3. Computations shown here are run on a 80×40 cartesian mesh. The domain is composed of a dense material ($\rho C_v = 8.6\,10^4 Jm^{-3}K^{-1}$ and $\sigma = 2\,10^5\,m^{-1}$) and a transparent region. A free streaming beam adjacent to the dense material enters the domain through the top left boundary. The other boundaries of the domain are set as transparent. The initial temperature is $1K$ in the dense material and $300K$ elsewhere. A radiative temperature of $T = 5802000K$ is applied on the left side of the transparent region (from $y = 0.5m$ to $y = 1m$).

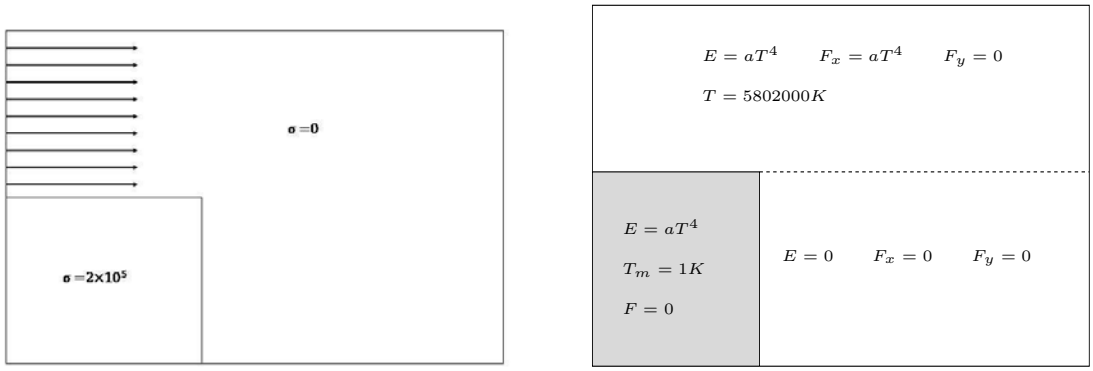

FIGURE 5.3 – Geometry (left) and expected solution (right) for the 2D case.

As for the expected solution it is summed up in Figure 5.3. Indeed, in the upper part the photons are simply translated from the left boundary to the right of the domain. And in the lower part, no photons are entering this area and the solution remains constant against time. The line $y = 0.5$ then is a stationary contact discontinuity for the M_1-system. The dense material does not get any photon either and its temperature remains constant.

Simulations are stopped at time $t = 5\,10^{-8}s$. Figure 5.4 and 5.5 respectively show the radiative and material temperature distributions obtained from calculations with the HLL scheme on one hand and with the HLLC scheme on the other hand. It is obvious that the HLL scheme induces an important numerical diffusion responsible for non-physical penetration of photons in the lower part of the domain. Meanwhile the HLLC scheme is able to deal properly with the discontinuity. There is underlined the major role of the third eigenvalue that was expected to make the difference in 2D configurations.

Looking more in details at the material temperature obtained through the various schemes (see Table 5.1), it appears that the HLLC scheme together with the asymptotic preserving modification and a second order MUSCL-like scheme allow to narrow the expected temperature of $1K$.

Figure 5.6 is a slice made at $x = 1m$ so we can look at the computed radiative temperature across the contact discontinuity. There is outlined the numerical diffusion engendered by the HLL scheme while HLLC is able to approximate the exact

HLL

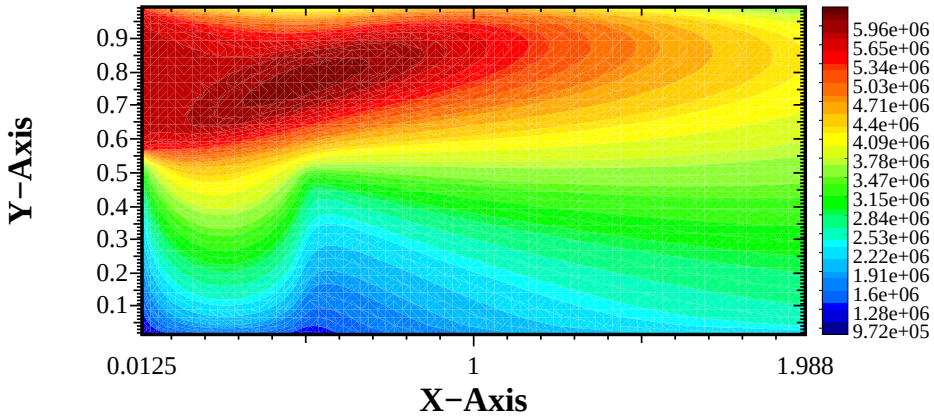

HLLC

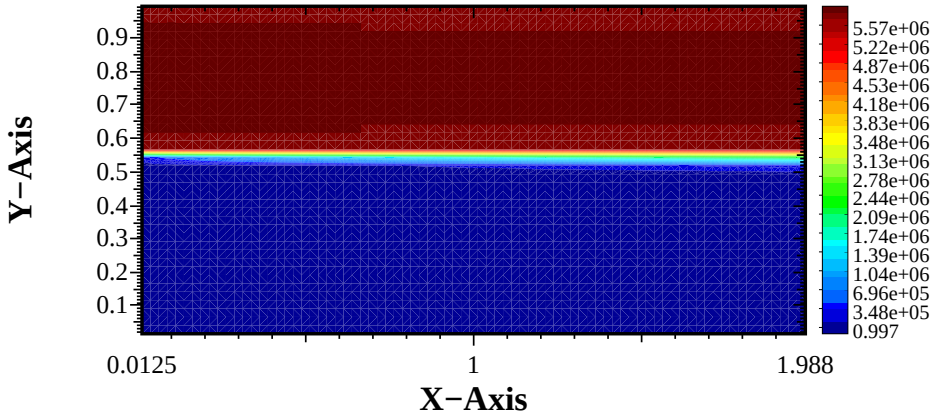

FIGURE 5.4 – Radiative temperature.

Scheme	T matière max HLL	T matière max HLLC	T matière moyenne HLL	T matière moyenne HLLC
b_R, b_L csts	4300000	17000	350000	840
b_R, b_L variables	3700000	170000	290000	11000
b_R, b_L csts + AP	3600000	9000	43000	40
b_R, b_L variables + AP	740000	110000	5200	690
b_R, b_L csts + Minmod	3600000	16000	240000	340
b_R, b_L csts + Minmod + AP	2700000	6400	34000	26
b_R, b_L csts + Superbee + AP	1600000	2400	11000	6.1

TABLE 5.1 – Material temperature with HLL and HLLC schemes.

solution quite closely.

Let us note that a better approximation of the solution is obtained when setting the b_L and b_R values to $\pm c$ than when using the exact eigenvalues of the system. This

HLL

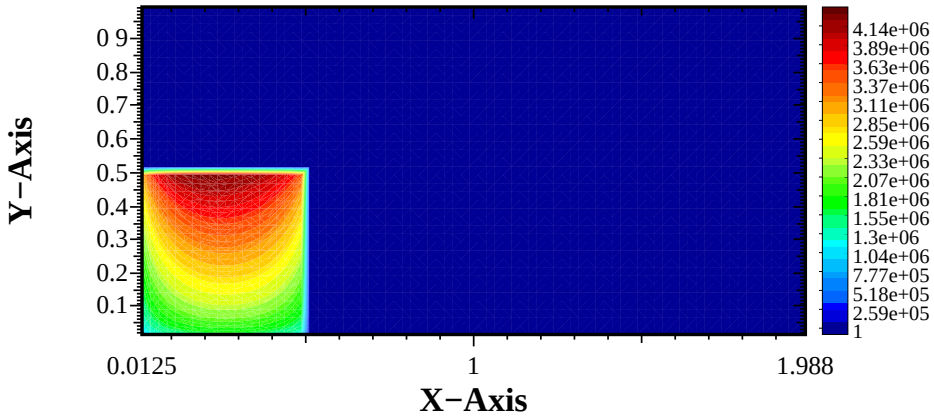

HLLC

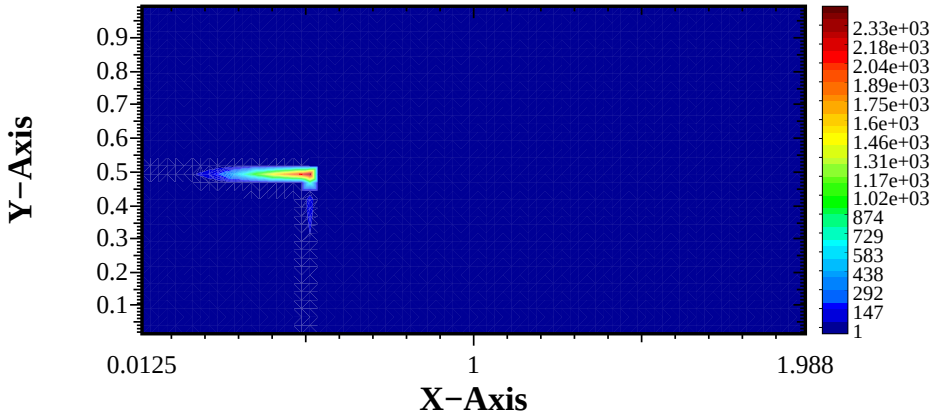

FIGURE 5.5 – Material temperature.

may come from the fact that the waves with velocities b_L and b_R get too close to the contact wave of velocity $c\beta$ and divisions by zero may occur. We therefore choose to use the speed of light as the Riemann problem wavespeeds in all the computations. It indeed does not appear useful to spend time calculating an exact cone. The wider cone (made of $b_L = -c$ and $b_R = +c$) is sufficient as far as capturing the contact wave of the Riemann problem brings a great deal of accuracy to the calculations, even in this very stiff case.

5.4 Elliptic cloud

The second purely radiative test case also allows us to check that the model is able to deal with strong anisotropies, characteristic of the shadow phenomena. We here consider an ellipsoïdal cloud a hundred times thicker than its air-like environment. Other results for this test are shown in [28] and [20].

The domain is a cylinder of length $L = 1cm$ and radius $R = 0.12cm$. The

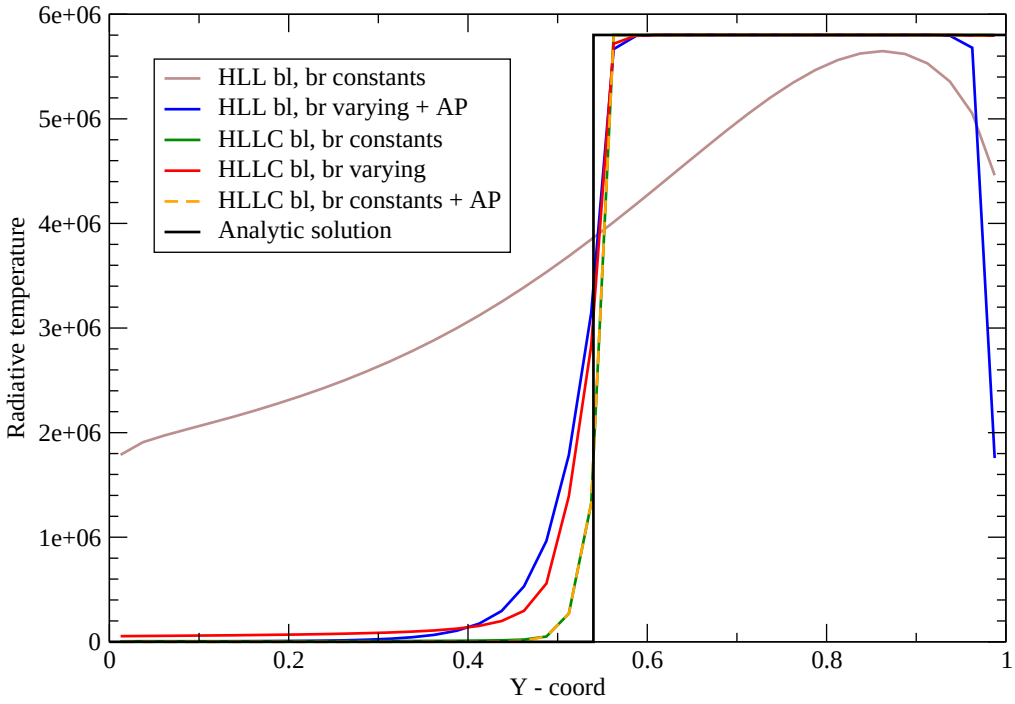

FIGURE 5.6 – Radiative temperature along the y coordinate.

geometry is symmetric and we will only consider one half of it. The cloud center is $(0.5, 0)$ and its dimensions are $(0.1, 0.06)$. The medium is initially at the equilibrium temperature $T_0 = 290K$ and density $\rho_0 = 10^{-3}\, kg\, m^{-3}$. As for the cloud its density is $\rho_1 = 100\rho_0$ and the edge of the cloud is smooth thanks to the relation :

$$\rho(z, r) = \rho_0 + \frac{\rho_1 - \rho_0}{1 + exp\Delta}, \tag{5.1}$$

where

$$\Delta = 10\left[\left(\frac{z - z_c}{z_0}\right)^2 + \left(\frac{r - r_c}{r_0}\right)^2 - 1\right]. \tag{5.2}$$

The opacity in the medium is a function of density and temperature :

$$\sigma = \sigma_0 \left(\frac{T}{T_0}\right)^{-3.5} \left(\frac{\rho}{\rho_0}\right)^2, \tag{5.3}$$

where $\sigma_0 = 10m^{-1}$.

At time $t = 0s$ a uniform temperature $T = 1740K$ is applied on the left boundary of the cylinder. Photons are translated to the right, except that the region behind the cloud is shadowed because of the very short mean free path in the cloud. This shadow must remain stable as long as the light has not gone through the cloud. Figure 5.7 shows the radiative temperature distribution for this test case and for HLL and HLLC calculations. The computations have been performed on a 280×80 cartesian grid. The calculations are stopped at $t = 0.1s$.

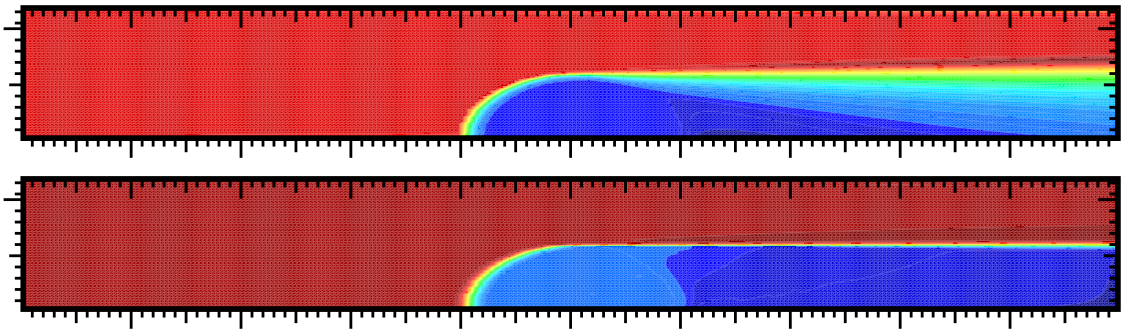

FIGURE 5.7 – Radiative temperature around the cloud with HLL (top) and HLLC (bottom).

The HLL result presented here is a first order calculation with varying b_L and b_R, and the HLLC result is a second order calculation with the Minmod slope limiter and with constant b_L and b_R, i.e. $b_L = -c$ and $b_R = +c$. Both results use the asymptotic preserving modification. The results outline the ability of the HLLC scheme to preserve the radiation anisotropy and to minimise greatly the numerical diffusion.

5.5 Light beam

Another test is this of the light beam entering the domain with an angle different from zero (see [37]). This test is helpful to quantify the numerical diffusion enhanced by the numerical scheme as the incident beam is not aligned with the mesh axis.

In this test the mesh is divided into 128×128 cells and has the dimensions $x = [-1, 1]$ and $y = [-1, 1]$. The temperature in the domain is initially $T = 300K$ and all boundaries are transparent except at $x = -1m$ and in the interval $y = [-0.875, -0.750]$ where a radiative temperature of $1000K$ is applied, the photons incident angle in this interval is 45°. The opacity in the whole medium is $\sigma = 0m^{-1}$, therefore it is not expected any physical diffusion, nor dispersion of the photons.

Figure 5.8 shows radiative energy distributions obtained thanks to computations with HLL on one hand and HLLC on the other hand. Figure 5.9 plots the radiative energy profile at $y = 0m$. We can then compare the beams wideness. Indeed, while the boundary condition sets the incident beam over 8 cells, half-way up the domain the beam extends over 24 cells with the HLL scheme and over 15 cells with the HLLC scheme. The same result as with the HLL scheme was shown in [20].

In order to test the influence of the mesh on the result in figure 5.10 and figure 5.11 are respectively plotted the radiative energy profile at $y = 0$ and the decrease of radiative energy along the beam for both meshes 128×128 and 256×256. The numerical imperfections are obviously less spreaded with the 256×256 mesh, and also the radiative energy appears less attenuated along the beam. Improvements brought by the numerical schemes are here outlined as far as the numerical diffusion is reduced across the discontinuities.

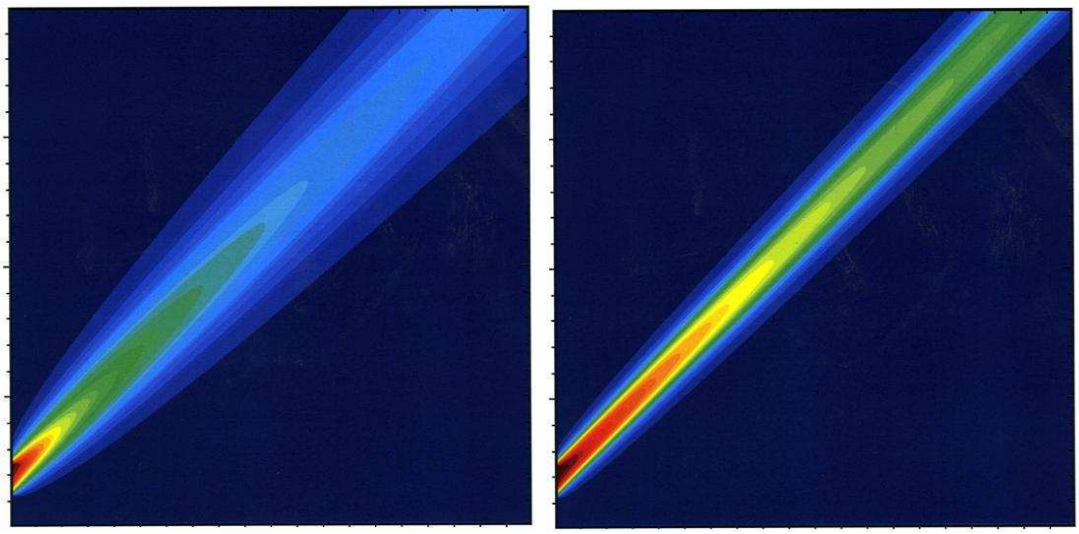

FIGURE 5.8 – Radiative energy of the angled light beam with the HLL scheme (left) and the HLLC scheme (right).

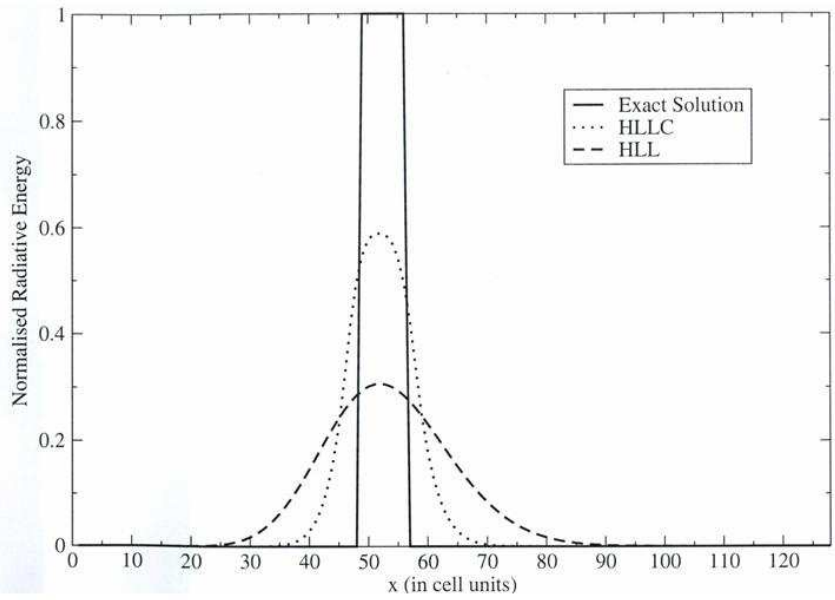

FIGURE 5.9 – Radiative energy profile at $y = 0m$.

5.6 Double light beams

In here we consider two converging light beams angled as in the precedent test. The behaviour of the M_1-model in such a case is shown in Figure 5.12. This test yields the limitations of the M_1-model. In fact, because of the average made over the solid angle when deriving the M_1-model from the radiative transfer equation, photons moving in various directions end up into a single resulting beam. In this test, the two beams should not actually interact. The macroscopic model we have chosen is thus the limiting parameter for the solution to be correct from a physical

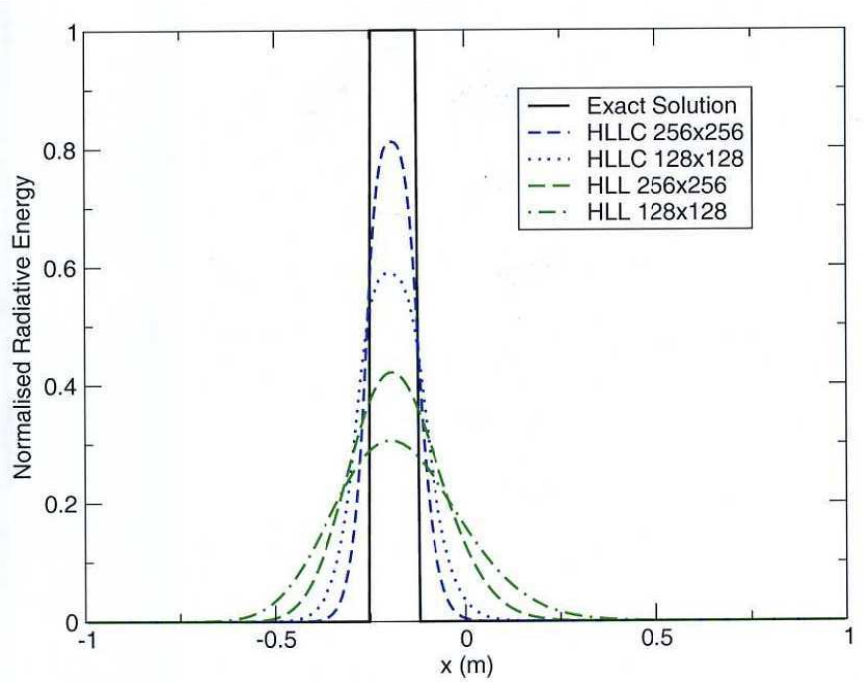

FIGURE 5.10 – Radiative energy profile at $y = 0$ for two meshes.

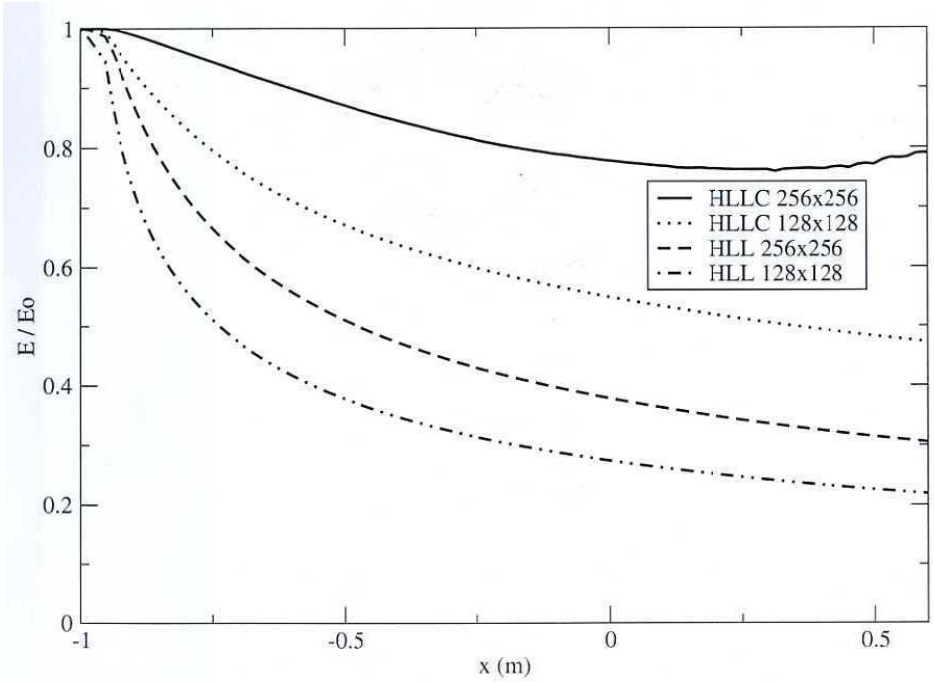

FIGURE 5.11 – Radiative energy decrease along the beam.

point of view.

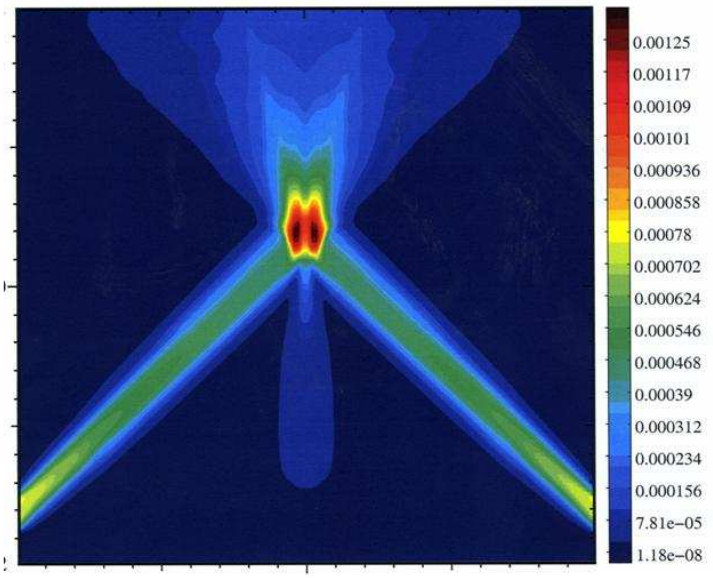

FIGURE 5.12 – The two converging light beams - Radiative energy.

5.7 Curvilinear test

Lastly, in order to test the curvilinear scheme presented in Section 4.3 we get back to the elliptic cloud test case presented in Section 5.4.

In Figure 5.14, the computation results for three different meshes and for the two HLL and HLLC schemes are presented. The meshes used for these computations are a cartesian one, a curvilinear one and a mixed mesh where the area from $y = 0.0006$ to $y = 0.0012$ is cartesian and the bottom area, where the cloud is situated, is meshed curvilinearly. These three meshes are shown in Figure 5.13 where the elliptic cloud has been artificially located. Note that the properties of the cloud area (and the outside of the cloud) have been set through a penalisation method : every cell which center coordinates are located into the ellipse are designated with the cloud properties.

HLL and HLLC computations are second order calculations with the use of the Minmod slope limiter and of the asymptotic preserving scheme. The HLL calculations are performed with variable b_L and b_R and the HLLC calculations make use of $b_R = -b_L = c$. The results are presented in Figure 5.14.

The cartesian and mixed meshes give similar results whereas the curvilinear mesh deteriorates the sharpness of the solution. This could be explained by the fact that, in this particular case, the main propagation direction of the photons is not aligned with the mesh, which involves errors when approximating the solution. Note that the results are still better with the HLLC scheme than with HLL.

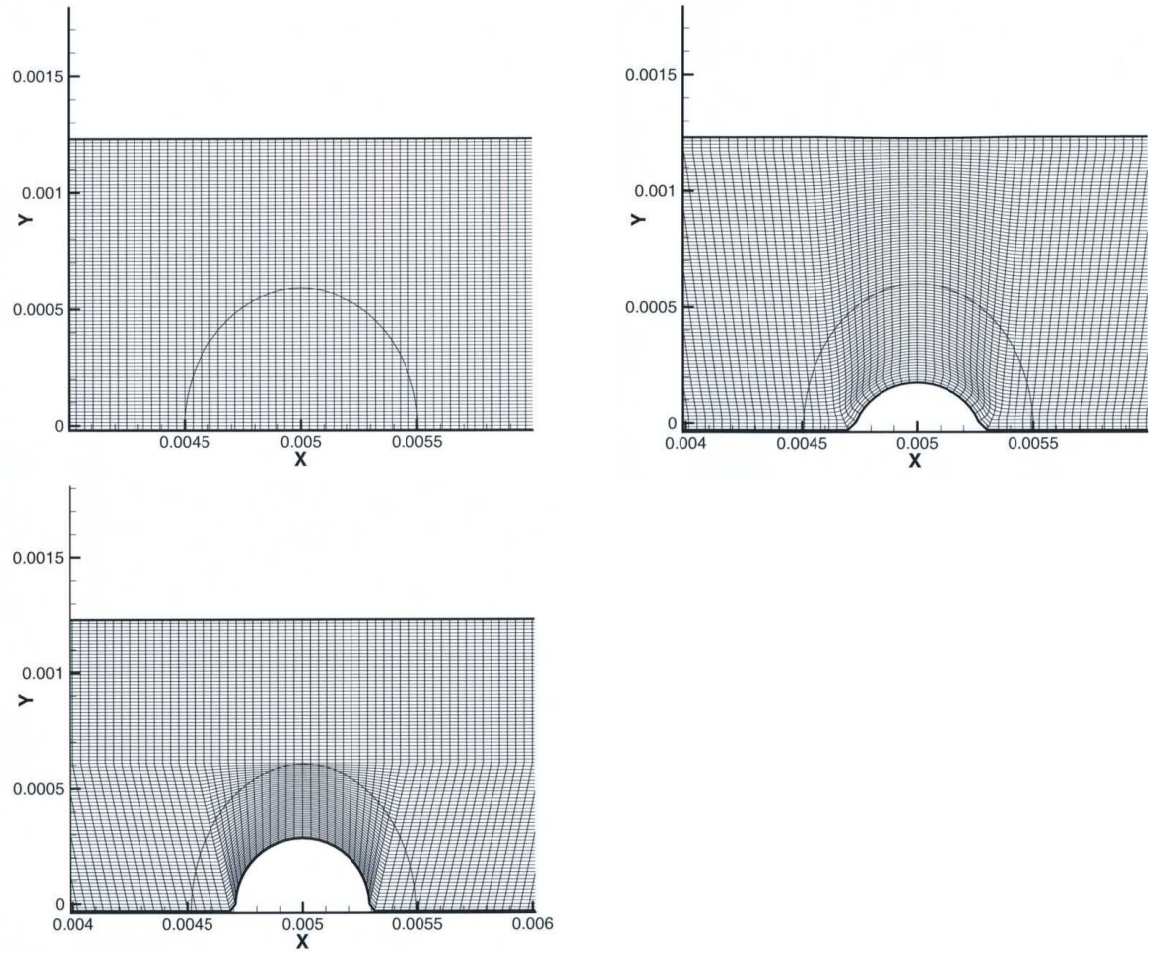

FIGURE 5.13 – Cartesian, curvilinear and mixed meshes.

5.8 Scattering

Let us recall the time-dependant Radiative Transfer Equation taking into account the scattering term :

$$\begin{aligned} \tfrac{1}{c}\partial_t I_\nu(\mathbf{\Omega}) + \mathbf{\Omega}.\nabla I_\nu(\mathbf{\Omega}) = \sigma_\nu^e B_\nu(T) - (\sigma_\nu^a + \sigma_\nu^d) I_\nu(\mathbf{\Omega}) \\ + \tfrac{\sigma_\nu^d}{4\pi} \int_{S^2} p_\nu(\mathbf{\Omega}'.\mathbf{\Omega}) I_\nu(\mathbf{\Omega}') d\mathbf{\Omega}' d\nu, \end{aligned} \tag{5.4}$$

where σ_ν^d, σ_ν^a and σ_ν^e are respectively the mean dispersion, absorption and emission opacities, and $p/4\pi$ is the scattering probability density. When constructing the M_1 moment model, integrations of the RTE are performed over directions and frequencies, therefore one obtain the following system :

$$\begin{cases} \partial_t E + \nabla \cdot \mathbf{F} = c\sigma^a \big(aT^4 - E\big) \\ \partial_t \mathbf{F} + c^2 \nabla \cdot \mathbf{P} = -c\big(\sigma^a + (1 - \tilde{g}_\nu)\sigma^d\big)\mathbf{F} \end{cases} \tag{5.5}$$

where $\tilde{g}_\nu$ is the asymetric parameter of dispersion. In the following test case, the dispersion is considered to be isotropic and this parameter is then equal to 0. The

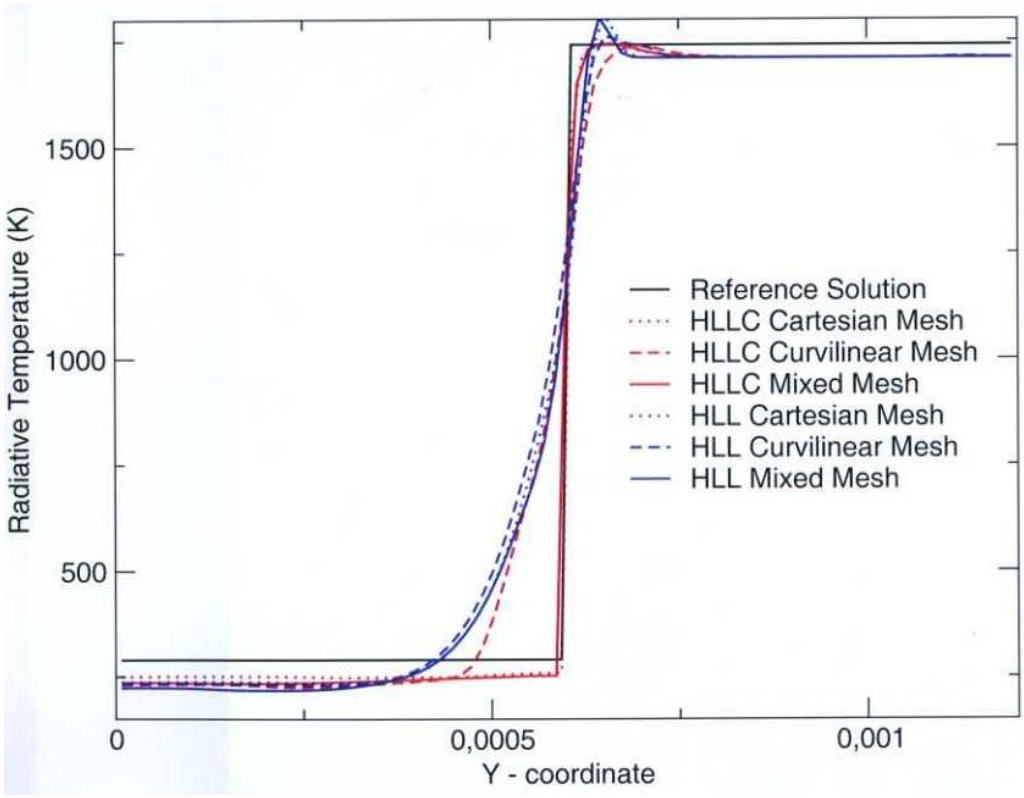

FIGURE 5.14 – Radiative temperature versus the y coordinate with the HLL and HLLC scheme (200 mesh point in the x direction).

equations in (5.5) become :

$$\begin{cases} \partial_t E + \nabla \cdot \mathbf{F} = c\sigma^a \big(aT^4 - E\big) \\ \partial_t \mathbf{F} + c^2 \nabla \cdot \mathbf{P} = -c\big(\sigma^a + \sigma^d\big)\mathbf{F} \end{cases} \tag{5.6}$$

The effects of scattering and the scheme behaviour are observed through a test case from Aydin [4]. This test simulates the propagation of an isotropic beam source into the brain, that is surrounded by a clear layer (the subarachnoid space) and then by the outside tissues. The computed domain is a $100mm \times 100mm$ square meshed by 100 cells in both directions. The ponctual source is centered on the left side of the domain. This configuration is modelled by the geometry in Figure 5.15. Effects of a void-like channel are here highlighted. The channel is $4mm$ thick and $84mm$ long all around. Results are compared with kinetic computations of this test case.

Figure 5.16 shows a map of the radiative energy obtained with computations through a kinetic method. The domain is still discretised into 100 cells in both directions, and the arbitrarily chosen frequencies and directions of propagations vary up to eight different values for a first computation, and up to sixteen different values for the second computation. These kinetic solutions are used as reference solutions for the validation of our macroscopic method based on the moment M_1 model.

Figure 5.17 shows a map of the radiative energy in the domain. This is obtained

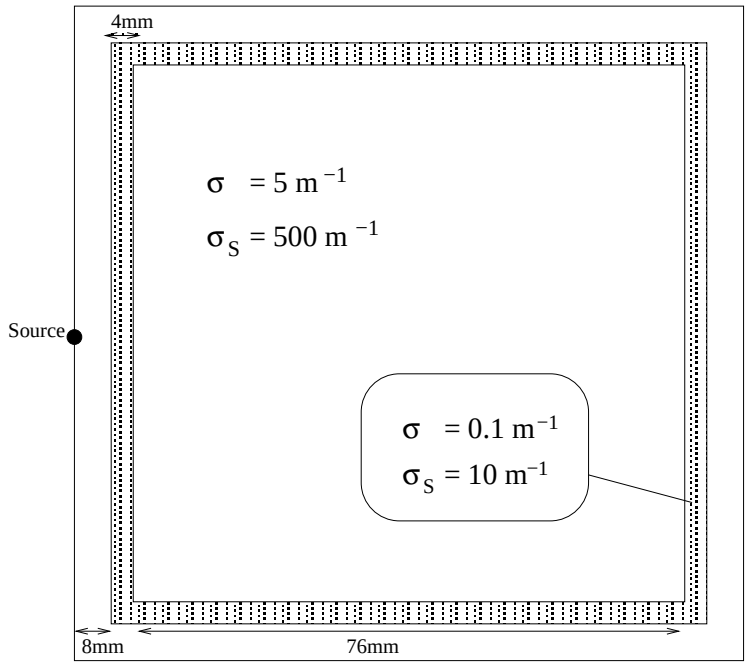

FIGURE 5.15 – Geometry of the channeling problem.

through a second order computation performed with the HLL scheme on the left and the HLLC scheme on the right.

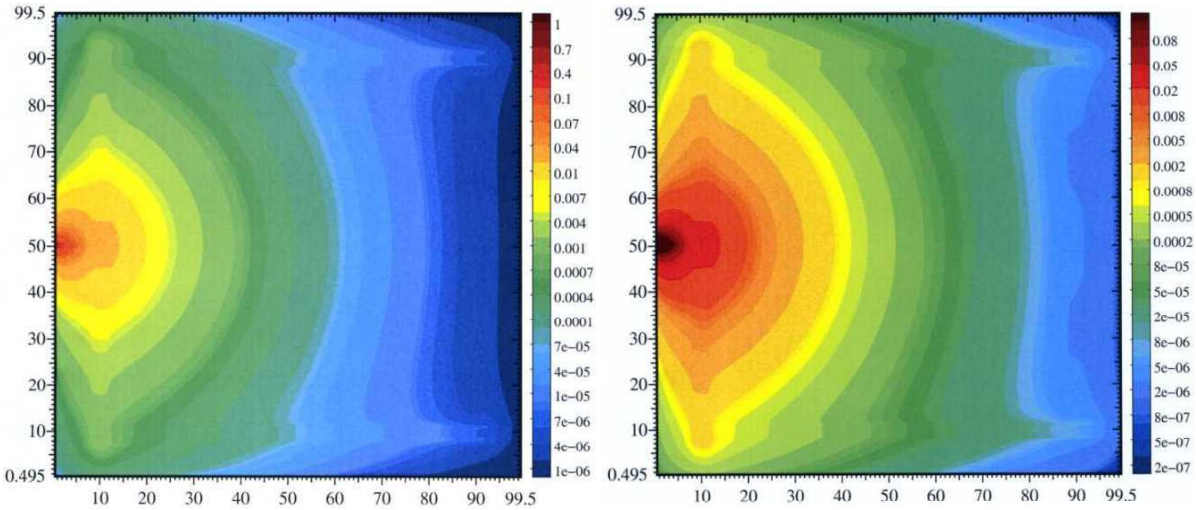

FIGURE 5.16 – Radiative energy - Kinetic computations with 8 (left) and 16 (right) directions of propagation.

A slice is made at the ordinate $y = 50mm$. And the radiative energy along this line is compared with the one obtained through a microscopic resolution of the radiative transfer equation. The number of directions for this kinetic resolution may vary from 8, to 16. Figure 5.18 gathers the results obtained from calculations in a 100×100 mesh, through a kinetic formulation of radiative transfer on one

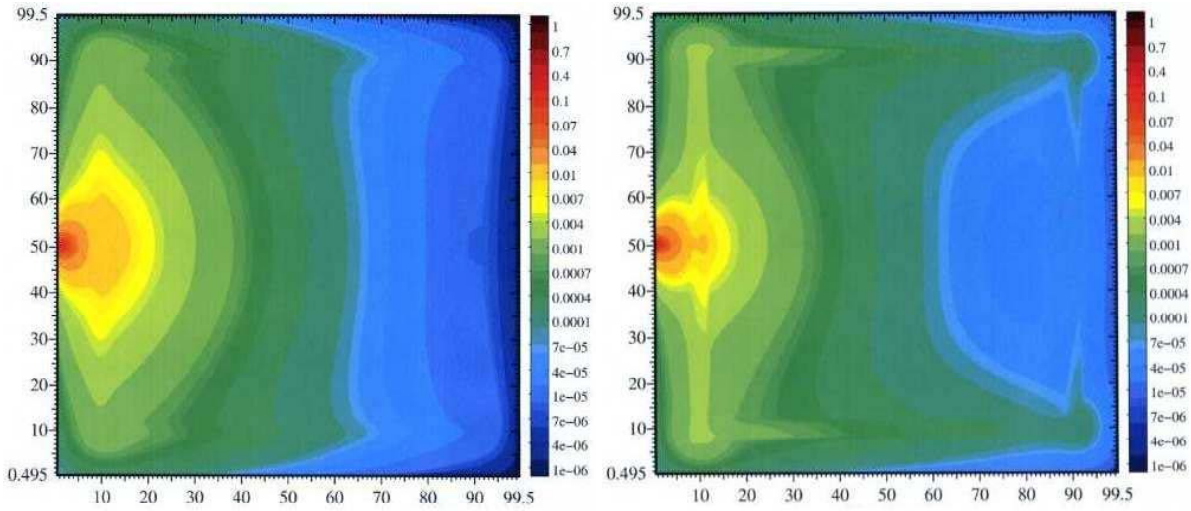

FIGURE 5.17 – Radiative energy - HLL and HLLC schemes, 2nd order MUSCL computations.

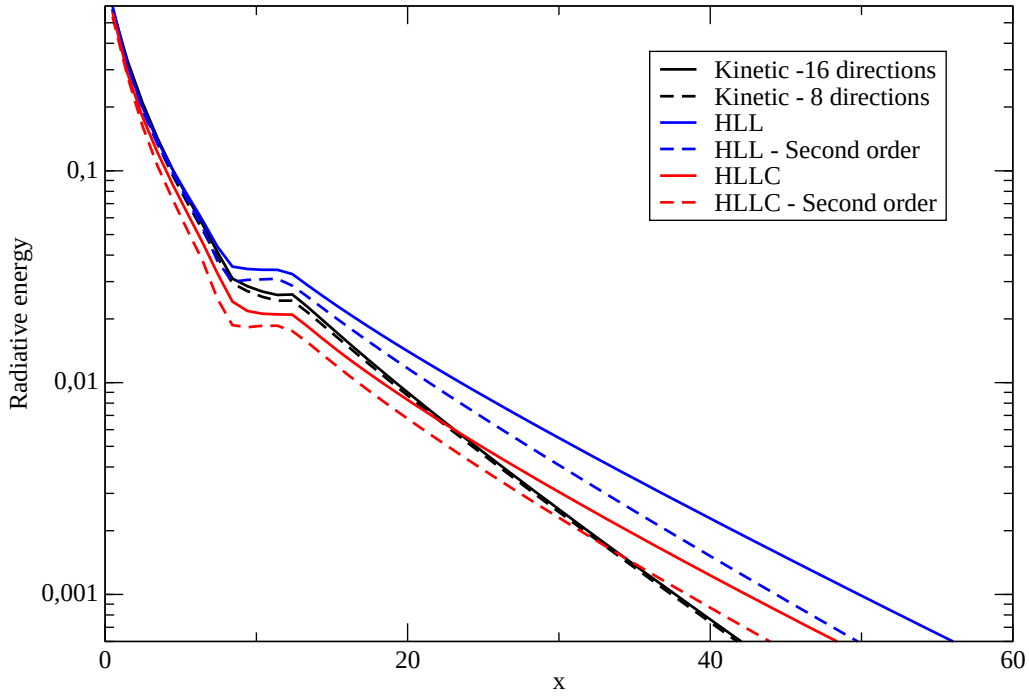

FIGURE 5.18 – Comparison of the radiative energy evolutions across the domain with HLL, HLLC and kinetic computations.

part, and the combined use of the M_1 moments model and the HLL and HLLC Riemann solvers. In this latter case, first and also second order computations have been performed. The logarithmic scale have been chosen in Figure 5.18 so that the slight differences remaining between the various methods can be seen.

In order to involve the role played by the spatial discretisation and to test the mesh convergence, computations have also been performed with a refined mesh

made of 200 cells in both directions. The results are shown in Figure 5.19, where

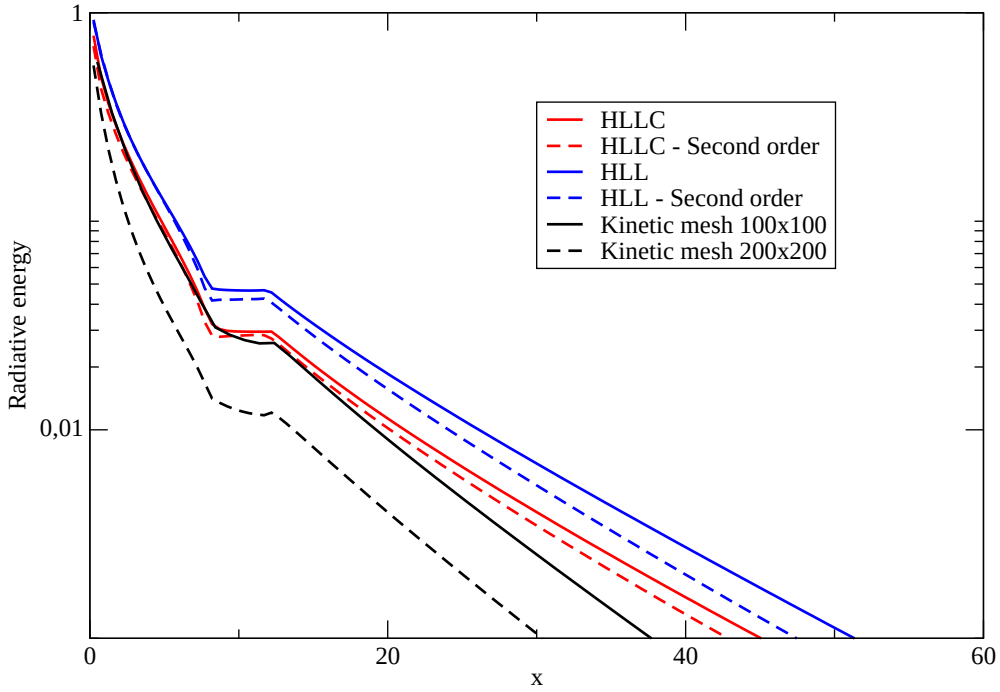

FIGURE 5.19 – Comparison of the radiative energy evolutions with a refined mesh.

a logarithmic scale is again used for the graph ordinate. The kinetic solution that is used as reference solution is obtained over a range of 16 varying directions, and both results with the original and refined mesh are plotted. We observe that the kinetic solution is not really converged either so we can not properly conclude on the improvements brought by the HLLC-type Riemann solver. Although the quality of the results seems to be at least preserved.

5.9 Conclusion

In this chapter, we have performed a number of numerical test cases dedicated to radiative transfer only. These experiments allowed us to specifically test the numerical capabilities of our developed HLLC type scheme, further furbished with an asymptotic preserving correction of the source terms and a second order MUSCL reconstruction.

Particularly, the shadow cone test case contains a very stiff discontinuity that basic Riemann solvers, neglecting the contact wave, are not able to treat properly and enhance an important numerical diffusion. Meanwhile, the present HLLC type scheme provides us with pretty good and accurate simulations of such a configuration. The asymptotic preserving correction of the source terms there appears to be appropriate and efficient.

In addition, through the brain imaging test case, the photons scattering is experienced and drawn against some results obtained through a kinetic approach. The

calculations through the macroscopic approach reveal to be quite satisfactory even if the kinetic approach used as a reference solution does not seem to be fully converged.

The remaining test to carry out is now a coupling of our radiative transfer solution with hydrodynamic phenomena. Having at our disposal an accurate model and a rather cheap method, we are then able to perform such simulations and observe the influence of radiative transfer upon other physical phenomena.

Chapitre 6

Coupling with hydrodynamics

6.1 Introduction

This chapter is devoted to some real life applications to the radiative transfer characterisation. The test case is related to hypersonic flows and the radiative transfer calculation is coupled with hydrodynamic calculations. This application is important as it shows the improvement in terms of accuracy brought to the radiative transfer calculation, and in terms of computation time that can be saved thanks to the newly developed scheme.

This application is a hypersonic flowfield calculation as it deals with an atmopsheric reentry. Atmospheric reentry refers to the movement of human-made or natural objects as they enter the atmosphere of a planet from outer space. It mainly deals with controlled reentry of vehicles which are intended to reach the planetary surface intact, although it may also include minimally controlled cases such as destructive deorbiting of satellites. Typically, this reentry process requires special methods to protect against aerodynamic heating. Indeed, depending on the entry parameters, the effects can be very different. For instance, in the case of a space shuttle coming back to Earth, the conditions are such that radiation plays only a neglectable part compared to the hydrodynamic effects. Meanwhile, in some cases, radiative transfer is determinant. As a matter of fact, the considered planet's atmosphere may be, as Venus', very dense, or as in Titan's case, it may contain chemical species that radiate a lot, and then an important amount of radiation is enhanced. The planet's gravity may also be important and then accelerate the probe or comet coming in. And finally, the velocity of a superorbital object entering the atmosphere can be very high. Indeed, the objective of such high speed reentries is to save fuel by slowing down the vehicle only using the planet's atmosphere as an aerodynamic brake. As an example, for the returning Appolo capsules, two third of the energy was dissipated by the means of radiative transfer effects.

A discussion about the optimum shape of an entry vehicle [35] concludes that a body of large nose radius is favorable in planetary entries as it produces a thick shock layer. This observation was the basic principle on which were built the early space missions vehicles. However, such a shape revealed to bring an unexpected heating related to radiation. As a matter of fact, the temperature in the shock layer being

very high (of the order of $10,000K$), the gas is then fully dissociated, or partially ionised, and it also leads to the production of radiation. This phenomenon, amongst the chemical and aerodynamic phenomena, is thus taken into account in nowadays feasibility studies of atmospheric reentry.

The calculation of a flow around a reentry vehicle involves many parameters that make necessary the use of robust codes. Indeed, considering radiative transfer, we must be able to approximate closely enough the solution of the radiative transfer equation in regimes as different as the diffusion regime in the hot and dense gases of the shock layer, and the transport regime in the cold and transparent regions, as well as the intermediate regimes. The medium opacities are determined from the chemical composition of the gas and the state the species are in, some radiating more or less, and depending on the temperature range the database may not be complete. Moreover, the hydrodynamic behaviour of the flow should not be neglected as it dictates the position and characteristics of the shock and the drag, and can be influenced by the radiative effects.

We have here performed simulations of a hypersonic flow around a planetary entry probe in the case of a Venus like reentry, where the chemistry and the opacities determination are simplified. We focus on the interaction between the radiative effects and the hydrodynamic behaviour.

6.2 The hydrodynamic code and coupling

6.2.1 The Navier-Stokes and $M1$ model coupling

For the following application, to keep the calculation as simple as possible and as we mainly focus on the capabilities of the numerical methods, we consider the grey radiative model written as :

$$\partial_t \mathcal{U} + \partial_x \mathcal{F}(\mathcal{U}) + \partial_y \mathcal{G}(\mathcal{U}) - \partial_x \mathcal{F}_v(\mathcal{U}) - \partial_y \mathcal{G}_v(\mathcal{U}) = \mathcal{S}(\mathcal{U}), \tag{6.1}$$

where, if we consider the perfect gas multi-species Navier-Stokes equations, we have :

$$\mathcal{U} = \begin{pmatrix} (\rho_i)_{i=1..n_s} \\ \rho u \\ \rho v \\ \mathcal{E} \\ E_R \\ F_R^x \\ F_R^y \end{pmatrix}$$

$$\mathcal{F}(\mathcal{U}) = \begin{pmatrix} (\rho_i u)_{i=1..n_s} \\ \rho u^2 + p \\ \rho uv \\ \rho uH \\ F_R^x \\ c^2 D_R^{xx} E_R \\ c^2 D_R^{yx} E_R \end{pmatrix}, \mathcal{G}(\mathcal{U}) = \begin{pmatrix} (\rho_i v)_{i=1..n_s} \\ \rho uv \\ \rho v^2 + p \\ \rho vH \\ F_R^y \\ c^2 D_R^{xy} E_R \\ c^2 D_R^{yy} E_R \end{pmatrix},$$

$$\mathcal{F}_v(\mathcal{U}) = \begin{pmatrix} (\rho\mathcal{D}\partial_x c_i)_{i=1..n_s} \\ \mathcal{T}_{xx} \\ \mathcal{T}_{xy} \\ \mathcal{T}_{xx}u + \mathcal{T}_{xy}v - q_x \\ 0 \\ 0 \\ 0 \end{pmatrix}, \mathcal{G}_v(\mathcal{U}) = \begin{pmatrix} (\rho\mathcal{D}\partial_y c_i)_{i=1..n_s} \\ \mathcal{T}_{yx} \\ \mathcal{T}_{yy} \\ \mathcal{T}_{yx}u + \mathcal{T}_{yy}v - q_y \\ 0 \\ 0 \\ 0 \end{pmatrix},$$

$$\mathcal{S}(\mathcal{U}) = \begin{pmatrix} (\dot{\omega}_i)_{i=1..n_s} \\ -\rho u g_x \\ -\rho v g_y \\ -\rho V.g - c(\sigma^e a T^4 - \sigma^a E_R) \\ (\sigma^e a T^4 - \sigma^a E_R) \\ -(\sigma^f + (1-g)\sigma^s)F_R^x \\ -(\sigma^f + (1-g)\sigma^d)F_R^y \end{pmatrix},$$

and in the case of the M_1 model, the Eddington tensor is written as :

$$D_R = \frac{1-\chi}{2} I_d + \frac{3\chi - 1}{2} \frac{F_R \otimes F_R}{\|F_R\|} \tag{6.2}$$

The scalar $\chi = \chi(f)$ is the Eddington factor. The considered state relation is here a perfect gas relation for every specie ($p_i = \rho_i R_i T$). However, the numerical code we use here is able to consider various state relations. In System (6.1), we have neglected some terms. As for the radiative pressure, it is assumed to be small compared to the total pressure. We suppose that emission, absorption and scattering are the only interaction mecanisms occuring between the photons and the matter. Moreover, the scattering distribution function is assumed to depend only on the angle Ω.

An interesting property of System (6.1) is that the first order term ($\partial_t \mathcal{U} + \partial_x \mathcal{F}(\mathcal{U}) + \partial_y \mathcal{G}(\mathcal{U}) = 0$) is hyperbolic. Indeed, in 1D, the Jacobian matrix is :

$$J = \begin{pmatrix} u & \rho & 0 & 0 & 0 \\ u^2 + \partial_\rho p & 2\rho u + \partial_u p & \partial_{\mathcal{E}} p & 0 & 0 \\ uH + \rho u \partial_\rho H & \rho H + \rho u \partial_u H & \rho u \partial_{\mathcal{E}} H & 0 & 0 \\ 0 & 0 & 0 & 0 & 1 \\ 0 & 0 & 0 & c^2(\chi - \chi' f) & c\chi' \end{pmatrix}. \tag{6.3}$$

This matrix J is diagonal in blocks. The first block (3×3) is the jacobian of the Euler equations. And the second block (2×2) is the jacobian of the M_1 model. This means that hydrodynamic and radiative phenomena are only coupled through the source terms of order 0. The system eigenvalues are then $u + a$, u, $u - a$, $\lambda - +$ and λ_- where a is the speed of sound and

$$\lambda_\pm = \pm \frac{c[\mp 3f\sqrt{4 - 3f^2} + 2\sqrt{3}\sqrt{(-4 + 3f^2)(3f^2 + 2\sqrt{4 - 3f^2} - 5)}]}{3(-4 + 3f^2)}$$

are the eigenvalues of the M_1 system [17].

This non-coupled property of the hyperbolic system makes easier the numerical approximation and the introduction of radiation into a hypersonic hydrodynamic procedure. However, for specific applications, it is possible to realise a strong coupling between hydrodynamic and radiation. This coupling is taken into account through the source terms.

6.2.2 Numerical scheme

The numerical methods presented in this document have been introduced in the ARES code from the CEA-CESTA. ARES is a two dimensional aerodynamic code that contains various types of flow models such as Euler, Navier-Stokes, and with turbulence models, simple chemistry or non-equilibrium chemistry.

Spatial discretisation

Let us consider multi-block structured meshes. In this case, the discrete unknowns vector is defined by :

$$\mathcal{U}(i+(l-1)n_{fr}+(m-1)l_{max}n_{fr})_{i=1..n_{fr},l=1..l_{max},m=1..m_{max}}. \tag{6.4}$$

The hyperbolic numerical fluxes calculation may be done through :

- a Roe scheme for the hydrodynamic.
- an HLL or HLLC scheme, or a kinetic scheme for radiative transfer (see [3], [17], [45]).

The second order terms are treated through centered schemes.

Time implicit scheme

With the above defined spatial discretisation, the scheme can be written :

$$\partial_t \mathcal{U}_{l,m}(t) + \frac{\mathcal{F}_{l+\frac{1}{2},m}(t) - \mathcal{F}_{l-\frac{1}{2},m}(t)}{\Delta x_{l,m}} + \frac{\mathcal{G}_{l,m+\frac{1}{2}}(t) - \mathcal{G}_{l,m-\frac{1}{2}}(t)}{\Delta y_{l,m}} = S_{l,m}(t), \tag{6.5}$$

that we also note :

$$\partial_t \mathcal{U}_{l,m}(t) = \Theta_{l,m}(\mathcal{U}(t)). \tag{6.6}$$

In terms of time discretisation, we use the following schemes :

- Explicit scheme :

$$\mathcal{U}_{l,m}^{n+1} - \mathcal{U}_{l,m} - \Delta t \Theta(\mathcal{U}^n) = 0. \tag{6.7}$$

- Implicit scheme :
  - Euler implicit (first order) :

$$\mathcal{U}_{l,m}^{n+1} - \mathcal{U}_{l,m} - \Delta t \Theta(\mathcal{U}^{n+1}) = 0. \tag{6.8}$$

  - Gear method (second order) :

$$3\mathcal{U}_{l,m}^{n+1} - 4\mathcal{U}_{l,m} + \mathcal{U}_{l,m}^{n-1} - 2\Delta t \Theta(\mathcal{U}^{n+1}) = 0. \tag{6.9}$$

GMRes and JFNK methods

All the precedent schemes can be written in the form $\Phi(\mathcal{U}^{n+1}) = 0$. In order to determine $\mathcal{U}^{n+1}$, we have to solve this equation. With this aim, we use the Newton method. And, in this case, if we set $A(\mathcal{U}) = \Phi'(\mathcal{U})$, we have to iterate the solution of the linear system :

$$A(\mathcal{U}^k)(\mathcal{U}^{k+1} - \mathcal{U}^k) = -\Phi(\mathcal{U}^k). \tag{6.10}$$

In order to solve these systems, we choose to use a Krylov type method with the GMRes extension (Generalized Minimal Residual). Within this classical approach, we are led to build and store the jacobian matrix A, which size is usually quite important. However, we are to skip this difficulty by using Jacobian-Free method, i.e. a method where the calculation and storage of the jacobian matrix is not useful. Finally, as we often like to use large timesteps, which deteriorates the jacobian matrix conditionning, we use pre-conditioning schemes that accelerate the GMRes convergence.

6.3 The Pioneer Venus entry

In this numerical experiment, we look at an object with the dimensions of the Pioneer Venus bus portion of the spacecraft that reached Venus in December 1978. It is a $2.5m$ diameter vehicle weighing $250kg$. The trajectory point considered in this simulation is located at an altitude of about $80km$, and the temperature at this point is of $142K$ and the pressure is $300Pa$. Atmospheric reentries in Venus are to be known to be quite difficult because of the thickness of its atmosphere (about 90 times thicker than the Earth atmosphere).

For the simulations performed here, we solely look at the forepart of the body. The chemical composition of the venusian atmosphere is assumed to be made of 100% of CO_2, we neglect the presence of N_2, and then, the species in presence in the shock layer will be CO_2, CO, C, C_2 and O_2. The initial opacities are also considered constant over the computed domain and equal to $5000m^{-1}$.

It has already been pointed out in [46] that the flow is modified by the radiative effects. The shock layer thickness is smaller in the case of a coupled calculation, and also the temperatures are smaller in the coupled case than in the calculation without radiation. And the conclusion is that a large amount of energy is dissipated thanks to the radiative effects and that this energy is transfered towards the cold regions of the outer environment of the probe.

Here, we focus on the numerical accuracy improvements realised with the development of an accurate approximate Riemann solver that is the HLLC-like solver described in the precedent chapters. Then for our study, we reduce the comparison to the HLL and HLLC approximate Riemann solvers at our disposal for the solution approximation of the radiative transfer equation. The calculation domain is regularly divided into 40 cells in the x direction and 15 cells in the y direction (see the left mesh in Figure 6.2). The temperatures obtained with such flow conditions are

plotted in Figure 6.1. We can notice that the shock layer thickness is even more reduced through the use of the HLLC scheme than with the HLL scheme (compared to a non coupled simulation as shown in [46]).

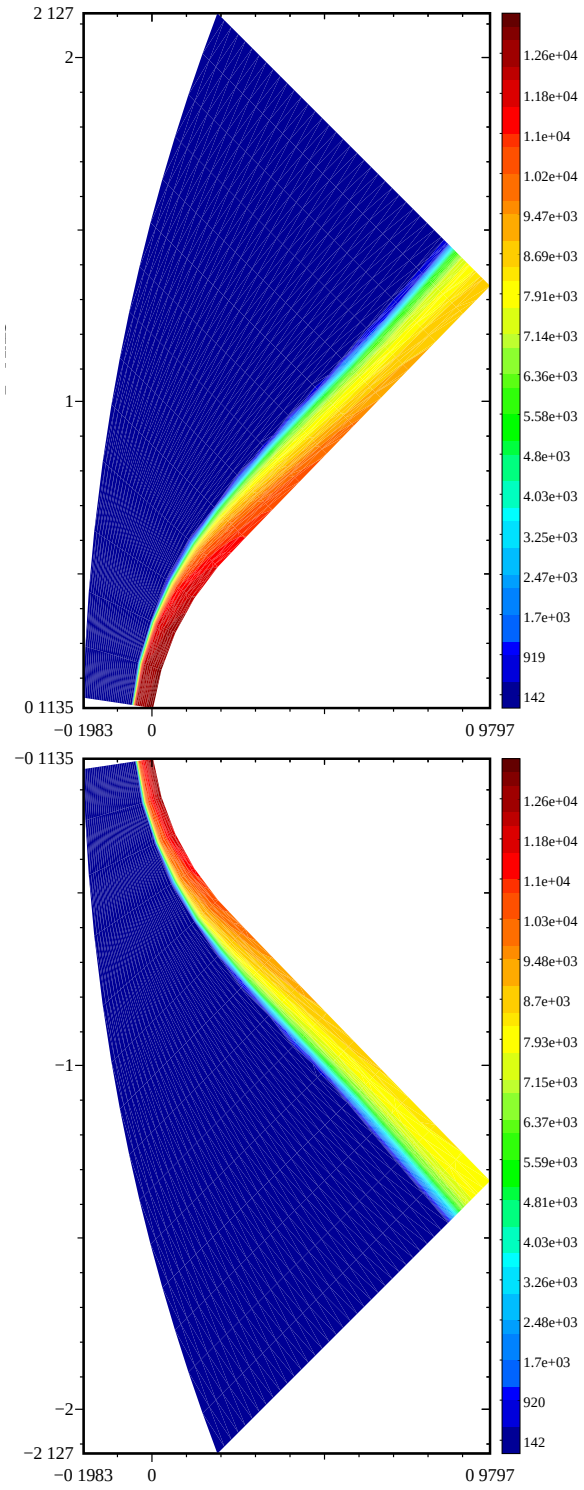

FIGURE 6.1 – Temperatures obtained the HLL (top) and HLLC (bottom) schemes.

Next, an additional test we make is to refine the mesh in the boundary layer close to the body, and we observe how does the solution converge with a better adapted mesh to the phenomena. The first mesh, which is basically regular over the whole domain, and the second and refined mesh are sketched in Figure 6.2. Let us precise that the refined mesh is still divided into 40 cells in the x direction and 15 cells in the y direction, as the original mesh.

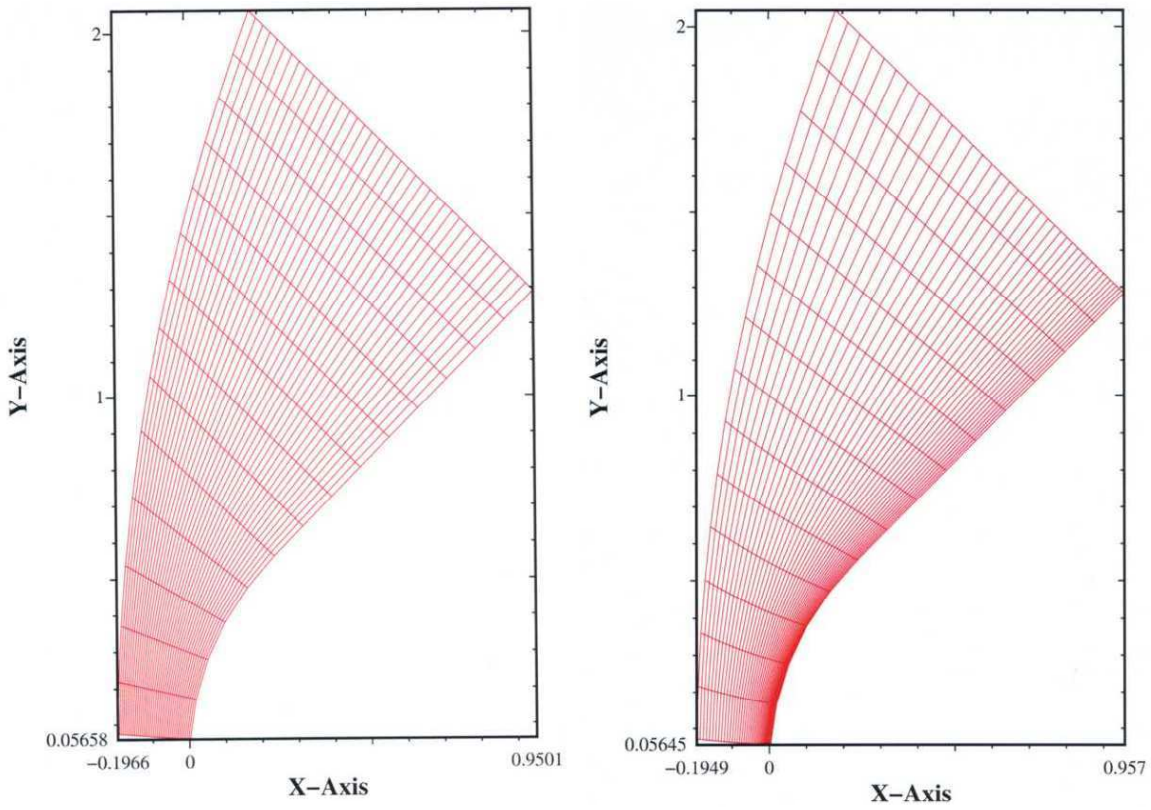

FIGURE 6.2 – Regular (left) and refined (right) meshes.

From the observations of the obtained temperatures shown in Figure 6.3 and the anisotropy factor in Figure 6.4, we have that the HLLC solution obtained with the regular mesh converges with both HLL and HLLC solutions obtained with the refined mesh. We thus confirm the gain in accuracy we have made when developing an HLLC like Riemann solver. Moreover, from a computation cost point of view, performing these tests on one processor (type : Itanium II - 1.6 GHz), we outline that it is approximately two times longer to obtain a converged solution with the refined mesh than with the regular mesh. It is therefore cheaper to realise the needed calculations over a regular mesh, and it is accurate enough when using the HLLC approximate Riemann solver.

The influence of radiative transfer is thus here outlined, even at such a high altitude where we picked our trajectory point. Deeper into the atmosphere, it may be even more visible. However, more complex chemistry and turbulence calculations would be needed.

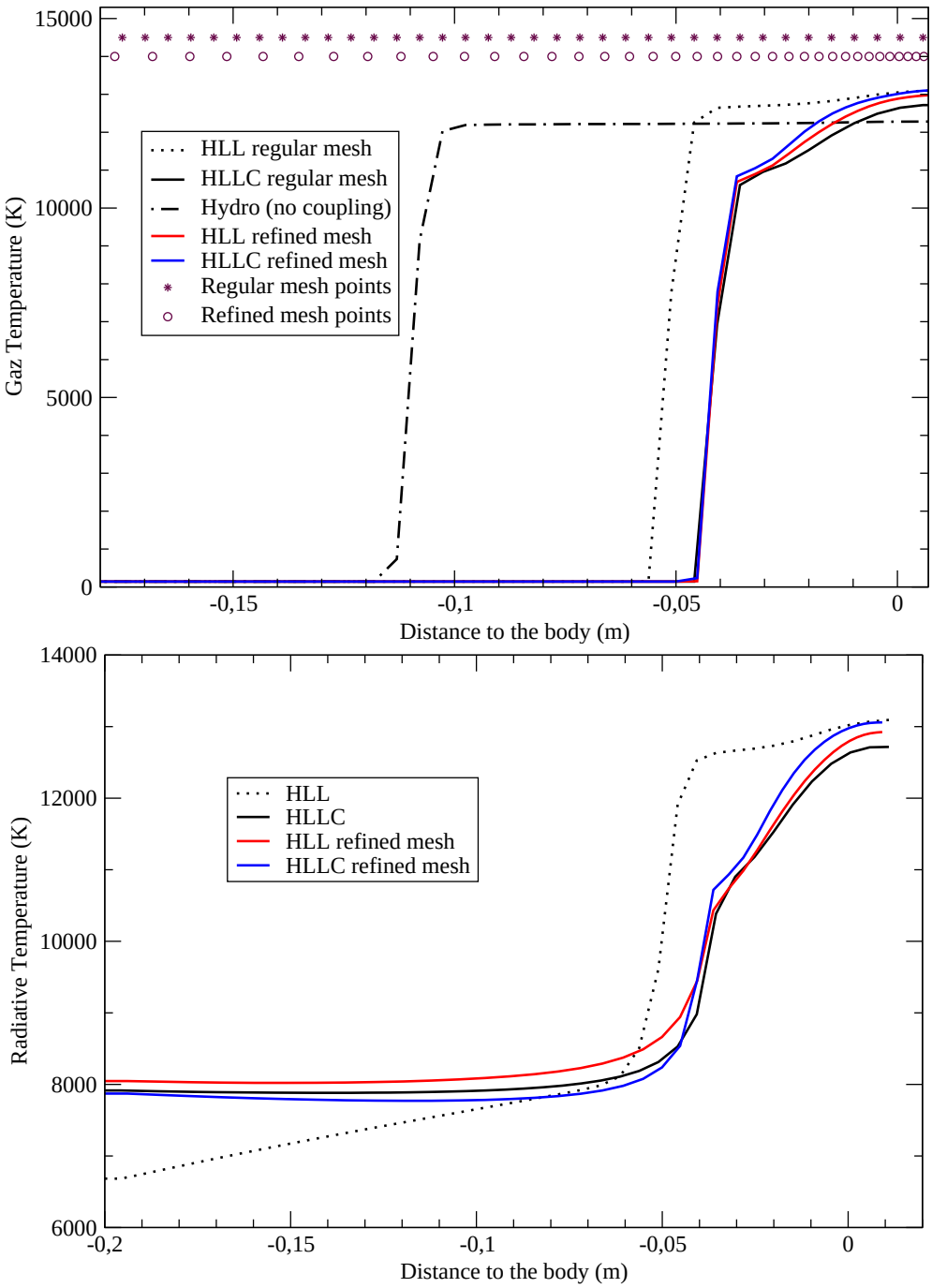

FIGURE 6.3 – Gaz temperature (top) and radiative temperature (bottom) - Mesh convergence.

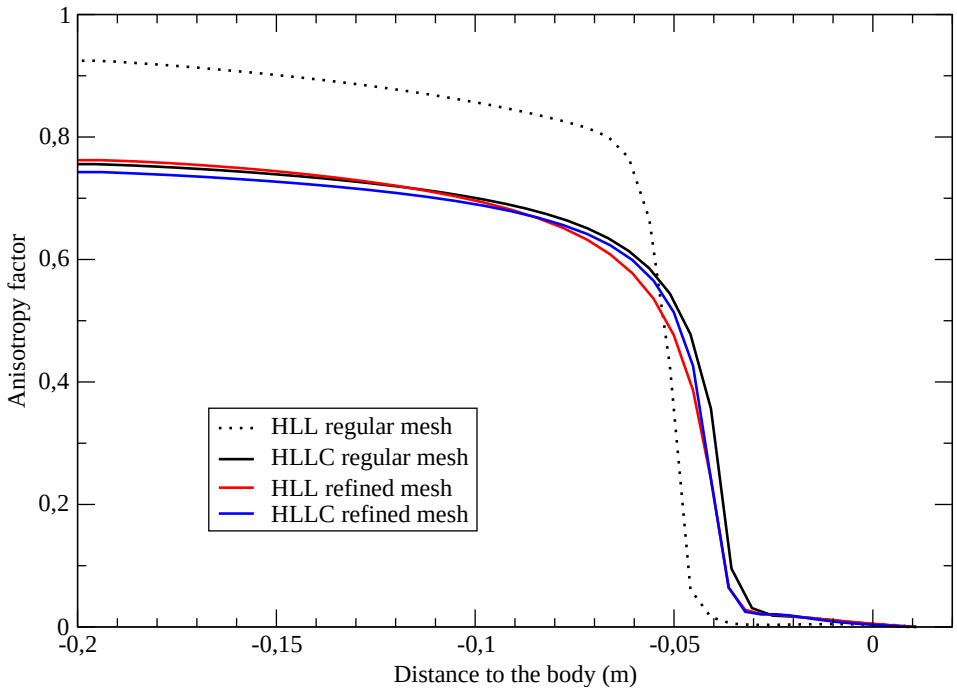

FIGURE 6.4 – Anisotropy factor - Mesh convergence.

Conclusion

The present document reports the work realised on the particular phenomenon that is radiative transfer and for purposes such as atmospheric reentries simulations. The objective was to allow us to take radiative transfer into account providing with an accurate approximation of the solution and still with an acceptable computation cost. This work is based on the M_1 macroscopic model for radiative transfer, resulting from an integration of the radiative transfer equation over the directions and frequencies. This model has the advantage to preserve some essential physical properties, such as the radiative energy positivity, the radiative flux limitation, and it is built on the entropy minimum principle. This model is appropriate for our needs as it allows simulations of the limit propagation regime occuring in opaque mediums on one hand, and in transparent mediums on the other hand.

Finite volume techniques are considered for the expected simulations, and particularly, accurate approximate Riemann solvers were our main topic. The study of a relaxation scheme has permitted to establish the appropriate linearisations useful for writing an accurate numerical tool. On the basis of the classical HLL approximate Riemann solver, known for its robustness but rather diffusive behaviour, we have built an HLLC type Riemann solver. This solver is able to capture the stationary contact wave and thus brings additional accuracy to the solution approximation. Additionaly, this scheme is proved to be robust. The robustness is verified through various numerical experiments, and the precision improvement is well exhibited with these numerical test cases, especially with the very stiff case that is the shadow cone test case.

In order to fulfill the asymptotic regimes requirements, we have included an asymptotic preserving scheme dealing properly with the source terms of our hyperbolic system and respecting the limit regimes behaviours. Along with the use of a second order MUSCL-like scheme, the whole procedure is checked to remain robust, that is to say, to preserve the radiative energy positivity and the radiative flux limitation. The whole procedure containing the developed HLLC Riemann solver reveals to be rather effective as far as, particularly when performing coupled calculations with hydrodynamic problems, it allows an obvious gain in accuracy, and thus a significant saving in terms of computation cost.

The effects of scattering have also been investigated. Isotropic dispersion have been compared with a kinetic approach of the phenomenon and the results reveal to be satisfactory.

The next step, in order to improve the hypersonic flow simulations, would be to consider the appropriate opacities that are usually calculated through databases spe-

cifying the radiative properties for each chemical species in presence in the medium. The M_1 model, resulting from an integration of the radiative transfer equation over the frequencies, considers a unique opacity data over the whole spectrum. However, this is not accurate when dealing with reentry problems where the radiative gas is in spectral non-equilibrium. Multigroup models, such as the one presented in [44] and [46], must then be used to compensate this need.

An other aspect to deal with is the direction non-equilibrium. Indeed, as for the spectral non-equilibrium, the M_1 model, from its construction, does not take this aspect into account.

Finally, it could be envisaged to couple a macroscopic treatment of radiative transfer such as realised in this work, with a kinetic model in order to compensate for the disadvantages of the M_1 model in the areas where strong non-equilibriums occur. The calculations of these latter regions would be taken over by the more precise but expansive method, while the equilibrium regions are calculated through the M_1 model for a faster treatment.

Bibliographie

[1] J. D. Anderson, *Hypersonic and High Temperature Gas Dynamics*, McGraw-Hill Edition, 1989.

[2] D. Aregba-Driollet and R. Natalini, *Convergence of relaxation schemes for conservation laws*, Appl. Anal., 61, 163-196, 1996.

[3] E. Audit, P. Charrier, J.P. Chièze and B. Dubroca, *A radiation-hydrodynamics scheme valid from the transport to the diffusion limit*, astro-ph database article, no 0206281, 2002.

[4] E. D. Aydin, *Three-Dimensional Photon Migration Through Voidlike Regions and Channels*, Applied Optics, Vol.46, No.34, December 2007.

[5] M. Ben-Artzi and J. Falcovitz, *A Second Order Godunov-Type Scheme for Compressible Fluid Dynamics*, J. Comput. Phys., 55 :1-32, 1984.

[6] C. Berthon, P. Charrier, B. Dubroca, *An HLLC Scheme to Solve the M_1 Model of Radiative Transfer in Two Space Dimensions*, J. Sci. Comput., 31, no. 3, pp 347-389, 2007.

[7] C. Berthon, J. Dubois, R. Turpault, *Numerical Approximation of the M_1 Model*, Mathematical Methods and Numerical Models for Radiative Transfer, SMF, Nice 2007.

[8] C. Berthon and R. Turpault, *Asymptotic Preserving HLL Schemes*, 2009.

[9] F. Bouchut, *Nonlinear Stability of Finite Volume Methods for Hyperbolic Conservation Laws*, Birkhaiuser Verlag, 2004.

[10] C. Buet, S. Cordier, *Asymptotic Preserving Scheme and Numerical Methods for Radiative Hydrodynamic Models*, C.R.Acad.Sci. Paris, Tome 338 (2004), Série I, 951-956.

[11] C. Buet and B. Després, *Asymptotic analysis of fluid models for the coupling of radiation and hydrodynamics*, J. Quant. Spectrosc. Radiat. Transfer, 85 (2004), 3-4, 385–418.

[12] C. Buet and B. Després, *Asymptotic preserving and positive schemes for radiation hydrodynamics*, Journal of Computational Physics, Volume 215, Issue 2, 1 July 2006, pp 717-740.

[13] C. Chalons and J.-F. Coulombel, *Relaxation Approximation of the Euler Equations*, J. Math. Anal. Appl., vol 348, no. 2, pp872-893, 2008.

[14] P. Colella and P.R. Woodward, *The Piecewise Parabolic Method (PPM) for gas-dynamical simulations*, J. Comput. Phys., vol 54, pp174-201, 1984.

[15] F. Coquel and B. Perthame, *Relaxation of Energy and Approximate Riemann Solvers for General Pressure Laws in Fluid Dynamics*, SIAM J. Numer. Anal., 35, 6, 2223-2249.

[16] B. Dubroca, G. Duffa, *Modélisation Numérique du Rayonnement et Applications*, Cours de 3ème année MATMECA, January 2005.

[17] B. Dubroca, J.-L. Feugeas, *Hiérarchie de Modèles aux Moments pour le Transfert Radiatif*, C.R.Acad.Sci. Paris, tome 329, 1999, Serie I, pp 915-920.

[18] C.A.J. Fletcher, *Computational Techniques for Fluid Dynamics - Specific Techniques for Different Flow Categories*, Springer-Verlag, Vol.2, 1988.

[19] E. Godlewski, P.-A. Raviart, *Numerical Approximation of Hyperbolic Systems of Conservation Laws*, Springer-Verlag New York Inc. 1996.

[20] M. González, *Contribution à l'étude numérique de l'hydrodynamique radiative : des expériences de chocs radiatifs aux jets astrophysiques*, PhD Report Université Paris-Sud XI, Oct. 2006.

[21] L. Gosse, *A well-balanced flux-vector splitting scheme designed for hyperbolic systems of conservation laws with source terms*, Comput. Math. Appl., 39, 135-159, 2000.

[22] L. Gosse and G. Toscani, *An Asymptotic Preserving Well-Balanced Scheme for the Hyperbolic Heat Equations*, C. R. Acad. Sci. Paris, Ser. I 334, 2001.

[23] S. Gottlieb, D. Gottlieb, C.W. Shu, *Recovering High-Order Accuracy in WENO Computations of Steady-State Hyperbolic Systems*, J. of Scientific Computing, vol 28, no.2/3, 2006.

[24] H. Grad, *On Kinetic Theory of the Rarefied Gases*, Comm. Pure and Appl. Math., II :331-407, 1949.

[25] J.M. Greenberg, A.-Y. Leroux, *A Well-Balanced Scheme for the Numerical Processing of Source Terms in Hyperbolic Equations*, SIAM J. Numer. Anal., 33 (1996), pp 1-16.

[26] A. Harten, *ENO Schemes with Subcell Resolution*, J. Comput. Phys., 83 :148-184, 1989.

[27] A. Harten, P.D. Lax, B. van Leer, *On Upstream Differencing and Godunov-Type Schemes for Hyperbolic Conservation Laws*, SIAM Review, Vol.25, No.1, January 1983.

[28] J.C. Hayes & M.L. Norman, *Beyond Flux-Limited Diffusion : Parallel Algorithms for Multidimensional Radiation Hydrodynamics*, ApJS, 147 :197-220, July 2003.

[29] S. Jin and Z. Xin, *The Relaxation Scheme for Systems of Conservation Laws*, Comm. Pure Appl. Math., 45, 235-276, 1995.

[30] R.J. Leveque, *Numerical methods for conservation laws*, Birkhäuser, Basel, 1992.

[31] R.J. Leveque and M. Pelanti, *A Class of Approximate Riemann Solvers and Their Relation to Relaxation Schemes*, J. Comput. Phys., 172, 572-591, 2001.

[32] D. Levermore, *Moments Closure Hierarchies for Kinetic Theories*, J. Stat. Phys., 83, 1996.

[33] D. Levermore, *Relating Eddington Factors to Flux Limiters*, J. Quant. Spectrosc. Radiat. Transfer, Vol.31, 1984.

[34] D. Mihalas, G. W. Mihalas, *Foundation of Radiation Hydrodynamics*, Oxford University Press, 1984.

[35] C. Park, *Overview of radiation problems in planetary entries*, Procedings of the International Workshop on Radiation of High Temperature Gases in Atmospheric Entry, ESA SP-583, May 2005.

[36] G.C. Pomraning, *The Equations of Radiation Hydrodynamics*, Sciences Application, 1973.

[37] S. Richling, E. Meinköhn, N. Kryzhevoi and G. Kanschat, *Radiative Transfer with Finite Elements. I. Basic method and tests*, A&A, 452 :907-920, June 2001.

[38] J.-F. Ripoll, *Modélisation Mathématique et Numérique du Couplage Hydrodynamique-Transfert Radiatif. Application aux Feux*, PhD Report, January 2001.

[39] P.L. Roe, *Some Contributions to the Modelling of Discontinuous Flows*, Proceedings of the SIAM/AMS Seminar, San Diego, 1983.

[40] A.J. Smith, A. Wood, J. Dubois, M. Fertig, B. Pfeiffer, *Plasma Radiation Database PARADE V2.2*, Technical Report TR28/96, Fluid Gravity Engineering Ltd, October 2006.

[41] E.F. Toro, *Riemann Solvers and Numerical Methods for Fluid Dynamics - A Practical Introduction*, Springer-Verlag Berlin Heidelberg, 1999.

[42] E.F. Toro and V.A. Titarev, *Solution of the Generalised Riemann Problem for Advection-Reaction Equations*, Proc. Roy. Soc. London, 458 :128-143, 2002.

[43] R. Turpault, *Construction d'un modèle M1-multigroupe pour les équations du transfert radiatif*, C. R. Acad. Sci. Paris, Ser. I, 334 (2002) 1-6.

[44] R. Turpault, *A Multigroup M1 Model for Radiation Hydrodynamics and Applications*, 23rd internationnal symposium on rarefied gas dynamics proceedings editors A. D. Ketsdever and E. P. Muntz, American Institute of Physics.

[45] R. Turpault, *Modèles cinétiques et modèles aux moments multigroupes pour le transfert radiatif*, rapport LRC-02.06, 2002.

[46] R. Turpault, *Modélisation, Approximation Numérique et Applications du Transfert Radiatif en Déséquilibre Spectral Couplé avec l'Hydrodynamique*, PhD Report, September 2003.

[47] B. Van Leer, *Towards the Ultimate Conservative Difference Scheme - A Second Order Sequel to Godunov's Method*, J. Comp. Phys., Volume 32, pp 101-136, 1979.

[48] E.E. Whiting, C. Park, Y. Liu, J.O. Arnold, J.A. Paterson, *NEQAIR96, Nonequilibrium and Equilibrium Radiative Transport and Spectra Program : User's Manual*, NASA, reference publication 1389 edition, December 1996.